Receptivity of Boundary Layers under Pressure Gradient

by

Lars-Uve Schrader

November 2008
Technical Reports
Royal Institute of Technology
Department of Mechanics
SE-100 44 Stockholm, Sweden

Akademisk avhandling som med tillstånd av Kungliga Tekniska Högskolan i Stockholm framlägges till offentlig granskning för avläggande av teknologie licentiatsexamen fredagen den 14 november 2008 kl 10.30 i K1, Kungliga Tekniska Högskolan, Teknikringen 56, entréplan, Stockholm.

Universitetsservice US–AB, Stockholm 2008

Receptivity of Boundary Layers under Pressure Gradient

Lars-Uve Schrader
Linné Flow Centre, Department of Mechanics, Royal Institute of Technology (KTH)
SE-100 44 Stockholm, Sweden

Abstract

Boundary-layer flow over bodies such as aircraft wings or turbine blades is characterized by a pressure gradient due to the curved surface of the body. The boundary layer may experience modal and non-modal instability, and the type of dominant instability depends on whether the body is swept with respect to the oncoming flow or not. The growth of these disturbances causes transition of the boundary-layer flow to turbulence. Provided that they are convective in nature, the instabilities will only arise and persist if the boundary layer is continuously exposed to a perturbation environment. This may for example consist of turbulent fluctuations or sound waves in the free stream or of non-uniformities on the surface of the body. In engineering, it is of relevance to understand how susceptive to such perturbations the boundary layer is, and this issue is subject of *receptivity analysis*.

In this thesis, receptivity of simplified prototypes for flow past a wing is studied. In particular, the three-dimensional swept-plate boundary layer and the boundary layer forming on a flat plate with elliptic leading edge are considered. The response of the boundary layer to vortical free-stream disturbances and surface roughness is analyzed, receptivity mechanisms are identified and their efficiency is quantified.

Descriptors: Swept-plate boundary layer, surface roughness, free-stream turbulence, cross-flow instability, streaks, leading-edge effects

Preface

This thesis deals with the receptivity and the early stages of instability in spatially evolving boundary-layer flows. A brief overview over the basic concepts and methods is presented in the first part. The second part is a collection of the following articles:

Paper 1. L.-U. Schrader, L. Brandt & D.S. Henningson, 2008
Receptivity mechanisms in three-dimensional boundary-layer flows. Journal of Fluid Mechanics, Article in Press

Paper 2. L.-U. Schrader, S. Amin & L. Brandt, 2008
Transition to turbulence in the boundary layer over a smooth and rough swept plate exposed to free-stream turbulence. To be submitted

Paper 3. L.-U. Schrader, L. Brandt, C. Mavriplis & D. S. Henningson, 2008
Receptivity to free-stream vorticity of flow past a flat plate with elliptic leading edge. Internal report

Division of work between authors
The research project was initiated by Dr. Luca Brandt (LB) who has acted as co-advisor. Prof. Dan Henningson (DH) has been the main supervisor until September 2008. Recently, LB achieved the qualification of a Ph.D. supervisor and has therefore become the main supervisor in September 2008.

Paper 1
The code development and computations were performed by Lars-Uve Schrader (LS) with feed-back from LB. Most of the paper has been written by LS with input from LB and DH.

Paper 2
The implementation of the surface roughness and the modifications of the free-stream turbulence for 3D flow was done by LS. The simulations were performed by Subir Amin (SA) as part of his Master's Thesis and by LS. Most parts of the paper have been written by LS with input from LB, and the part about the breakdown by LB together with LS. Feed-back has been provided by DH.

Paper 3
The simulation code has been made available by Dr. Paul Fischer. The generation of the computational mesh was developed by LS with input by Prof. Catherine Mavriplis (CM). The treatment of the boundary conditions was implemented by LS with feed-back from Prof. Ardeshir Hanifi. The computations were performed by LS. The paper was written by LS with input from LB, CM and DH.

Part I

Introduction

CHAPTER 1

Introduction

Cycling through the landscape with the wind gently blowing around the head is often considered as a pleasant leisure activity, but it is also an example for the relevance of fluid dynamics in everyday life. The aerodynamic forces on the cyclist and his bike dominate in fact over the rolling-friction forces above a speed of about 13 km/h, see Lukes *et al.* (2005), and account for circa 90% of the total resistance at a racing speed of 32 km/h. Beyond 10 km/h the laminar flow around the biker becomes unstable, causing a substantial raise in air resistance. The instabilities occur inside the thin boundary layer forming on rider and bicycle and are excited by perturbations arising for instance from the rough material of the biker's jacket or some fluctuations in the oncoming air stream. The initial magnitude of the triggered instabilities follows from the *receptivity* of the thin boundary layer to these perturbations, and the subsequent growth from the *stability* characteristics of the layer. Once the primary instabilities have reached a certain amplitude the boundary layer becomes susceptive to secondary instability which is usually generated by high-frequency fluctuations from outside and initiates the *break-down* of the laminar layer to its turbulent state.

Receptivity, disturbance growth and break-down define the three basic stages of transition of boundary-layer flow to turbulence. Though the receptivity process comes first on the route toward turbulence, researchers have initially focused on the stability of boundary layers. This seems indeed natural, as the stability is an intrinsic characteristic of the boundary layer, while receptivity involves the interaction of the layer with its environment. In stability theory the boundary-layer flow is treated as a dynamical system subject to certain initial and boundary conditions, and its stability characteristics are governed by the stability equations. In the classic linear analysis these are derived from the Navier-Stokes equations by considering small perturbations and linearizing the equations about the basic flow, assuming locally parallel flow. The solutions to the linear disturbance equations are wave-like disturbances with amplitudes being functions of one spatial direction solely. Such disturbance waves have indeed been observed in the experiments of Schubauer & Skramstad (1947) in the two-dimensional incompressible flat-plate boundary layer, where they are called Tollmien-Schlichting modes. On the other hand, the classic linear stability theory has failed in predicting the instability characteristics of Poiseuille pipe flow, for example. This led to the development of the theory of transient

disturbance growth, see for instance Reddy & Henningson (1993), accounting for the short-time behavior of the disturbance waves. The concepts of stability analysis are revisited in section 2.1.

Receptivity theory links the boundary-layer instabilities to the perturbations from the free stream or the wall. While the objective of a stability analysis is to clarify *whether* disturbances can arise inside the boundary layer at given conditions and at which rate they grow, a receptivity study is concerned with *how* and at which incipient amplitudes these disturbances are excited by the external perturbations. The receptivity problem had been formulated already by Morkovin (1969); however, the fundamental work of Goldstein (1983, 1985) and Ruban (1985) on the mechanisms behind receptivity was first published about fifteen years later. These early studies employed asymptotic analysis and have later been complemented by the Finite Reynolds-Number Theory (FRNT), e.g. in Crouch (1992, 1993); Choudhari & Streett (1992); Choudhari (1994), building again on the solution of the stability equations. The external perturbations are incorporated in FRNT either through the boundary conditions or through a forcing term, leading to inhomogeneous governing equations. Receptivity is briefly reviewed in section 2.2.

It is worth noticing that receptivity has so far not entered in the transition-prediction tools usually used in engineering and aeronautics. The most common approach, the e^N-method, builds on the classic linear theory, that is, neither receptivity nor nonlinear and secondary-instability growth nor transient amplification are considered. This clearly points to the need of ongoing research on receptivity and stability to improve the industrial prediction tools. Also the cyclist might benefit from the insights on this research field: He is well advised to wear tightly fitting clothes of either very smooth material to prevent laminar-turbulent transition or very rough material to avoid a long transitional region in the boundary layer and to promote rapid break-down to turbulence.

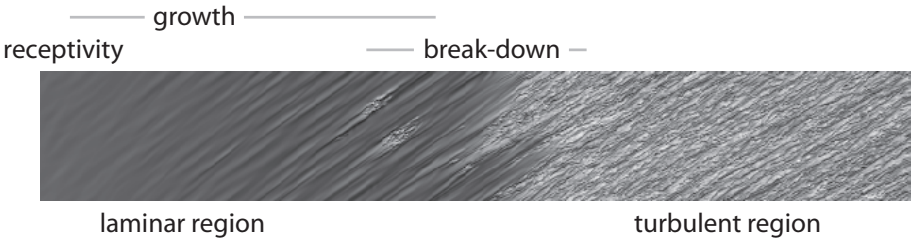

FIGURE 1.1. Receptivity, disturbance growth and break-down are the three basic stages of laminar-turbulent transition. Transition in the swept-plate boundary layer is shown here. The flow is from left to right. Details can be found in Part II, Paper 2.

CHAPTER 2

Theoretical background

2.1. Stability theory

Unsteady incompressible flow is governed by the time-dependent incompressible Navier-Stokes equations along with the continuity condition,

$$\frac{\partial \vec{\mathcal{U}}}{\partial t} + (\vec{\mathcal{U}} \cdot \nabla)\vec{\mathcal{U}} = -\nabla \mathcal{P} + \frac{1}{Re}\nabla^2 \vec{\mathcal{U}} \ , \tag{2.1a}$$

$$\nabla \cdot \vec{\mathcal{U}} = 0 \ . \tag{2.1b}$$

The instantaneous flow field is described by the velocity vector $\vec{\mathcal{U}}(\vec{x},t) = (\mathcal{U},\mathcal{V},\mathcal{W})^T$, solution to the equations (2.1), and the pressure field $\mathcal{P}(\vec{x},t)$, both depending on space $\vec{x} = (x,y,z)^T$ and time t. The equations above are in non-dimensional form with velocities normalized by the reference velocity U_{ref} and lengths by the reference length L_{ref}. The characteristic scales define along with the kinematic viscosity ν the Reynolds number,

$$Re = \frac{U_{ref} L_{ref}}{\nu} \ . \tag{2.2}$$

The solution $\vec{\mathcal{U}}(\vec{x},t)$ depends on the initial state of the flow field at time t_0,

$$\vec{\mathcal{U}}(\vec{x},t_0) = \vec{\mathcal{U}}_0 \ , \tag{2.3}$$

and on the conditions at the boundaries of the domain of interest. An example are the no-slip/impermeability conditions for the velocity at a solid non-porous wall.

The objective of stability theory is to determine the evolution of small disturbances $\vec{u}$ to the underlying base flow $\vec{U}$, being a steady or time-periodic solution of (2.1). If these disturbances grow in amplitude as time passes by (temporal perspective) or as they are transported downstream by the basic flow (spatial perspective), the boundary layer is unstable; if they, in contrast, die out, the flow is stable. The disturbances are governed by the stability equations, derived by substituting the decomposition

$$\vec{\mathcal{U}} = \vec{U} + \varepsilon \vec{u} \tag{2.4a}$$

$$\mathcal{P} = P + \varepsilon p \tag{2.4b}$$

into the equations (2.1). P is the mean pressure and p the pressure perturbation. In *linear* stability analysis the disturbance amplitude ε in (2.4) is assumed

to be small in comparison with U_{ref} and the linearized stability equations are solved, being readily to hand after discarding the terms of order ε^2,

$$\frac{\partial \vec{u}}{\partial t} + (\vec{U}\cdot\nabla)\vec{u} + (\vec{u}\cdot\nabla)\vec{U} = -\nabla p + \frac{1}{Re}\nabla^2\vec{u} \ , \tag{2.5a}$$

$$\nabla\cdot\vec{u} = 0 \ . \tag{2.5b}$$

The solution for $\vec{u}$ requires again the specification of an initial state, e.g. a disturbance-free incipient flow field, and boundary conditions, for instance zero slip at a solid wall.

2.1.1. *Classic eigenmode analysis*

If space and time can be separated, a temporal eigenmode ansatz assuming time-periodic instabilities may be substituted into decomposition (2.4),

$$\vec{\mathcal{Q}}(x,y,z,t) = \vec{Q}(x,y,z) + \varepsilon\vec{q}(x,y,z)e^{-i\omega t} \ , \tag{2.6}$$

where the velocity components and the pressure have been combined in the vectors $\vec{\mathcal{Q}}$, $\vec{Q}$ and $\vec{q}$ for the instantaneous flow field and its mean and fluctuating part, respectively. In classic linear theory, the ansatz (2.6) is simplified by assuming a one-dimensional, "locally parallel" basic flow and a "normal-mode"-like disturbance with an amplitude function depending on one spatial direction alone,

$$\vec{\mathcal{Q}}(x,y,z,t) = \vec{Q}(y) + \varepsilon\vec{q}(y)e^{i(\alpha x+\beta z-\omega t)} + \text{compl. conjg.} \ , \tag{2.7}$$

This approach has in particular been successful in viscous theory based on the Orr-Sommerfeld/Squire equations (Orr (1907); Sommerfeld (1908); Squire (1933)) and is valid not only in strictly parallel flow, e.g. developed laminar channel flow, but also for slowly varying inhomogeneous base flows. In two-dimensional boundary-layer flow at large enough Reynolds numbers, for instance, the predicted normal eigenmodes – the Tollmien-Schlichting waves – are an accurate approximation of the disturbance waves first observed in the experiment by Schubauer & Skramstad (1947). The derivation of the Orr-Sommerfeld/Squire system from the equations (2.5) together with the parallel-flow assumption is outlined in textbooks like Schmid & Henningson (2001); Drazin (2002), and the result is written for three-dimensional (e.g. Falkner-Skan-Cooke) flow and in wavenumber space here, indicated by the tilde,

$$\frac{\partial}{\partial t}\begin{pmatrix}\tilde{v}\\ \tilde{\eta}\end{pmatrix} = \begin{pmatrix}(\mathcal{D}^2-\alpha^2-\beta^2)^{-1}\mathcal{L}_{OS} & 0\\ i\alpha W' - i\beta U' & \mathcal{L}_{Sq}\end{pmatrix}\begin{pmatrix}\tilde{v}\\ \tilde{\eta}\end{pmatrix} \tag{2.8}$$

with the linear operators

$$\mathcal{L}_{OS} = (-i\alpha U - i\beta W)(\mathcal{D}^2-\alpha^2-\beta^2) + i\alpha U'' + i\beta W'' + \frac{1}{Re}(\mathcal{D}^2-\alpha^2-\beta^2)^2,$$

$$\mathcal{L}_{Sq} = -i\alpha U - i\beta W + \frac{1}{Re}(\mathcal{D}^2-\alpha^2-\beta^2) \ .$$

$\tilde{\eta}$ is the vertical vorticity; α and β are the stream- and spanwise wavenumbers; $\mathcal{D}$ is the normal-derivative operator and the prime and double prime denote

the first respective second derivative of the one-dimensional base flow. The solution of the initial-value problem (2.8) is,

$$\tilde{q} = e^{\mathcal{L}t}\tilde{q}|_{t=t_0} \quad , \tag{2.9}$$

where $\tilde{q} = (\tilde{v}, \tilde{\eta})^T$ for the Orr-Sommerfeld/Squire problem and the matrix operator in (2.8) is labelled $\mathcal{L}$. The key to stability analysis are the eigenvalues σ_i and -functions $\vec{\phi_i}$ of the matrix exponential,

$$e^{\mathcal{L}t}\vec{\phi_i} = \sigma_i\vec{\phi_i}, \qquad |\sigma_1| > \cdots > |\sigma_n|. \tag{2.10}$$

The instability condition stated above in words can now be mathematically formulated:

$$\text{Asymptotically unstable flow, if} \quad |\sigma_1| > 1 \quad , \tag{2.11a}$$

$$\text{Asymptotically stable flow otherwise.} \tag{2.11b}$$

The eigenvalues of $e^{\mathcal{L}t}$ and those of the matrix operator $\mathcal{L}$, denoted λ_i here, are related via $\lambda_i = \frac{1}{t}\log\sigma_i$ with λ_i being a measure for the amplification rate of the eigenmode $\vec{\phi_i}$.

Clearly from equation (2.11), only one eigenvalue governs the instability characteristics of the basic flow, namely that pertaining to the least stable eigenmode. The amplitude function of this mode is non-zero inside the boundary layer and tends to zero outside of it; hence, it is sometimes termed *boundary-layer mode*. Grosch & Salwen (1978) have shown that besides the boundary-layer modes there exists also a continuous eigenvalue spectrum in boundary-layer flows with all eigenmodes being damped. The amplitude functions of the continuous-spectrum modes differ significantly from those of the boundary-layer modes in that they are oscillatory in the free stream and tend to zero toward the wall. Therefore, they are sometimes labelled *free-stream modes*. Due to their shape these modes are adequate as a model for vortical free-stream perturbations in full Navier-Stokes simulations. This idea has been exploited by Jacobs & Durbin (1998) for Blasius flow, where a simplified method for the computation of the free-stream modes is presented. The free-stream modes have later been used in Jacobs & Durbin (2001); Brandt *et al.* (2004) as a model for free-stream turbulence in two-dimensional boundary-layer flow. The concept of the continuous-spectrum modes is extended to Falkner-Skan-Cooke flow in Part II of this thesis (Paper 1), where the free-stream modes are used in Direct Numerical Simulations (DNS) to develop a model for receptivity of swept-plate flow to free-stream vorticity. In Paper 2 the Falkner-Skan-Cooke free-stream modes are employed for the generation of synthetic free-stream turbulence at the inflow of the computational domain.

The discussion on the classic stability analysis is finalized by stating that the accuracy of predictions from linear theory along with (2.7) drops whenever "non-parallel effects" become important. A successful effort to reconcile the classic theory with stability problems in flows with more than one inhomogeneous direction has been the development of the Parabolized Stability Equation approach (PSE) by Herbert (see Herbert (1997) for a review). In PSE the basic

flow is still resolved in one direction only, but it is allowed to develop moderately in the other two directions. The PSE approach leads to parabolic stability equations amenable to an efficient spatial marching technique and is thus appropriate for parametric stability studies. Excellent agreement between results from PSE and DNS on the evolution of cross-flow instability in Falkner-Skan-Cooke flow was for instance demonstrated in Högberg & Henningson (1998). Another attempt to broaden the classic stability analysis is the global-stability theory where the eigenmode ansatz for spanwise periodic problems reads,

$$\vec{\mathcal{Q}}(x,y,z,t) = \vec{Q}(x,y) + \varepsilon\vec{q}(x,y)e^{i(\beta z-\omega t)} + \text{compl. conjg.} \ , \tag{2.12}$$

i.e. the eigenmodes have two-dimensional amplitude-shape functions and are periodic in only one spatial direction and in time. Global-mode theory is discussed in Theofilis *et al.* (2002); Åkervik & Henningson (2008).

2.1.2. *Transient growth*

The experiment by Schubauer & Skramstad (1947) appears convincing that the instability characteristics of the Blasius boundary layer were predictable by addressing the classic linear stability theory alone; however, already the work by Taylor (1939) had cast a shadow on the classic approach. Continuing research efforts revealed in fact that eigenmode analysis fails in predicting the response of the Blasius boundary layer to free-stream turbulence, for instance. Klebanoff (1971) observed boundary-layer disturbances differing seriously from the TS-waves predicted by linear eigenmode analysis in that they occurred further upstream, had a different shape and exhibited algebraic instead of exponential amplification. These disturbances were later called "Klebanoff modes" though they are not modal in nature. Ellingsen & Palm (1975) demonstrated for inviscid shear layers that there can indeed exist initial disturbances growing linearly in time instead of exponentially, producing a streaky pattern of alternating high and low streamwise velocity. This kind of amplification was termed 'transient growth' in Hultgren & Gustavsson (1981) and shown to exist in viscous flow, as well. Landahl (1980) proposed a physical explanation, building on the wall-normal displacement of fluid particles in shear flows by weak pairs of counter-rotating stream-wise vortices, causing stream-wise velocity perturbations. This so-called lift-up mechanism is efficient in forcing axial streaks of high and low stream-wise velocity alternating in the span-wise direction. The mathematical framework for transient growth is given in Butler & Farrell (1992); Reddy & Henningson (1993); Trefethen *et al.* (1993) and in the textbook by Schmid & Henningson (2001). It is based on the non-normality of the linear Navier-Stokes – or in the example above – Orr-Sommerfeld/Squire operator in shear flows, $\mathcal{L}\mathcal{L}^* \neq \mathcal{L}^*\mathcal{L}$, where the star denotes the adjoint operator. Transient growth of an initial disturbance at time $t = t_0$ is then given by,

$$G(t) = \|e^{\mathcal{L}t}\tilde{q}|_{t=t_0}\|^2 \ . \tag{2.13}$$

The condition for non-modal instability can be formulated by means of the singular values σ_i

$$e^{\mathcal{L}^* t} e^{\mathcal{L} t} \vec{\phi}_i = \sigma_i \vec{\phi}_i, \qquad \sigma_1 \geq \cdots \geq \sigma_n \geq 0. \tag{2.14}$$

and reads

$$\text{Transient growth, if} \quad \sigma_1 > 1 \ , \tag{2.15a}$$

$$\text{No transient growth otherwise.} \tag{2.15b}$$

Transient amplification describes hence the short-time behavior of boundary-layer disturbances, while linear growth is approached when $t \to \infty$, reflected by the attribute "asymptotic" in (2.11). Transient growth is also called *non-modal*, as the underlying mechanism does not rely on the evolution of a single growing eigenmode but on the interaction between eigenmodes of Orr-Sommerfeld and Squire type. This results in a boundary-layer disturbance changing its shape as individual modes grow or decay in time and space at different rates. Transient growth may for this reason occur before the subsequent exponential behavior and trigger laminar-turbulent transition before the asymptotic instability reaches relevant amplitude levels. The "natural transition" mechanism due to the latter disturbance is then "bypassed", and the transition route is called *bypass transition*. Paper 3 deals with the receptivity and the early transient-growth phase preceding bypass transition in the two-dimensional boundary layer on a plate with elliptic leading edge, where the "Klebanoff modes" play a central role, as well. In Paper 2, a scenario is considered where both non-modal and modal instabilities co-exist. The three-dimensional swept-plate boundary layer under free-stream turbulence is considered there, and it is found that asymptotic instability due to cross-flow modes outweighs transient instability in form of the streaks.

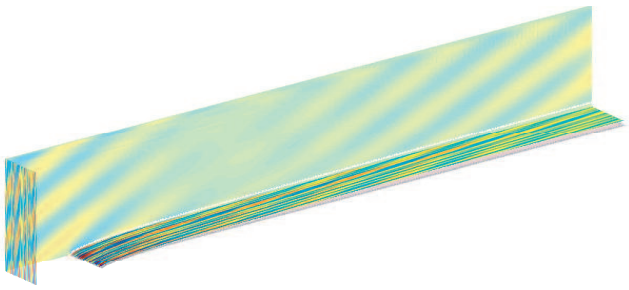

FIGURE 2.1. Response of the boundary layer on a flat plate with elliptic leading edge to vortical free-stream disturbances. The reader is referred to Part II, Paper 3.

2.2. Receptivity

In the previous section the focus has been on the instability of boundary-layer flow to modal and non-modal disturbances. It was also indicated that boundary-layer instability needs a forcing from outside[1] – for instance through the free-stream turbulence in Klebanoff's experiment – and that the nature and the initial amplitudes of the disturbances inside the layer strongly depend on the perturbation environment. Receptivity analysis extends the stability theory by including the connection between the forcing through external perturbations and the response of the boundary layer.

Perturbations residing in the free-stream or on the wall will always enforce a disturbance inside the boundary layer. If the forced disturbance field is able to feed the eigenmodes of the boundary layer with energy and a modal or non-modal instability arises, the layer is said to be *receptive* to the perturbation environment; if, in contrast, the forced response dies out, the boundary layer is not receptive. Receptivity requires a resonance in frequency and wavenumber between the enforced disturbance and the eigenmodes of the layer. In laboratory experiments perturbation sources may be designed such that this resonance is available, but many natural disturbance sources do not provide wavenumber resonance. This is the case in particular for free-stream disturbances, the length scales of which are governed by the inviscid dynamics in the outer flow, while the characteristic length of the TS-waves, for instance, are dominated by the viscous effects in the boundary layer. Examples are sound waves at low Mach numbers, possessing much larger wavelengths than the TS-modes, and the vortical free-stream disturbances considered in Paper 1 in this thesis with smaller chordwise wavelengths than the unstable cross-flow modes in the swept-plate boundary layer investigated there.

Despite the lack of direct wavenumber resonance, two-dimensional boundary-layer flow has been found to be receptive to free-stream sound under certain conditions, and likewise, the three-dimensional swept-plate boundary layer is demonstrated to be receptive to free-stream vortices in Paper 1. Goldstein (1983, 1985) was the first to propose an explanation for this apparent contradiction by introducing the concept of *length-scale conversion*. He considered two-dimensional flat-plate boundary-layer flow exposed to a plane acoustic free-stream disturbance. In the incompressible limit, the sound wave enforces a Stokes wave with the frequency of the acoustic forcing and with zero streamwise wavenumber. There is thus no direct wavenumber resonance between the Stokes and the TS-mode unless a second steady source provides the TS-wavenumber. This can be a non-uniformity at the wall, e.g. a roughness bump or a suction hole in the plate; but also the rapidly developing regions of the mean flow can convert the length scale of the enforced Stokes solution into that of the TS-wave. Such regions are found near the leading edge of the plate, where the boundary layer grows rapidly, or on a curved surface. Goldstein (1983,

[1]The focus is on convective instability here. In absolutely unstable flows the instability is sustained without external forcing, see e.g. Schmid & Henningson (2001).

1985) addressed asymptotic analysis to demonstrate receptivity through scale conversion. Expansion of the disturbance in powers of $\frac{1}{Re}$ leads to the triple-deck equations which are linearized in terms of the disturbance amplitude and govern the disturbance evolution in the limit of high Reynolds numbers. The triple-deck formulation is only valid at the first neutral point (branch I) of the unstable mode. A successful attempt to extend receptivity analysis to moderate Reynolds numbers and to the regions away from branch I of the instability was the Finite-Reynolds Number Theory (FRNT) first addressed by Zavol'skii *et al.* (1983). FRNT builds on the same ideas as the classic linear stability theory, namely (1) on the assumption of a one-dimensional "locally parallel" basic flow and (2) on small amplitudes of the external perturbations, allowing for linearization. FRNT has been applied in two-dimensional flat-plate flow by Crouch (1992) and Choudhari & Streett (1992) and in the Falkner-Skan-Cooke boundary layer by Crouch (1993) and Crouch (1994).

The Finite-Reynolds Number Theory is briefly discussed here by considering an acoustic free-stream disturbance with amplitude ε_u and a steady roughness bump with height ε_s in two-dimensional flow. In analogy with equation (2.4a) the instantaneous flow field can be decomposed,

$$\vec{\mathcal{U}}(x,y,t) = \vec{U}(y) + \varepsilon_u \vec{u}_u(x,y,t) + \varepsilon_s \vec{u}_s(x,y) + \varepsilon_u \varepsilon_c \vec{u}_{us}(x,y,t) \quad . \tag{2.16}$$

The total disturbance environment inside the boundary layer consists thus of the Stokes solution $\vec{u}_u$ due to the free-stream sound, the steady disturbance field $\vec{u}_s$ enforced by the roughness and the travelling wave $\vec{u}_{us}$ with the acoustic frequency and the length scales of the roughness. Like in classic stability theory, ansatz functions in the form of "normal modes" for the amplitude profiles of $\vec{u}_u$ and $\vec{u}_s$ are used in the FRNT,

$$\vec{u}_u(y,t) = \tilde{\vec{u}}_u(y) e^{-i\omega t} \tag{2.17a}$$

$$\vec{u}_s(x,y) = \frac{1}{2\pi} \int_{-\infty}^{\infty} \tilde{\vec{u}}_s(y;\alpha) e^{i\alpha x} d\alpha \quad . \tag{2.17b}$$

In the formulation of (2.17b) the roughness is assumed to be localized in chordwise direction; thus, the spectrum of the bump contains a large number of chordwise wavenumbers α. An integration over all present wavenumbers is then necessary to obtain the total steady contribution, leading to the Fourier transform in (2.17b). Further, the dependence of the spectral coefficient $\tilde{\vec{u}}_s$ on α must be specified, that is, a relation between the wavenumber spectrum $\tilde{H}(\alpha)$ of the bump contour and the disturbance velocity due to the bump needs to be established. In e.g. Crouch (1992) and in Paper 1 this is done by modelling the surface roughness through a projection of the no-slip conditions at the hump contour along the wall gradient of the mean flow onto the undisturbed wall, leading to non-homogeneous boundary conditions,

$$\tilde{\vec{u}}_s(0;\alpha) = -\tilde{H}(\alpha) \left(\frac{\partial \vec{U}}{\partial y} \right)_0 \quad . \tag{2.18}$$

At the free-stream boundary y_∞, a condition for the Stokes contribution $\tilde{\vec{u}}_u$ is prescribed,

$$\tilde{\vec{u}}_u(y_\infty) = \begin{pmatrix} e^{-i\omega t} \\ 0 \end{pmatrix} \ . \tag{2.19}$$

After plugging in decomposition (2.16) into the Navier-Stokes equations, linearizing about the mean flow, sorting the terms of order ε_u, ε_s and $\varepsilon_u\varepsilon_s$ and applying the ansatz (2.17) along with the boundary conditions (2.18) and (2.19) to the contributions of order ε_s and ε_u the steady disturbance field $\vec{u}_s$ due to the roughness and the unsteady Stokes solution $\vec{u}_u$ caused by the sound are obtained.

However, the receptivity analysis aims at determining the amplitude of the travelling wave $\vec{u}_{us}$ in equation (2.16), since the boundary-layer instability, here the TS-wave, is contained in this function. $\vec{u}_{us}$ is found by substituting the ansatz (2.17) into the contribution at order $\varepsilon_u\varepsilon_s$ to the total disturbance. The details of this derivation can be found in Crouch (1992); Choudhari (1994); Collis & Lele (1999) and the result reads,

$$\vec{u}_{us}(x,y,t) = \frac{1}{2\pi} \int_{-\infty}^{\infty} \tilde{\vec{u}}_{us}(y;\alpha) e^{i(\alpha x - \omega t)} d\alpha \ . \tag{2.20}$$

The form of the coefficient $\tilde{\vec{u}}_{us}$ is obtained when applying boundary conditions deduced from those in (2.18) and (2.19) to the contribution at order $\varepsilon_s\varepsilon_u$, see Crouch (1992),

$$\tilde{\vec{u}}_{us}(y;\alpha) = \varepsilon_s\varepsilon_u \tilde{H}(\alpha)\tilde{\Lambda}(\alpha)\overline{\vec{u}}_{us}(y) \ , \tag{2.21}$$

where $\overline{\vec{u}}_{us}(y)$ is a normalized amplitude function taking the form of a "normal mode". The α-dependence of $\tilde{\vec{u}}_{us}$ has been isolated in the function $\tilde{\Lambda}$ and the amplitude in the factor $\varepsilon_s\varepsilon_u$. The bump shape $\tilde{H}$ enters in (2.16) through the boundary conditions.

Clearly from (2.20), the travelling-wave field $\vec{u}_{us}$ contains the frequency of the free-stream sound and the wavenumbers provided by the roughness. Therefore, as time $t \to \infty$, $\vec{u}_{us}$ will be entirely dominated by the unstable TS-wave. This is reflected by the transfer function $\tilde{\Lambda}(\alpha)$ in equation (2.21) becoming very large at the wavenumber α_{TS} of the TS-wave, while the contributions at $\alpha \neq \alpha_{TS}$ die out. Tam (1981) shows that the integral in equation (2.20) then reduces to $2\pi i\tilde{C}(\alpha_{TS})$, where $\tilde{C}(\alpha_{TS})$ is defined as

$$\tilde{C}(\alpha_{TS}) = \lim_{\alpha \to \alpha_{TS}} [(\alpha - \alpha_{TS})\tilde{\Lambda}(\alpha)] \ . \tag{2.22}$$

Since the amplitude function $\overline{\vec{u}}_{us}$ in (2.21) is normalized to be 1 at its wall-normal maximum, the maximum amplitude of the TS-wave can be written as

$$A_{TS} = \varepsilon_u\varepsilon_s |\tilde{H}(\alpha_{TS})\tilde{C}(\alpha_{TS})| \ . \tag{2.23}$$

Equation (2.23) can be re-organized,

$$C_{rec} = \frac{A_{TS}}{\varepsilon_u\varepsilon_s |\tilde{H}(\alpha_{TS})|} \ , \tag{2.24}$$

where C_{rec} is the modulus of $\tilde{C}(\alpha_{TS})$. It should be noticed that equation (2.26) relates the amplitude A_{TS} of the boundary-layer instability to the amplitudes ε_u of the sound wave and $\varepsilon_s|\tilde{H}(\alpha_{TS})|$ of the roughness in the form

$$C_{rec} = \frac{\text{Initial instability amplitude}}{\text{Amplitudes of the perturbation sources}} \quad , \tag{2.25}$$

that is, C_{rec} is a measure for the efficiency in energy transfer from the driving perturbation sources to the TS-wave. C_{rec} is called *receptivity coefficient*, and it is in fact the key in receptivity analysis. Another interesting detail worth of notice is that only the spectral content of the bump function at the instability wavenumber, $|\tilde{H}(\alpha_{TS})|$, enters in C_{rec}, that is, the boundary layer is equally receptive to two roughness bumps of different shape as long as they provide the same amplitude at α_{TS}.

As indicated above, Finite-Reynolds Number Theory builds on the assumption of "parallel flow". Bertolotti (2000) presents an extension to include non-parallel effects at first order and shows that the shape-independence of receptivity to roughness is not always maintained. In Paper 1, C_{rec} has been determined through Direct Numerical Simulation (DNS) to characterize the receptivity of the three-dimensional swept-plate boundary layer to surface roughness and vortical free-stream modes. This type of base flow supports cross-flow instability which is three-dimensional, i.e. the spanwise wavenumber β has to be considered, as well. Steady localized roughness with sinusoidal shape in spanwise direction is shown to be efficient in exciting stationary cross-flow vortices ("CF") inside the boundary layer, and the receptivity coefficient is in this case

$$C_{rec} = \frac{A_{CF}}{\varepsilon_s|\tilde{H}_\beta(\alpha_{CF})|} \quad . \tag{2.26}$$

Figure 2.2 displays the dependence of C_{rec} on the spanwise wavenumber of the roughness. Three bumps with different contours are considered, as indicated by the three thick curves in (b). The figure shows that the shape-independence of receptivity to roughness is observed for most of the investigated spanwise wavenumbers. Further, the result obtained in parallel flow is plotted as a thin line. This curve corresponds to the prediction for C_{rec} by the FRNT and exhibits a moderate deviance to higher values. The exclusion of non-parallel effects leads thus to an over-prediction of roughness receptivity, i.e. the predictions from FRNT are "on the safe side".

The discussion on receptivity is concluded by highlighting the usefulness of the curves for C_{rec} like those in figure 2.2: Once the dependence of C_{rec} on the spanwise wavenumber is known for a given Reynolds number, the curves can be used to weight different instability components in a complex disturbance environment. This is demonstrated in figure 2.3 and at length in Paper 2, where the receptivity coefficients determined through simplified models for receptivity to roughness and free-stream vorticity are applied to predict the total boundary-layer disturbance in the flow over a swept plate. The figure shows that the

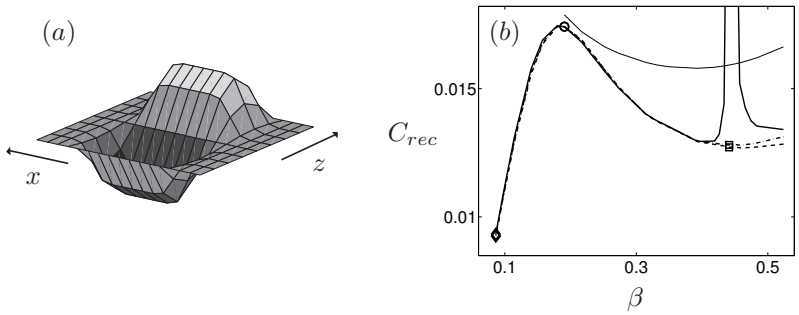

FIGURE 2.2. (a) Roughness bump with chordwise localized, spanwise sinusoidal shape. (b) Receptivity to three different roughness elements. Thick lines: Receptivity coefficient C_{rec} in spatially evolving flow versus spanwise wavenumber of the three roughness elements. Thin solid line: Receptivity coefficient in parallel flow. A detailed explanation of the figure is found in Paper 1.

prediction is already quite successful if only a small number of individual modes is considered.

The receptivity coefficients obtained from simplified linear models as those in Paper 1 or from calculations based on FRNT can also be combined with established transition-prediction tools such as the e^N-method to provide a refined prediction tool for industrial use, including the receptivity process. Since the instability amplitudes in the e^N-method are normalized with their magnitude at the first neutral point of the instability, it is more adequate to apply receptivity coefficients defined at branch I instead of those computed at the receptivity site. These coefficients are occasionally called *effective receptivity coefficients*, denoted C_{rec}^{eff} here. C_{rec}^{eff} can be used to determine the disturbance amplitude $A(x)$ at any location in the linear regime downstream of the receptivity site, if the N-factor of the instability is known,

$$A(x) = \varepsilon_s |\tilde{H}_\beta(\alpha_{CF})| C_{rec}^{eff} e^{N(x)}. \tag{2.27}$$

Since the receptivity mechanisms depend on many influencing factors, for instance the geometry of the problem of interest, the perturbation environment and the nature of the dominant instabilities, the practical application of the findings from receptivity analysis in an industrial context will require a vast database of receptivity coefficients. This motivates the continuation of research on this field to develop refined theoretical receptivity models. Direct Numerical and Large-Eddy Simulations like those presented in this thesis will in the future continue to serve as validation tools for these models.

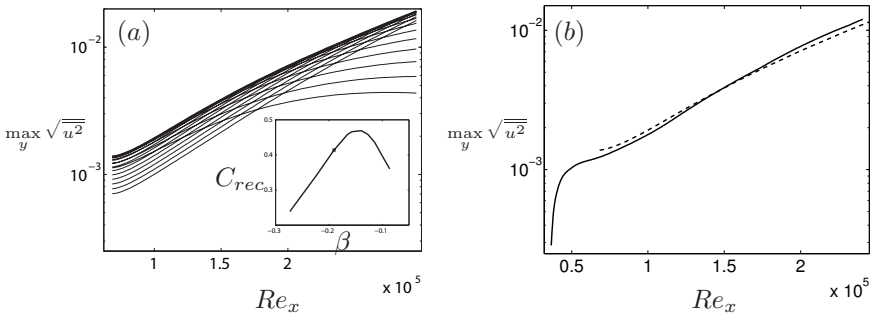

FIGURE 2.3. (a) Amplitude evolution of single unstable travelling cross-flow waves in swept-plate flow and the corresponding receptivity coefficients. The latter are used to weight the individual evolution curves to obtain the envelope. (b) Swept-plate boundary-layer response to free-stream turbulence in comparison with the envelope from (a). See Paper 2 for a discussion.

CHAPTER 3

Numerical methods

The results compiled in Paper 1 and 2 have been obtained by using the simulation code **Simson**, building on a global spectral method and described in Chevalier *et al.* (2007). For the computations of the flow over the flat plate with leading edge presented in Paper 3, the code **Nek5000** employing the Spectral-Element Method by Patera (1984) has been addressed, see Tufo & Fischer (1999). Both numerical approaches are discussed in the papers in Part II of this thesis, and the reader is referred to the respective sections. Here, the focus is on a comparison between the global spectral technique and the Spectral-Element Method, see table 3.1, to highlight their applicability and limitations.

In global spectral methods, the solution to the Navier-Stokes equations is approximated by a linear combination of sinusoidal or polynomial basis functions prescribed over the entire numerical domain, as indicated by the label *global*. In contrast, the polynomial basis functions used in the Spectral-Element Method are defined on sub-domains called spectral elements, and the method is thus a local approach. It has its local nature in common with the Finite-Element Method (FEM), while the orthogonality of the basis functions distinguishes it from FEM. The benefit of the local approach is its geometric flexibility and the availability of two refinement strategies: (1) through the reduction of the element size (h-refinement) and (2) by raising the order of the basis polynomials (p-refinement). Thus, the Spectral-Element Method allows for localized refinement, while in the global approach, an increase in resolution along one direction always affects the whole numerical domain. On the other hand, the global spectral method ensures exponential convergence as the mesh is refined, while the convergence rate of the Spectral-Element Method is usually lower. This together with the possibility of employing Fast-Fourier Transforms ensures the high efficiency of the global spectral approach.

In summary, the global spectral method is due to its performance the preferred tool when the geometry of the simulation domain can be kept simple and when sufficiently smooth solutions to the governing equations are expected. For complex geometries or flow fields with local steep gradients, requiring localized refinement, the Spectral-Element Method is an accurate alternative to finite-difference or -volume methods. The discussion of the two approaches is concluded with the remark that the Spectral-Element Method passes into a

global spectral method, when the physical domain of interest is decomposed into one single element.

TABLE 3.1. Global spectral method versus Spectral-Element Method.

	Global spectral method	Spectral-Element Method
Simulation code	**Simson**	**Nek5000**
Programming language	Mainly Fortran77	Mainly Fortran77
General characteristics	Global approach Fourier-Galerkin-Chebyshev tau method Fast Fourier transforms	Local approach Galerkin method
Special features	Fringe technique	
Numerical grid	Equidistant in the horizontal directions, Gauss-Lobatto-Chebyshev nodes in the vertical direction	Sub-domains (spectral elements) with arbitrary shape, Gauss-Lobatto-Legendre points
Basis functions/ spatial discretization	Fourier modes in the horizontal directions, Chebyshev polynomials in the vertical direction	Polynomial interpolation of Lagrange form at Legendre nodes
De-aliasing	$\frac{3}{2}$-rule in the horizontal directions	Filtering at the highest wavenumbers, over-integration
Time integration	Implicit/explicit splitting: Four-step third order Runge- Kutta method + second-order Crank-Nicholson	Implicit/explicit splitting technique: Third-order backward differentiation + third-order Adams-Bashforth
Parallelisation	MPI and OpenMP Partitioning into slices in span-wise direction	MPI Element-wise partitioning
Applications	Incompressible laminar and turbulent flow: Channel flow, 2D and 3D boundary-layer flow on flat plates	Massively parallel simulations of incompressible laminar and turbulent flow in complex geometries
Limitations	To problems which can be made periodic using the fringe technique Simple geometries, e.g. no curved walls or leading edge	Less efficient than the global spectral method

CHAPTER 4

Summary of the papers

Paper 1

Receptivity mechanisms in three-dimensional boundary-layer flows.
In this article receptivity mechanisms in swept-plate flow under favorable pressure gradient are analyzed. The sensitivity of the boundary layer to perturbations arising from the surface of the plate or from the free stream is termed *receptivity*. Two different disturbance sources are considered: a surface-roughness element being localized in the chord- and sinusoidal in the span-wise direction and a vortical free-stream disturbance modelled by a continuous-spectrum Orr-Sommerfeld mode. In the presence of these disturbances the boundary layer response is dominated by steady and unsteady cross-flow modes, respectively. The efficiency of energy transfer from the forced disturbance due to the roughness and the free-stream vorticity to the cross-flow instability is quantified in terms of the receptivity coefficient. A parameter study is performed to identify the length scales of the perturbation with most efficient receptivity.

The receptivity mechanism for unsteady cross-flow waves due to free-stream vorticity has been explained for the first time in the paper. The focus has been on demonstrating the link between penetration and decay of the free-stream disturbance and the receptivity of the boundary layer to it. It has been found that scale conversion is a key element and that receptivity to free-stream vorticity is most efficient in the rapidly evolving upstream region of the layer. Further, to determine whether steady or unsteady cross-flow modes are dominant prior to the breakdown of the boundary layer to turbulence, a combination of surface roughness and free-stream vorticity has been considered. It has been found that stationary cross-flow vortices dominate the boundary-layer response below an amplitude of the free-stream vortex of about 0.5%.

Paper 2

Transition to turbulence in the boundary layer over a smooth and rough swept plate exposed to free-stream turbulence.
This article is closely linked with Paper 1 in that the material on receptivity presented there is extended. Swept-plate boundary-layer flow with free-stream acceleration in chordwise direction is considered, being a prototype for swept-wing flow downstream of the leading edge and upstream of the pressure minimum of the wing. The flow is exposed to two different perturbations

sources: free-stream turbulence and localized wall roughness with random amplitude along the span. Thus, the disturbance sources are more complex than those studied in Paper 1, and the focus has been on demonstrating that the receptivity coefficients presented there are also applicable in a more realistic perturbation environment.

In addition to the receptivity study, a description of the break-down to turbulence of the swept-plate boundary layer is included in Paper 2. The numerical simulation of transition in three-dimensional boundary-layer flow is a novelty and has not been addressed before. Here, Large-Eddy Simulations are performed with the aim of identifying the relevant disturbance structures excited by free-stream turbulence and random wall roughness at different disturbance amplitudes.

Paper 3

Receptivity to free-stream vorticity of flow past a flat plate with elliptic leading edge.

Two-dimensional flow over a flat plate with leading edge of elliptic shape is investigated in Paper 3. The focus is on studying the boundary-layer response when leading-edge- and surface-curvature effects are included. The Spectral-Element Method is addressed, allowing for the simulation of flow around bodies with curved surface. A vortical disturbance is imposed at the inflow plane of the computational domain. In order to isolate the effect of the three vorticity components on the response of the boundary layer, free-stream perturbations with axial, vertical and span-wise vorticity are considered separately. It has been found that the disturbance inside the boundary layer is dominated by long streaks triggered through low-frequency axial free-stream vorticity. However, at low frequencies, also wall-normal free-stream vorticity contributes to some extent to the total disturbance amplitudes in the boundary layer, in particular if the leading edge is blunt. The vertical vortex tubes in the free stream are wrapped around the leading edge and tilted, and this mechanism triggers axial vorticity. For span-wise free-stream vorticity of high frequency, the formation of Tollmien-Schlichting waves is enhanced in the presence of a blunt leading edge. This leading-edge effect is, however, of minor importance, as the amplitudes of the TS-waves remain low in comparison of those of the low-frequency streaks.

CHAPTER 5

Outlook

In the present thesis receptivity of spatially evolving boundary layers to free-stream turbulence and wall roughness is investigated. Three-dimensional boundary-layer flow of Falkner-Skan-Cooke type and two-dimensional flow past a flat plate with elliptic leading edge have so far been considered. Both types of flow accommodate various characteristics of the flow over a swept wing: the chordwise pressure gradient, the streamline curvature and the cross flow in the case of the swept-plate configuration and the consideration of leading edge and wall curvature in the case of the flat plate with elliptic nose. A natural extension is then to combine these ingredients in order to refine the model for swept-wing flow.

At the Department of Mechanics, experiments on receptivity of the boundary layer on a swept flat plate with elliptic leading edge are currently carried out in the Minimum-Turbulence Level (MTL) wind tunnel within the European TELFONA project. Apart from the pressure distribution due to the leading-edge curvature, a favorable pressure gradient is imposed in the free stream by means of the bump-shaped roof of the test section. In this way a Falkner-Skan-Cooke like velocity distribution is obtained in the free stream above the flat plate. The boundary layer is perturbed by placing tiny cylindrical roughness elements near the leading edge and by inserting a turbulence grid upstream of the plate. In the continuation of the present research project, simulations of this configuration will be performed by means of the Spectral-Element Method, and the results on receptivity to roughness and free-stream turbulence will be compared with the experimental findings.

The Spectral-Element Method opens the possibility of accurately studying the flow around bodies of interest in aeronautics or turbo-machinery. One example is the flow field over a concave wall where other instability types than those considered in this thesis come into play. If the radius of curvature is of the order of the boundary-layer thickness, the centrifugal forces become large enough to create a wall-normal pressure variation. This leads to centrifugal instability and the formation of Görtler vortices. Simulations of this scenario will together with the present results provide insights which will in the future be useful for the computation of the transitional and turbulent flow field around a full-wing model. Such simulations will, however, require modelling techniques for the smallest disturbance structures in the flow field such as the sub-grid models applied in LES.

Acknowledgements

The present thesis is the summary of about two and a half years of research in Prof. Dan Henningson's group at KTH Mechanics. During this time I did not only learn a lot on fluid mechanics and numerical simulation of flows but I also enjoyed the kindly atmosphere in our team.

I would like to thank my supervisor Prof. Dan Henningson for guiding me through my studies and giving me the opportunity of attending exciting conferences and meetings. Many thanks to my co-advisor Dr. Luca Brandt – now my main advisor – for sharing his vast knowledge and experience with me, but also for continuously putting me and our group into good humour. Dr. Ardeshir Hanifi and Dr. Philipp Schlatter are also acknowledged for their help.

Shervin Bagheri and David Tempelmann, my office mates, play a major role in creating a friendly atmosphere at work day after day – many thanks to them. Onofrio Semeraro joined us a couple of days ago – welcome. It makes me glad at any time to meet Espen Åkervik (the creator of the most imaginative nicknames), Antonios Monokrousos, Johan Ohlsson, Qiang Li, Yohann Duguet and Stefan Ivanell.

I am grateful for the valuable comments of Dr. Jens Fransson, Qiang Li and Dr. Philipp Schlatter on this manuscript.

The Swedish Research Council (Vetenskapsrådet) is gratefully acknowledged for the funding of the project.

This short paragraph is traditionally rounded off with a phrase in native language:

Herzlichen Dank an Euch, meine Eltern, die Ihr den Grund für meinen Lebensweg gelegt habt!

Bibliography

Åkervik, E. & Henningson, D. S. 2008 The use of global modes to understand transition and perform flow control. *Phys. Fluids* **20** (031302).

Bertolotti, F. P. 2000 Receptivity of three-dimensional boundary-layers to localized wall roughness and suction. *Phys. Fluids* **12(7)**, 1799–1809.

Brandt, L., Schlatter, P. & Henningson, D. S. 2004 Transition in boundary layers subject to free-stream turbulence. *J. Fluid Mech.* **517**, 167–198.

Butler, K. M. & Farrell, B. F. 1992 Three-dimensional optimal perturbations in viscous shear flow. *Phys. Fluids A* **4**, 1637–1650.

Chevalier, M., Schlatter, P., Lundbladh, A. & Henningson, D. S. 2007 A Pseudo-Spectral Solver for Incompressible Boundary Layer Flows. *Tech. Rep* TRITA-MEK 2007:07. Royal Institute of Technology (KTH), Dept. of Mechanics, Stockholm.

Choudhari, M. 1994 Roughness-induced Generation of Crossflow Vortices in Three-Dimensional Boundary Layers. *Theoret. Comput. Fluid Dynamics 6* pp. 1–30.

Choudhari, M. & Streett, C. L. 1992 A finite Reynolds number approach for the prediction of boundary layer receptivity in localized regions. *Phys. Fluids A* **4**.

Collis, S. S. & Lele, S. K. 1999 Receptivity to surface roughness near a swept leading edge. *J. Fluid Mech.* **380**, 141–168.

Crouch, J. D. 1992 Localized receptivity of boundary layers. *Phys. Fluids A* **4 (7)**, 1408–1414.

Crouch, J. D. 1993 Receptivity of three-dimensional boundary layers. *AIAA Paper* (93-0074).

Crouch, J. D. 1994 Distributed excitation of Tollmien-Schlichting waves by vortical free-stream disturbances. *Phys. Fluids* **6(1)**, 217–223.

Drazin, P. G. 2002 *Introduction to Hydrodynamic Stability*. Cambridge University Press.

Ellingsen, T. & Palm, E. 1975 Stability of linear flow. *Phys. Fluids* **18**, 487–488.

Goldstein, M. E. 1983 The Evolution of Tollmien-Schlichting Waves Near a Leading Edge. *J. Fluid Mech.* **127**, 59–81.

Goldstein, M. E. 1985 Scattering of Acoustic Waves into Tollmien-Schlichting Waves by Small Streamwise Variations in Surface Geometry. *J. Fluid Mech.* **154**, 509–529.

Grosch, C. E. & Salwen, H. 1978 The continuous spectrum of the Orr-Sommerfeld equation. Part 1. The spectrum and the eigenfunctions. *J. Fluid Mech.* **87**, 33–54.

Herbert, T. 1997 Parabolized stability equations. *Annu. Rev. Fluid Mech.* **29**, 245–283.

Högberg, M. & Henningson, D. S. 1998 Secondary instability of cross-flow vortices in Falkner-Skan-Cooke boundary layers. *J. Fluid Mech.* **368**, 339–357.

Hultgren, L. S. & Gustavsson, L. H. 1981 Algebraic growth of disturbances in a laminar boundary layer. *Phys. Fluids* **24**, 1000–1004.

Jacobs, R. G. & Durbin, P. A. 1998 Shear sheltering and continuous spectrum of the Orr-Sommerfeld equation. *Phys. Fluids* **10(8)**, 2006–2011.

Jacobs, R. G. & Durbin, P. A. 2001 Simulations of bypass transition. *J. Fluid Mech.* **428**, 185–212.

Klebanoff, P. S. 1971 Effect of free-stream turbulence on the laminar boundary layer. *Bull. Am. Phys. Soc.* **10**, 1323.

Landahl, M. T. 1980 A note on an algebraic instability of inviscid parallel shear flows. *J. Fluid Mech.* **98, part 2**, 243–251.

Lukes, R. A., Chin, S. B. & Haake, S. J. 2005 The understanding and development of cycling aerodynamics. *Sports Engineering* **8**, 59–74.

Morkovin, M. V. 1969 Bypass-transition research: issues and philosophy. *Tech. Rep* AFFDL-TR-68-149. Air Force Flight Dynamics Laboratory, Wright-Paterson Air Force Base.

Orr, W. M. F. 1907 The stability or instability of the steady motions of a perfect liquid and of a viscous liquid. Part I: A perfect liquid. Part II: A viscous liquid. In *Proc. Roy. Irish Acad. A*, , vol. 27, pp. 9–138.

Patera, A. T. 1984 A Spectral Element Method for Fluid Dynamics: Laminar Flow in a Channel Expansion. *J. Comp. Phys.* **54**, 468–488.

Reddy, S. C. & Henningson, D. S. 1993 Energy growth in viscous channel flows. *J. Fluid Mech.* **252**, 209–238.

Ruban, A. I. 1985 On the Generation of Tollmien-Schlichting Waves by Sound. *Fluid Dynamics* **19**, 709–716.

Schmid, P. J. & Henningson, D. S. 2001 *Stability and Transition in Shear Flows*. Springer.

Schubauer, G. B. & Skramstad, H. K. 1947 Laminar boundary layer oscillations and stability of laminar flow. *J. Aero. Sci.* **14**, 69–78.

Sommerfeld, A. 1908 Ein Beitrag zur hydrodynamischen Erklärung der turbulenten Flüssigkeitsbewegungen. In *Proc. 4th Internat. Congr. Math.*, , vol. III, pp. 116–124. Rome.

Squire, H. B. 1933 On the stability of three-dimensional disturbances of viscous flow between parallel walls. In *Proc. Roy. Soc. Lond. A*, , vol. 142, pp. 621–628.

Tam, C. K. W. 1981 The excitation of Tollmien-Schlichting waves in low subsonic boundary layers by free-stream sound waves. *J. Fluid Mech.* **109**, 483–501.

Taylor, G. I. 1939 Some recent developments in the study of turbulence. In *Proc. 5th Intl. Congr. Appl. Mech.* (ed. J. P. D. Hartog & H. Peters), pp. 294–310. Wiley.

Theofilis, V., Barkley, D. & Sherwin, S. 2002 Spectral/hp element technology for global flow instability and control. *Aeronaut. J.* **106**, 619–625.

Trefethen, L. N., Trefethen, A. N., Reddy, S. C. & T. A, D. 1993 Hydrodynamic stability without eigenvalues. *Science* **261**, 578–584.

Tufo, H. M. & Fischer, P. F. 1999 Terascale spectral element algorithms and implementations. In *Supercomputing, ACM/IEEE 1999 Conference*.

Zavol'skii, N. A., Reutov, V. P. & Ryboushkina, G. V. 1983 Generation of Tollmien-Schlichting Waves via Scattering of Acoustic and Vortex Perturbations in Boundary Layer on Wavy Surface. *J. Appl. Mech. Tech. Phys.* pp. 79–86.

Part II

Papers

1

Paper 1

Receptivity mechanisms in three-dimensional boundary-layer flows

By Lars-Uve Schrader, Luca Brandt & Dan S. Henningson

Linné Flow Centre, Department of Mechanics
Royal Institute of Technology, SE-100 44 Stockholm, Sweden

Journal of Fluid Mechanics, Article in Press

Receptivity in three-dimensional boundary-layer flow to localized surface roughness and free-stream vorticity is studied. A boundary layer of Falkner-Skan-Cooke type with favorable pressure gradient is considered to model the flow slightly downstream of a swept-wing leading edge. In this region stationary and travelling cross-flow instability dominates over other instability types. Three scenarios are investigated: the presence of low-amplitude chordwise localized, spanwise periodic roughness elements on the plate, the impingement of a weak vortical free-stream mode on the boundary layer and the combination of both disturbance sources. Three receptivity mechanisms are identified: steady receptivity to roughness, unsteady receptivity to free-stream vorticity and unsteady receptivity to vortical modes scattered at the roughness. Both roughness and vortical modes provide efficient direct receptivity mechanisms for stationary and travelling cross-flow instabilities. We find that stationary cross-flow modes dominate for free-stream turbulence below a level of about 0.5%, whereas higher turbulence levels will promote the unsteady receptivity mechanism. Under the assumption of small amplitudes of the roughness and the free-stream disturbance, the unsteady receptivity process due to scattering of free-stream vorticity at the roughness has been found to give small initial disturbance amplitudes in comparison to the direct mechanism for free-stream modes. However, in many environments free-stream vorticity and roughness may excite interacting unstable stationary and travelling cross-flow waves. This nonlinear process may rapidly lead to large disturbance amplitudes and promote transition to turbulence.

1. Introduction

The classical transition path to turbulence in laminar boundary-layer flow is characterized initially by the receptivity phase, i.e. the conversion of external perturbations into boundary-layer disturbances, subsequently by linear and nonlinear growth of the disturbances and finally by the breakdown to turbulence via secondary instability. Despite the fact that the linear amplification of the unstable waves can now be accurately estimated, reliable values for the

initial condition of these perturbations need to be provided. Commonly used industrial transition-prediction tools, e.g. the e^N-method, exclude the receptivity phase. In order to overcome the need of "guessing" the initial disturbance conditions, receptivity has been studied analytically, experimentally and numerically in the past.

1.1. *Receptivity of Blasius flow*

The foundation of receptivity studies had already been laid in the eighties by Goldstein (1983, 1985) and Ruban (1985), who employed asymptotic analysis to investigate receptivity at the first neutral point of Tollmien-Schlichting (TS) instability in Blasius flow. They pointed out that resonance regarding frequency and wave vector between the external disturbances and the unstable eigenmode of the base flow is necessary to trigger boundary-layer instability. The excitation of TS waves, for instance, requires unsteady external perturbations, e.g. acoustic or vortical free-stream disturbances. However, free-stream perturbations feature in general larger chordwise wavelengths than the discrete eigenmodes of the mean flow. Hence, scale reduction is necessary to trigger TS instability by free-stream disturbances. Goldstein (1985) shows that scale conversion requires a short-scale downstream variation of the base flow. This requirement is fulfilled in two regions: shortly downstream of the leading edge where the boundary layer grows rapidly, and in the vicinity of a localized surface non-uniformity. Thus, two different receptivity mechanisms to unsteady free-stream perturbations are imaginable: (1) a direct process in the leading-edge region, associated with the unsteady free-stream disturbance, and (2) a mechanism associated with the interaction between unsteady free-stream perturbations and the steady disturbance induced by localized surface non-uniformity. For acoustic free-stream perturbations only the second receptivity mechanism proved to be efficient.

1.2. *Receptivity of three-dimensional boundary layers*

Three-dimensional boundary layers can be found on swept wings or blades and are therefore of importance in aeronautics and turbomachinery. In particular, the flow over a swept flat plate subject to a chordwise pressure gradient has often been considered in literature. This is a prototype for swept wings, being referred to as Falkner-Skan-Cooke boundary layer. Most studies focus on cross-flow instability waves, since they dominate the perturbation scenario inside the boundary layer, given a large sweep angle. In contrast to TS instability, cross-flow instability is of inviscid type and can be stationary as well as travelling.

Results on receptivity and stability in three-dimensional boundary-layer flow have been reviewed by Saric *et al.* (2003). In the nineties, the Finite Reynolds-Number Theory (FRNT), originally developed by Zavol'skii *et al.* (1983) for two-dimensional boundary layers, has been addressed by e.g. Crouch (1993), Choudhari (1994) and Ng & Crouch (1999). In contrast to asymptotic

analysis, FRNT is valid for moderate Reynolds numbers and can be applied upstream and downstream of the first neutral point of the instability. It is based on perturbation equations of Orr-Sommerfeld/Squire type and incorporates in its usual formulation the parallel-flow assumption. External disturbances are included in Finite Reynolds-Number Theory as non-homogeneous boundary conditions, e.g. for wall roughness, or as an additional forcing term, e.g. for acoustic free-stream waves. Finite Reynolds-Number Theory further assumes that the excited boundary-layer disturbances are convective in nature. The work by Crouch (1993) and Choudhari (1994) deals with Falkner-Skan-Cooke boundary-layer flow exposed to both surface non-uniformities and acoustic free-stream perturbations. These authors consider linear receptivity to localized small-amplitude roughness elements, exciting steady cross-flow instability, and an unsteady receptivity mechanism due to a weak planar acoustic free-stream wave scattered at the roughness, generating travelling cross-flow modes. They characterize the receptivity process by an efficiency coefficient, which relates the initial amplitude of the instability mode to that of the triggering perturbations. Although Crouch (1993) and Choudhari (1994) found higher efficiency for the unsteady receptivity mechanism, the steady receptivity process to roughness gave larger initial disturbance amplitudes. This is due to the interaction of two small-amplitude disturbances in the case of unsteady receptivity. They concluded therefore that stationary cross-flow vortices are more likely to dominate transition in swept-wing flow under flight conditions than travelling cross-flow instability.

Ng & Crouch (1999) and Collis & Lele (1999) consider receptivity to localized roughness of flow over a swept parabolic cylinder. While the former authors use this configuration as base flow for a FRNT study, Collis & Lele (1999) perform both non-parallel FRNT calculations and Direct Numerical Simulations based on linearized perturbation equations. Spatial evolution of the boundary layer and surface curvature are included in their work. They found that non-parallel effects attenuate steady receptivity, while convex curvature enhances it. As in Crouch (1993) and Choudhari (1994) the most efficient receptivity sites were found slightly upstream of the first neutral point of the triggered stationary instability. Also Bertolotti (2000) studied the effect of non-parallel mean flow on receptivity to localized roughness for swept-wing flow. He emphasizes that non-parallel effects are substantial especially in the leading-edge vicinity. This is, on the one hand, due to rapid boundary-layer growth, on the other hand to highly curved streamlines in this region. Bertolotti performs his analysis in Fourier space, expanding to first order the base flow and the disturbance in the streamwise coordinate about the roughness location. The receptivity amplitude is then expressed as the sum of a zeroth- and a first-order contribution, and two separate efficiency coefficients are introduced. While the zeroth-order part resembles the formulation for the receptivity amplitude in Finite Reynolds-Number Theory, the first-order contribution also involves the

derivative of the Fourier amplitude of the roughness with respect to the instability wavenumber. Bertolotti (2000) found that non-parallel effects attenuate roughness receptivity, as well.

1.3. *Receptivity to vortical free-stream disturbances*

The numerical studies mentioned above are limited to acoustic free-stream disturbances. In turbomachinery, for instance, vortical perturbations in the free stream are often more relevant. Experimental work has been done on receptivity and transition of three-dimensional boundary layers subject to vortical free-stream disturbances, for instance by Bippes & Deyhle (1992) and Reibert *et al.* (1996). Also these studies revealed that steady cross-flow disturbances dominate the boundary-layer response at the typically low turbulence levels under flight conditions. However, this may not be the case in noisy environments and for wind-tunnel tests, see Saric *et al.* (2003).

While receptivity of three-dimensional boundary-layer flow to free-stream vortices is not as well-examined, many publications on numerical and experimental studies of two-dimensional boundary layers subject to vortical free-stream disturbances are available; see for example Jacobs & Durbin (1998, 2001), Brandt *et al.* (2004), Bertolotti & Kendall (1997), Kendall (1998), Fransson *et al.* (2005) and the review by Saric *et al.* (2002). Buter & Reed (1994) consider two-dimensional flow past a flat plate with an elliptic leading edge, exposed to time-periodic spanwise free-stream vortices. They found a receptivity mechanism for TS instability, which is, however, weaker than acoustic receptivity studied earlier by Lin *et al.* (1992) for the same configuration. The receptivity process becomes completely different, when the free-stream perturbations contain also streamwise vorticity. Then, the key structures prior to transition are no longer TS waves but streamwise streaks of alternating high- and low-momentum fluid. The formation of the streaky pattern is due to the interaction between non-normal eigenmodes of the base flow. Bertolotti (1997) found for Blasius flow that maximum receptivity is obtained for free-stream vortices with zero streamwise wavenumber. He suggests a linear receptivity mechanism, by which the free-stream vortices diffuse into the boundary layer close to the leading edge and cause the formation of the streaks inside it. This process has been confirmed by Bertolotti & Kendall (1997) in an experiment with controlled free-stream conditions through the generation of a weak axial vortex by a micro wing upstream of a flat plate with elliptic leading edge. Although its core was located outside the boundary layer the streamwise vortex was able to produce a rather strong perturbation inside it. The work also includes results from a numerical model of this flow configuration, and good agreement between the measured and the numerically determined amplitude function of the boundary-layer perturbation has been found. Berlin & Henningson (1999) consider both streamwise modes and a pair of oblique waves in the free stream. Apart from the linear receptivity mechanism, being efficient only for streamwise free-stream vorticity, they also found a nonlinear

receptivity mechanism due to the interaction of two streamwise or two oblique free-stream vortices. Jacobs & Durbin (1998) suggest an alternative model for vortical free-stream disturbances in Blasius flow, based on the concept of the continuous spectrum of the Orr-Sommerfeld/Squire operator. They show that penetration of the vortical mode into the boundary layer is crucial for receptivity and that deepest penetration is obtained for low-frequency free-stream vorticity at low Reynolds numbers. The model of Jacobs & Durbin (1998) is used by Brandt *et al.* (2002) and compared with the oblique-mode model of Berlin & Henningson (1999). These authors found similar nonlinear receptivity mechanisms for both types of free-stream disturbances. To obtain a more realistic model for turbulence in the outer flow, Jacobs & Durbin (2001) and Brandt *et al.* (2004) consider the superposition of a large number of modes from the continuous Orr-Sommerfeld/Squire spectrum, weighted to obtain a typical energy-density spectrum of isotropic turbulence. For free-stream turbulence dominated by low frequencies mainly the linear receptivity mechanism was found to cause the streak generation, whereas receptivity to high-frequency free-stream turbulence is characterized by the nonlinear mechanism. Zaki & Durbin (2005) show that bypass transition can be observed in numerical simulations, if only two vortical free-stream modes are prescribed at the inflow: one of low and one of high frequency. While the low-frequency mode is responsible for the generation of streaks, the high-frequency mode triggers secondary instability upon the streaky flow.

The influence of streamwise pressure gradient on receptivity and transition in the presence of free-stream vorticity was investigated in Zaki & Durbin (2006) by Direct Numerical Simulation of two-dimensional boundary-layer flow subject to a Falkner-Skan pressure distribution. That work also includes a study of the interaction between the continuous-spectrum modes and the boundary layer in Falkner-Skan flow, as has already been presented before by Maslowe & Spiteri (2001). Zaki & Durbin (2006) found that the free-stream modes penetrate less under adverse and more under favorable pressure gradient into the boundary layer than in Blasius flow; nonetheless, transition onset and completion are moved upstream for the former and downstream for the latter pressure distribution. The authors conclude that deep penetration of the free-stream modes is not crucial for the receptivity process in two-dimensional boundary layers.

Receptivity mechanisms in three-dimensional swept-plate flow, however, are much less studied than in Blasius flow, as stated by Saric *et al.* (2003). Results from Direct Numerical Simulations (DNS) with a spectral method are herein presented to characterize the receptivity of three-dimensional boundary layers. A spatial approach is employed, capturing non-parallel effects on receptivity due to the streamwise evolution of the mean flow. The focus lies on crossflow vortices, as well. Two perturbations are considered: localized roughness elements at the wall and vortical disturbances in the free-stream. Three receptivity mechanisms are investigated: steady receptivity to roughness, unsteady

receptivity to free-stream vorticity and unsteady receptivity due to scattering of a vortical mode at a localized roughness element. The first two mechanisms depend on the amplitude of the roughness element and the free-stream-mode, respectively, while the third receptivity process involves the product of two disturbance amplitudes. The three mechanisms are characterized in terms of a receptivity coefficient as a measure for their efficiency.

The paper is organized in the following fashion: Section 2 discusses the base flow (2.1), the numerical method (2.2) and the modelling of the surface-roughness element and the vortical free-stream disturbance (2.3). Section 3 focuses on steady receptivity to localized surface roughness, and section 4 deals with direct unsteady receptivity to a vortical free-stream mode. The advection of single vortical modes along a plate with localized roughness defines the third receptivity process being investigated in section 5. In section 6 the efficiency of the receptivity processes for stationary and travelling cross-flow instability is compared. The results are discussed and summarized in section 7.

2. Flow configuration and numerical approach

2.1. *Base flow*

The flow over a swept flat plate subject to a chordwise pressure gradient is considered, a frequently studied prototype for swept wings. The base flow is obtained through the solution of the three-dimensional time-dependent incompressible Navier-Stokes equations, initialized with the Falkner-Skan-Cooke similarity profiles. This type of flow includes most of the features of the flow over the wing – the chordwise pressure drop, the streamline curvature and the cross flow, but not the surface curvature. The pressure gradient and the curvature of the external streamlines are included in Falkner-Skan-Cooke flow by assuming the following free-stream velocity distribution

$$U_\infty(x) \equiv \frac{U^*_\infty(x^*)}{U^*_\infty(x^*_0)} = \left(\frac{x^* + x^*_0}{x^*_0}\right)^m \tag{1a}$$

$$W_\infty \equiv \frac{W^*_\infty}{U^*_\infty(x^*_0)} = \tan\phi_0 = const \ , \tag{1b}$$

where U and W are used for the chord- and spanwise mean velocity and starred quantities have physical dimensions. The exponent m denotes the flow acceleration, related to the frequently used Hartree parameter β_H via

$$m = \frac{\beta_H}{2 - \beta_H} \ . \tag{2}$$

The angle ϕ_0 is the sweep angle at the reference station x^*_0. Owing to the chordwise flow acceleration, the free-stream velocity vector is turned more and more into the x^* direction downstream, forming a curved streamline. The external streamline is sketched in figure 1, where the Falkner-Skan-Cooke base-flow profiles are shown with the coordinate system adopted. In this figure, the mean flow is decomposed along the free-stream direction at x^*_0 rather than

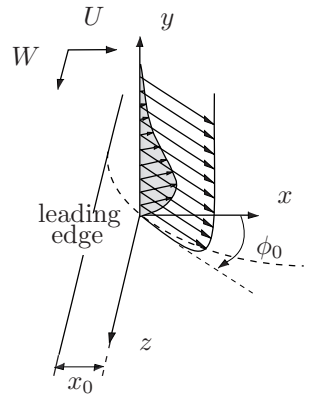

FIGURE 1. Wall-normal profiles of the streamwise and the cross-flow velocity for Falkner-Skan-Cooke boundary-layer flow.

along the chord- and spanwise coordinates x^* and z^*. This decomposition shows a non-zero velocity in the cross-stream direction inside the boundary layer – the *cross flow*, resulting from a force imbalance between the pressure and the centrifugal forces. The cross-flow profile exhibits an inflection point and supports inviscid instability, referred to as cross-flow instability. Note that instability waves propagating in the direction of the cross flow have negative spanwise wavenumber β and positive chordwise wavenumber α in the chosen coordinate system.

The Falkner-Skan-Cooke boundary-layer flow is independent of the spanwise direction z^*, and is governed by the two-dimensional boundary-layer equations, see for instance Schlichting (1979). For the free-stream velocity distribution in equation (1), the boundary-layer equations for the chordwise and wall-normal mean velocities U^* and V^* can be re-arranged in a single equation by introducing the stream function $f(\eta)$, while the chordwise and the normal coordinate x^* and y^* can be replaced by one single similarity variable η,

$$\eta = \sqrt{\frac{m+1}{2}\frac{U_\infty^*(x^*)}{\nu^* x^*}}\, y^* \quad . \tag{3}$$

If the spanwise velocity W^* is expressed as $W^* = W_\infty^* g(\eta)$, the boundary-layer equations can be transformed into a set of ordinary differential equations for $f(\eta)$ and $g(\eta)$,

$$f''' + f f'' + \beta_H (1 - f'^2) \;=\; 0 \tag{4a}$$

$$g'' + f g' \;=\; 0 \tag{4b}$$

with boundary conditions

$$\eta = 0 \quad : \qquad f = f' = g = 0 \tag{5a}$$

$$\eta \to \infty \quad : \qquad f \to 1, \;\; g \to 1 \quad . \tag{5b}$$

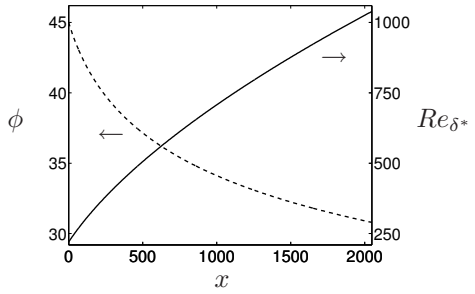

FIGURE 2. Reynolds number (——) and external streamline angle (----) as a function of the chordwise coordinate.

Self-similar profiles for the chordwise and the spanwise velocity U^* and W^* are obtained from $f'(\eta)$ and $g(\eta)$. They are referred to as the Falkner-Skan-Cooke similarity profiles in literature. Further details can be found in Schmid & Henningson (2001) or Högberg & Henningson (1998).

Throughout the remainder of this paper non-dimensional variables are used. Lengths are made dimensionless by the chordwise boundary-layer displacement thickness $\delta_0^* \equiv \delta^*(x_0^*)$ at the reference location x_0^* and velocities by the chordwise free-stream velocity $U_{\infty,0}^* \equiv U_\infty^*(x_0^*)$. The dimensionless reference station x_0 is located downstream of the leading edge of the plate and corresponds to the inflow plane of the computational domain. The reference length δ_0^* and the reference velocity $U_{\infty,0}^*$ define the Reynolds number at the computational inlet,

$$Re_{\delta_0^*} = \frac{U_{\infty,0}^* \delta_0^*}{\nu^*} \quad , \tag{6}$$

where ν^* is the kinematic viscosity. The local Reynolds number Re_{δ^*} is defined by replacing δ_0^* and $U_{\infty,0}^*$ in (6) by their local values $\delta^*(x)$ and $U_\infty^*(x)$. Figure 2 shows the relation between the local Reynolds number Re_{δ^*} and the chordwise coordinate x (solid line). Also the local angle ϕ of the external streamline is displayed versus x (dashed line).

The inflow Reynolds number is $Re_{\delta_0^*} = 220$ for most of the present results, corresponding to an inflow station at $x_0 = 167\delta_0^*$ downstream of the leading edge. The parameters m and ϕ_0 in equation (1) are chosen to obtain conditions similar to those of the airfoil experiments at Arizona State University by Reibert *et al.* (1996). These authors report among other results the N-factor of the steady cross-flow instability wave with $12mm$ spanwise wavelength at different chordwise stations. The local N-factor measured on the swept airfoil at 10% chord is approximately obtained at the corresponding station on the swept flat plate, if $m = 0.2$, or $\beta_H = 0.333$, is selected. In addition, this value gives a chordwise free-stream velocity distribution, which matches sufficiently well the c_p distribution reported by Reibert *et al.* (1996). The sweep angle at x_0^* is set to $\phi_0 = 45°$, as in the experiment. The cross-flow component is most pronounced at this angle, and the cross-flow instability waves dominate over other types of

instabilities. Also note that the streamwise and spanwise free-stream velocity are equal at the reference location for $\phi_0 = 45°$, i.e. $U_\infty(x_0) = W_\infty(x_0) = 1$.

2.2. *Numerical method*

The present results are obtained by means of a simulation code based on spectral methods to solve the three-dimensional time-dependent incompressible Navier-Stokes equations, see Chevalier *et al.* (2007). The algorithm builds on a Fourier representation along the chord- and spanwise coordinates x and z and on Chebyshev polynomials in the wall-normal direction y, together with a pseudo-spectral treatment of the nonlinear terms. The time integration is based on a four-step third-order Runge-Kutta method for the nonlinear terms and a second-order Crank-Nicolson scheme for the linear terms. Aliasing errors from the computation of the nonlinear terms are removed in wall-parallel planes by the 3/2-rule, whereas a grid refinement normal to the plate has turned out to be more convenient than dealiasing.

The swept-plate boundary layer develops along the chordwise direction, while the streamlines change continuously direction. For the simulation of such spatially evolving flows the required chordwise periodicity is established by the implementation of a "fringe region" at the downstream end of the computational domain, as described by Nordström *et al.* (1999). In this region the velocity field $\vec{\mathcal{U}}$ is forced to the desired velocity profiles $\vec{\mathcal{U}}_0$ by an additional term in the Navier-Stokes equations. Here, $\vec{\mathcal{U}}$ is used for the instantaneous velocity field to distinguish it from the base flow $\vec{U}$. $\vec{\mathcal{U}}_0$ indicates the desired inflow, i.e. the Falkner-Skan-Cooke similarity profiles, and may also contain incoming disturbances. The equation solved is,

$$\frac{\partial \vec{\mathcal{U}}}{\partial t} = \mathcal{NS}(\vec{\mathcal{U}}) + \lambda(x)(\vec{\mathcal{U}}_0 - \vec{\mathcal{U}}) \quad , \tag{7}$$

where $\mathcal{NS}$ denotes the right-hand side of the momentum equations, and $\lambda(x)$ is a smooth forcing function, being non-zero only in the fringe region.

Along the plate, no-slip conditions apply for the basic and the perturbed flow in the case of vortical free-stream perturbation, while non-homogeneous boundary-conditions are employed to model the surface roughness, see subsection 2.3. At the free-stream boundary, a von-Neumann condition is used for the computations with free-stream vortical modes, and the computational domain is chosen high enough to ensure independence of the boundary-layer response from the location of and the conditions at the top boundary. To compute the base flow and the disturbed flow in the case of surface roughness the asymptotic condition proposed by Malik *et al.* (1985) is employed,

$$y = y_\infty : \qquad \frac{\partial \hat{\vec{u}}}{\partial y} + \sqrt{\alpha^2 + \beta^2}\,\hat{\vec{u}} = \frac{\partial \hat{\vec{U}}}{\partial y} + \sqrt{\alpha^2 + \beta^2}\,\hat{\vec{U}} \quad . \tag{8}$$

This condition is equivalent to the requirement of zero vorticity at the free-stream boundary y_∞, allowing to place it nearer the boundary layer, and it

is applied in Fourier space, as indicated by the hat. $\vec{U}$ stands for the mean flow, $\vec{u}$ for the disturbance velocity and α and β for the chord- and spanwise wavenumber, respectively. As the mean flow is independent of and the perturbed flow periodic in the spanwise direction z, cyclic boundary conditions are applied along z.

The simulation code provides the possibility of solving the nonlinear and the linearized perturbation equations about any three-dimensional base flow. Herein, the linearized perturbation equations are solved for the studies of direct receptivity to roughness and free-stream vortices presented in the sections 3 and 4 and the nonlinear equations for the unsteady receptivity problem to free-stream vorticity in combination with roughness described in section 5.

2.3. *Disturbance generation*

In the present paper the receptivity of the three-dimensional swept-plate boundary layer is studied for two different types of external disturbances – steady roughness elements on the plate surface and unsteady vortical disturbances in the free stream. This section reports how these two types of disturbances are modelled and implemented in the simulation code.

2.3.1. *Surface roughness*

A chordwise localized, spanwise periodic roughness element

$$h(x,z) = \varepsilon_h \cdot h_x(x) \cdot \sin(\beta_R z) \tag{9}$$

is placed downstream of the inflow plane x_0. ε_h is a small parameter describing the maximum amplitude of the roughness bump, and $\beta_R = 2\pi/L_z$ is the spanwise wavenumber of the roughness bump. The spanwise length scale of the roughness element and the spanwise width L_z of the computational domain are hence identical. Roughness elements of different spanwise scales will be considered separately, owing to the assumption of linear flow behavior and the spanwise homogeneity of the base flow. The chordwise shape $h_x(x)$ is

$$h_x(x) = \left[S\left(\frac{x - h_{start}}{h_{rise}}\right) - S\left(\frac{x - h_{end}}{h_{fall}} + 1\right)\right] \quad , \tag{10}$$

where S is a smooth step function,

$$S(\xi) = \begin{cases} 0, & \xi \le 0 \\ 1/\left(1 + e^{(1/(\xi-1)+1/\xi)}\right), & 0 < \xi < 1 \\ 1 & \xi \ge 1 \end{cases} \quad . \tag{11}$$

The parameters h_{start}, h_{end}, h_{rise} and h_{fall} in (10) indicate the start and end station of the bump, i.e. $h_x(x) \neq 0$ on $[h_{start}, h_{end}]$, and the extension of the rising and the falling flank of the smooth step. The roughness element is not meshed but modelled by non-homogeneous boundary conditions along the plate. The no-slip conditions along the bump contour $h(x,z)$ are projected from

the bump surface to the undisturbed wall $y = 0$ via a Taylor series expansion,

$$\begin{pmatrix} u \\ v \\ w \end{pmatrix}_0 = \begin{cases} \begin{pmatrix} -h(x,z)\frac{\partial U}{\partial y} \\ 0 \\ -h(x,z)\frac{\partial W}{\partial y} \end{pmatrix}_0 , & h_{start} \le x \le h_{end} \\ \vec{0} , & \text{elsewhere} \end{cases} , \tag{12}$$

where u, v and w are the components of the disturbance velocity. Since the roughness height ε_h is assumed to be small, the Taylor series is truncated at first order. The parameters used in equations (9) and (10) are specified when presenting the results in section 3, where the model for roughness receptivity will be motivated in the context of previous studies reported in literature.

2.3.2. *Free-stream and boundary-layer modes*

The unsteady free-stream disturbance is modelled by adding a single vortical mode to the base flow in the fringe region. To analyze the effect of single waves of specific wavenumbers and frequencies Fourier modes would be a natural choice. However, in the presence of the plate the vortical mode has to decay smoothly to zero towards the wall. Eigenfunctions associated with the continuous wavenumber spectrum of the Orr-Sommerfeld/Squire operator for three-dimensional boundary-layer flows are therefore used to represent the free-stream modes, as for example in Jacobs & Durbin (1998) and Brandt *et al.* (2004). These continuous-spectrum eigenfunctions are sometimes also denoted *continuous modes*, while the eigenfunctions from the discrete wavenumber spectrum of the Orr-Sommerfeld/Squire operator are called *discrete modes*.

Grosch & Salwen (1978) first introduced the concept of the continuous spectrum for the Orr-Sommerfeld/Squire operator by relaxing the free-stream boundary conditions at $y \to \infty$. The derivation is outlined here since it is presented for the first time for three-dimensional boundary layers. In the limit $y \to \infty$ the Orr-Sommerfeld/Squire system simplifies to a set of two decoupled homogeneous ordinary differential equations with constant coefficients,

$$(\mathcal{D}^2 - \alpha^2 - \beta^2)^2\tilde{v} - iRe_{\delta^*}(\alpha U_\infty + \beta W_\infty - \omega)(\mathcal{D}^2 - \alpha^2 - \beta^2)\tilde{v} = 0 \tag{13a}$$

$$(\mathcal{D}^2 - \alpha^2 - \beta^2)\tilde{\eta} - iRe_{\delta^*}(\alpha U_\infty + \beta W_\infty - \omega)\tilde{\eta} = 0 \ . \tag{13b}$$

$\tilde{v}$ and $\tilde{\eta}$ are the amplitude functions in spectral space for the normal velocity v and vorticity η of the continuous Orr-Sommerfeld/Squire eigenmodes, α is the chordwise wavenumber and $\mathcal{D} = \mathrm{d}/\mathrm{d}y$. Defining

$$\gamma^2 \equiv -iRe_{\delta^*}(\alpha U_\infty + \beta W_\infty - \omega) - \alpha^2 - \beta^2 \ , \tag{14}$$

(13) can be re-written as

$$(\mathcal{D}^2 - \alpha^2 - \beta^2)(\mathcal{D}^2 + \gamma^2)\tilde{v} = 0 \tag{15a}$$

$$(\mathcal{D}^2 + \gamma^2)\tilde{\eta} = 0 \ . \tag{15b}$$

Further, equation (14) can be re-ordered to obtain a quadratic equation in α with solution

$$\alpha = \frac{i}{2}[\sqrt{(Re_{\delta^*}U_\infty)^2 + 4(iRe_{\delta^*}(\beta W_\infty - \omega) + \beta^2 + \gamma^2)} - Re_{\delta^*}U_\infty] \quad , \qquad (16)$$

which is the dispersion relation for the continuous Orr-Sommerfeld/Squire eigenmodes. The term $(\mathcal{D}^2 + \gamma^2)$ in (15) suggests the interpretation of γ as a wall-normal wavenumber. The solution to (15) reads,

$$\tilde{v} = Ae^{-i\gamma y} + Be^{i\gamma y} + Ce^{-\sqrt{\alpha^2+\beta^2}y} + De^{\sqrt{\alpha^2+\beta^2}y} \qquad (17a)$$

$$\tilde{\eta} = Ee^{-i\gamma y} + Fe^{i\gamma y} \quad . \qquad (17b)$$

The constants A through F result from the boundary conditions on the plate and in the outer flow. To avoid a non-physical "exploding" solution as $y \to \infty$, the fourth fundamental solution for $\tilde{v}$ should be dropped. In practice, to compute the free-stream modes, the upper boundary is located a sufficiently large wall-normal distance y_∞ away from the plate. There, one may impose arbitrary normalization conditions $\tilde{v}_\infty$ and $\tilde{\eta}_\infty$. The boundary conditions for $\tilde{v}$ and $\tilde{\eta}$ at the wall and in the free stream read then

$$y = 0 \quad : \qquad \tilde{v} = \mathcal{D}\tilde{v} = \tilde{\eta} = 0 \qquad (18a)$$

$$y = y_\infty \quad : \qquad \tilde{v} = \tilde{v}_\infty,\ \tilde{\eta} = \tilde{\eta}_\infty \quad . \qquad (18b)$$

These five conditions determine the constants in (17), and a shooting method can be employed to solve equations (13). Jacobs & Durbin (1998) observe, however, that shooting techniques do often not converge, in particular when ω is small. They suggest instead a method to impose a boundedness condition for the eigenfunction $\tilde{v}$ at y_∞, based on the evaluation of $(\mathcal{D}^2 + \gamma^2)\tilde{v}$ at two points y_1 and y_2 in the free stream,

$$\frac{\left[(\mathcal{D}^2 + \gamma^2)\tilde{v}\right]_{y_1}}{\left[(\mathcal{D}^2 + \gamma^2)\tilde{v}\right]_{y_2}} = e^{\sqrt{\alpha^2+\beta^2}\cdot(y_2 - y_1)} \quad . \qquad (19)$$

This amounts to a boundary-value problem for $\tilde{v}$ with the conditions (18a) at the wall and condition (19) near the free stream boundary. The normalization (18b) is then used to scale the mode to the desired energy. In summary, the spatial eigenvalue α is obtained from (16) and the associated eigenfunctions for $\tilde{v}$ and $\tilde{\eta}$ from the numerical solution of the Orr-Sommerfeld/Squire system together with the boundary conditions (18) and (19). The chordwise and spanwise spectral velocities $\tilde{u}$ and $\tilde{w}$ are computed from the definition of $\tilde{\eta}$ in conjunction with the continuity equation. The shape of a continuous eigenmode along the wall-normal coordinate y is shown in figure 3(a). Clearly, the amplitude of the eigenfunction is quenched to zero towards the plate, as desired, and oscillates in the free stream. Therefore, the continuous modes are herein also referred to as free-stream modes. Figure 3(b) shows the wall-normal amplitude for an eigenmode from the discrete spectrum of the Orr-Sommerfeld/Squire operator. Since it is large inside the boundary layer and tends to zero in the outer flow, the

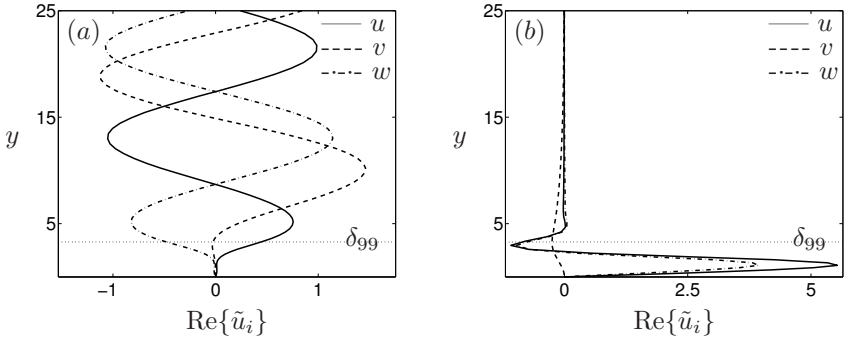

FIGURE 3. (a) Wall-normal shape of a free-stream eigenmode from the continuous spectrum of the Orr-Sommerfeld equation, $(\alpha, \beta) = (0.130, -0.140)$, $\alpha_i = 0.00081$, $\gamma = 0.377$, $\omega = -0.01$. (b) Amplitude in wall-normal direction of a travelling discrete boundary-layer eigenmode, $(\alpha, \beta) = (0.102, -0.140)$, $\alpha_i = 0.00474$, $\omega = -0.01$.

discrete modes are often called boundary-layer modes. In contrast to the free-stream modes, which are always damped, there exist unstable discrete modes in 3D boundary layers for certain parameter combinations $(m, \phi_0; Re_{\delta^*}, \beta, \omega)$, where β and ω are the spanwise wavenumber and the angular frequency of the eigenmode. The cross-flow instability waves are an example for unstable discrete modes, and the right plot of figure 3 shows indeed a cross-flow mode.

As already mentioned, the vortical free-stream mode is imposed in the fringe region and re-cycled to the inflow plane of the computational domain. Therefore, when computing the continuous mode, the Reynolds number is fixed to the inflow value $Re_{\delta_0^*}$, whereas β, γ and ω can be chosen arbitrarily. In section 4, the choice of the continuous-spectrum eigenmodes as a model for free-stream disturbances will be motivated.

To study the spatial evolution of the unstable modes, one may superimpose a discrete boundary-layer mode on the base flow in the same manner as the continuous free-stream mode. The spatial eigenvalues and eigenshapes of the discrete modes are computed by solving the spatial Orr-Sommerfeld/Squire eigenvalue problem, as described in Schmid & Henningson (2001), for instance.

2.4. *Computational domain and numerical resolution*

Table 1 compiles the dimensions L_x, L_y and L_z of the computational domain together with the corresponding resolution N_x, N_y and N_z along the spatial coordinates. Also the range of inflow Reynolds numbers $Re_{\delta_0^*}$ and the type of disturbance forcing are listed in the table. Three different computational boxes, A, B and C, have been used to obtain the results for receptivity to wall roughness, vortical free-stream modes and their combination. Note that the spanwise width L_z of the domain has been varied for Box A and B to study

TABLE 1. Dimensions and resolution of the computational domain. Inflow Reynolds number and type of disturbance forcing. "SR" stands for "surface roughness" and "FS" for "free-stream mode".

Box	$L_x \times L_y$	L_z	$N_x \times N_y \times N_z$	$Re_{\delta_0^*}$	Disturb.
A	883.2×20.0	12.0...73.0	$768 \times 65 \times 8$	220	SR
B	2048.0×50.0	23.0...73.0	$512 \times 97 \times 4$	220...353	FS
C	3072.0×50.0	33.0, 66.0, 99.0	$1536 \times 97 \times 12$	220	SR+FS

the receptivity when varying the spanwise wavenumber of the unstable waves, and that the inflow Reynolds number $Re_{\delta_0^*}$ has been also varied when studying the effect of free-stream modes. The box dimensions L_x, L_y and L_z have been scaled in such a way that the physical box dimensions $L_x\delta_0^*$, $L_y\delta_0^*$ and $L_z\delta_0^*$ and thus the resolution remain unchanged for all values of $Re_{\delta_0^*}$. The listed values of L_x, L_y and L_z for Box B refer to $Re_{\delta_0^*} = 220$.

3. Receptivity of stationary modes to localized wall roughness

It is known that surface roughness provides an efficient mechanism for the excitation of steady cross-flow instability waves if the roughness contour contains the wavenumber of the instability; see for instance Crouch (1993), Choudhari (1994) or Bertolotti (2000). The receptivity process, connecting the forcing due to the roughness element with the response of the boundary layer, is described in terms of the receptivity coefficient $C_R(\beta_R, \omega; m, \phi_0)$, where β_R is the spanwise wavenumber of the roughness, and the frequency ω is zero for steady surface roughness,

$$C_R = \frac{A_R}{\varepsilon_h \cdot H(\alpha_{CF})} \quad . \tag{20}$$

A_R is the receptivity amplitude, i.e. the amplitude of the excited steady cross-flow instability at the roughness station x_R, defined at the center of the bump. $H(\alpha_R)$ denotes the representation of the chordwise bump shape $h_x(x)$ in Fourier space, and α_{CF} is the chordwise wavenumber of the excited stationary cross-flow instability at x_R. Here, the wall-normal maximum of $\sqrt{\overline{u^2}}$ is chosen as the measure for the boundary-layer response, where u is the chordwise disturbance velocity. C_R may be interpreted as the efficiency of the forcing mechanism – here the roughness bump – in exciting the least stable eigenmode of the boundary layer – here the steady cross-flow mode. A similar definition is used in Crouch (1993), Choudhari (1994) and Ng & Crouch (1999) in the context of Finite Reynolds-Number Theory. In contrast to these studies non-parallel effects on the receptivity process are included here by employing Direct Numerical Simulation. Various roughness elements are considered, differing in their chordwise shape $h_x(x)$ as well as in their spanwise wavenumber β_R. Most of the results are obtained by using roughness with maximum amplitude ε_h being much smaller than the characteristic length δ_0^* of the basic flow such that

TABLE 2. Three different chordwise shape functions $h_x(x)$ for surface roughness. Parameters according to equations (9) and (10).

Shape	ε_h	h_{start}	h_{end}	h_{rise}	h_{fall}
I	0.021	4.6	32.2	11.5	11.5
II	0.021	9.2	27.6	6.9	6.9
III	0.021	13.8	23.0	3.45	3.45

the linearized perturbation equations are valid. In subsection 3.2 also higher roughness elements are considered and the nonlinear disturbance equations are solved. Three chordwise roughness contours are considered, with parameters compiled in table 2. In order to investigate the dependence of the receptivity coefficient C_R on the spanwise scale of the roughness, the width L_z of the domain is changed according to table 1 in the previous section. The values listed for Box A correspond to spanwise roughness wavenumbers β_R between 0.09 and 0.52.

3.1. *Low-amplitude roughness*

Figure 4 shows the boundary-layer response to perturbations caused by roughness elements of different spanwise wavenumbers β_R (thick lines). For each case a second simulation employing a smooth plate is performed, where the wall-normal velocity distribution of the stationary cross-flow eigenmode at $|\beta_{CF}| = \beta_R$ is prescribed at the inflow plane. The response of the base flow to this initial condition is displayed as a thin line in figure 4. Comparison of the thick and the thin curves reveals that the flow response in the vicinity of the roughness is characterized by transient behavior, while the downstream evolution of the boundary-layer disturbance is fully determined by the excited steady cross-flow instability. The receptivity amplitude A_R is extracted from the total disturbance (thick lines) by tracing back the contribution of the unstable cross-flow mode (thin lines) to the roughness station x_R. It can be concluded that surface roughness provides an efficient linear mechanism for the excitation of zero-frequency cross-flow instability.

Figure 4 also suggests that the efficiency of the receptivity mechanism is strongly dependent on the spanwise wavenumber of the roughness element. Further, to verify the assumption of shape independent receptivity, roughness elements of different chordwise shape are considered. These two aspects have been investigated in detail, and the result is reported in figure 5. In 5(a) the three chordwise roughness contours under consideration are displayed in physical (insertion) and in Fourier space. Depending on their spanwise wavenumber β_R these roughness elements will force different unstable boundary-layer modes with different efficiency. This is highlighted in the figure by the symbols, marking the spectral component $H(\alpha_{CF})$ for roughness elements of $\beta_R = 0.09$ ($\diamond$), 0.19 ($\circ$) and 0.44 ($\square$). $H(\alpha_{CF})$ measures to which degree the chordwise

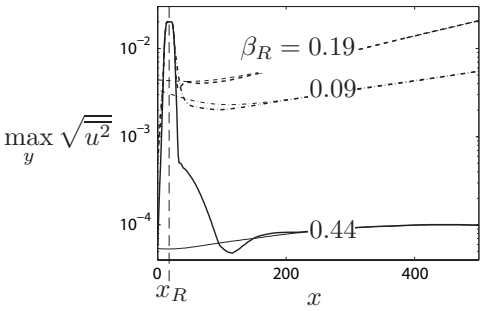

FIGURE 4. Boundary-layer response to roughness at $x_R = 18.4$ ($Re_{\delta^*} = 234$), expressed as wall-normal maximum of the chordwise disturbance-velocity amplitude (thick lines), and evolution of the excited steady cross-flow instability waves (thin lines).

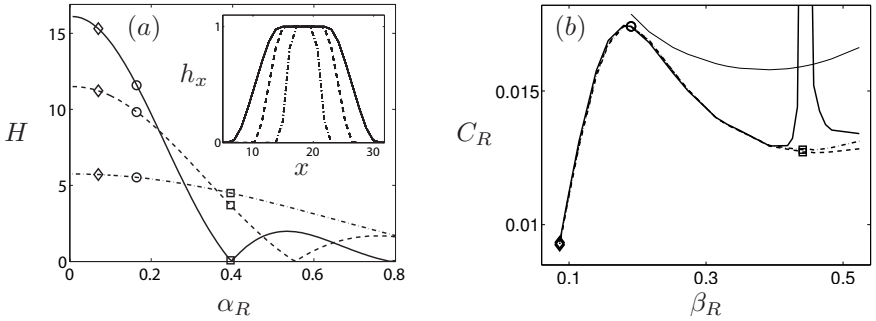

FIGURE 5. (a) Three roughness shapes in physical (insertion) and spectral space. The symbols mark the Fourier component of the spectral bump shape at the chordwise wavenumber α_{CF} of the excited steady cross-flow eigenmode (i.e. $\alpha_{CF} = \alpha_R$), shown for three spanwise wavenumbers of the roughness: $\beta_R = 0.09$ ($\diamond$), 0.19 ($\circ$) and 0.44 ($\square$). (b) Thick lines: Receptivity coefficient in spatially evolving flow versus spanwise wavenumber of the roughness for the three bump shapes in (a). The roughness is placed at $x_R = 18.4$ ($Re_{\delta^*} = 234$). The symbols correspond to those in (a). Thin solid line: Receptivity coefficient in parallel flow.

wavenumber α_{CF} of the triggered stationary cross-flow mode is represented in the three spectral shape functions. In figure 5(b) the influence of chordwise shape and spanwise wavenumber of the roughness on the receptivity coefficient is depicted. Results for receptivity in parallel boundary layers are included, as well (thin curve). They are obtained by employing the same roughness elements in parallel base flow for the Reynolds number at the roughness station, i.e.

$Re_{\delta^*} = 234$. The receptivity coefficients C_R in parallel flow could be extracted solely for wavenumbers pertaining to unstable or marginally stable cross-flow modes. Only in these cases the least stable mode is clearly distinguishable from the total disturbance further downstream. It can be concluded from figure 5(b) that non-parallel flow (thick lines) is less receptive to roughness-induced perturbations than parallel flow (thin line). In particular roughness elements of large spanwise wavenumber, triggering instabilities with short wavelengths, give lower receptivity coefficients in spatially developing flow. This is in line with the findings of Collis & Lele (1999) who demonstrated that non-parallel effects attenuate roughness-related receptivity. They used the steady solution to flow around a swept parabolic cylinder as base flow and applied a bump of Gaussian shape near the leading edge.

Two additional conclusions can be drawn from figure 5(b): (1) An optimal spanwise wavenumber, $\beta_R \approx 0.19$, can be identified, at which the receptivity process in non-parallel flow is most efficient. (2) For the three roughness contours under consideration the receptivity coefficient is independent of the specific shape over a large range of values for β_R. However, for $\beta_R \gtrsim 0.41$ the shape-independence of C_R is broken. For roughness contour I (solid line) the C_R curve exhibits a remarkable jump around $\beta_R = 0.44$. Comparing figure 5(a) and (b) reveals that this jump is occurring, as bump shape I has almost zero component $H(\alpha_{CF})$ at the instability wavenumber $(\alpha_{CF}, |\beta_{CF}|) = (0.40, 0.44)$ (square symbol). Also the amplitude A_R of the unstable eigenmode is small, if $\beta_R = 0.44$, as shown in figure 4. The receptivity coefficient C_R no longer provides a shape-independent, universal measure for receptivity to roughness, if both numerator and denominator in definition (20) become small. In such situations C_R describes the receptivity process improperly; moreover, C_R is no longer well-defined, when $H(\alpha_{CF})$ is zero. Also the receptivity coefficients computed from the roughness contours II and III start to differ for large values of β_R, i.e. when the bump is longer than the cross-flow wavelength.

Unlike in parallel flow, where the receptivity amplitude A_R of the cross-flow mode vanishes as $H(\alpha_{CF}) \to 0$, low values of A_R are still observed in downstream evolving boundary layers, even when the spectrum of the roughness element contains no energy at all at the instability wavenumber. The receptivity coefficient C_R, derived for parallel base flow, cannot capture this non-parallel effect. To provide an improved measure for roughness-related receptivity when $H(\alpha_{CF})$ becomes small, Bertolotti (2000) suggests an alternative expression for the receptivity amplitude,

$$A_R = \varepsilon_h |C_{R,0} H(\alpha_{CF}) + C_{R,1} H'(\alpha_{CF})| \ , \tag{21}$$

i.e. a second term depending on the slope $H'(\alpha_{CF}) \equiv (\mathrm{d}H/\mathrm{d}\alpha)_{\alpha_{CF}}$ is introduced. Bertolotti derives relation (21) by expanding the base flow and the disturbance in the chordwise direction about the roughness station x_R. The expansion is truncated at first order and analyzed in spectral space. As shown in Bertolotti (2000), the term $C_{R,0} H(\alpha_{CF})$ represents the contribution to A_R

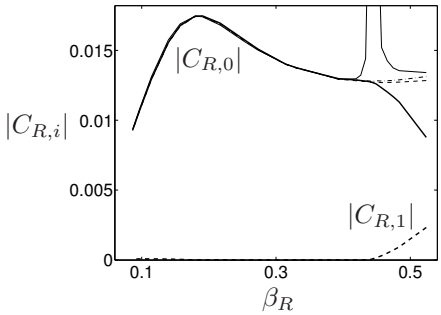

FIGURE 6. Thick lines: Receptivity coefficients $|C_{R,0}|$ (——) and $|C_{R,1}|$ (----) according to equation (21). Thin lines: Receptivity coefficient C_R, equation (20), as in figure 5(b).

at zeroth order, while $C_{R,1}H'(\alpha_{CF})$ is the first-order correction due to the non-parallel evolution of the base flow.

The zeroth- and first-order receptivity coefficients $C_{R,0}$ and $C_{R,1}$ can be extracted from the present DNS data by solving the following linear system,

$$\begin{pmatrix} C_{R,0} \\ C_{R,1} \end{pmatrix} = \frac{1}{\varepsilon_h} \begin{pmatrix} H_1 & H_1' \\ H_2 & H_2' \end{pmatrix}^{-1}_{\alpha_{CF}} \begin{pmatrix} A_{R,1} \\ A_{R,2} \end{pmatrix}_{DNS} , \tag{22}$$

using two of the roughness contours under consideration. The validity of Bertolotti's ansatz for A_R is checked by applying equation (21) with the coefficients $C_{R,0}$ and $C_{R,1}$ from (22) to results obtained when forcing with the third roughness contour,

$$A_{R,3}|_{pred} = \varepsilon_h (C_{R,0}H_3 + C_{R,1}H_3')_{\alpha_{CF}} \equiv A_{R,3}|_{DNS} \ . \tag{23}$$

$A_{R,3}|_{pred}$ denotes the wave amplitude and phase predicted by model (21), and $A_{R,3}|_{DNS}$ is the receptivity amplitude obtained by DNS. $A_{R,3}|_{pred} = A_{R,3}|_{DNS}$ is indeed obtained with good accuracy for all spanwise wavenumbers under consideration, both in terms of amplitude and phase. The receptivity coefficients $|C_{R,0}|$ and $|C_{R,1}|$ are plotted versus β_R in figure 6. Clearly, there is very good agreement between the standard receptivity coefficient C_R and the zeroth-order coefficient $|C_{R,0}|$ for $\beta_R \lesssim 0.41$. In this regime receptivity to roughness is adequately described by a receptivity coefficient based only on $H(\alpha_{CF})$. For $\beta_R \gtrsim 0.41$, however, the correction term $C_{R,1}H'(\alpha_{CF})$ is no longer negligible. $|C_{R,0}|$ drops down in this region and does no longer exhibit the peak seen in the curve for C_R. $|C_{R,0}|$ in combination with $|C_{R,1}|$ is thus a more appropriate measure for receptivity to roughness bumps with very low spectral amplitude $H(\alpha_{CF})$ than the standard coefficient C_R. Following Bertolotti (2000) who attributes the contribution proportional to $H'(\alpha_{CF})$ to the non-parallel nature of the base flow, we conclude from figure 6 that the non-parallel correction $C_{R,1}H'(\alpha_{CF})$ is most important for large wavenumbers of the triggered unstable boundary-layer mode. The wavelength of the cross-flow disturbance is

then considerably shorter than the chordwise extent of the roughness element. Since $|C_{R,0}|$ and $|C_{R,1}|$ fulfill equation (21) for all three roughness contours, they represent to first order a shape-independent, universal measure for receptivity to roughness. To summarize, the non-parallel nature of the base flow becomes manifest in two ways: a stronger effect over the whole wavenumber range plotted in figure 5(b) and a weaker effect only for large wavenumbers displayed in figure 6.

A roughness element with even larger chordwise length may be designed such that the spectral shape has a zero crossing at $(\alpha_{CF}, \beta_{CF}) = (0.17, -0.19)$, that is, at the most receptive wavenumber. We have performed a simulation with a bump with $H(\alpha_{CF} = 0.17) = 9.6 \cdot 10^{-2}$, which is about 60 times smaller than the spectral amplitude of the short bump contour III at that wavenumber. The difference in amplitude A_R of the triggered unstable mode is, however, much less; A_R is $9.6 \cdot 10^{-4}$ for the long versus $1.7 \cdot 10^{-3}$ for the short roughness element. The curve for the classical receptivity coefficient C_R would again exhibit large peaks at every zero crossing of the spectral contour H, while the curves for $|C_{R,0}|$ and $|C_{R,1}|$ look smooth. They differ, however, from the corresponding curves in figure 6 in that the contribution of the first-order coefficient $|C_{R,1}|$ becomes stronger. We conclude that the receptivity coefficients $|C_{R,0}|$ and $|C_{R,1}|$ preserve their independence of roughness shape only within a limited range of bump length. For longer, less localized roughness elements, contributions related to higher derivatives of H are likely to come into play. We want to emphasize, however, that the classical receptivity coefficient C_R is nevertheless an appropriate representation of roughness receptivity in the framework of localized receptivity.

The response of the base flow to disturbances introduced by localized roughness elements at different chordwise stations x_R is studied next. Bump shape III is considered here. The spanwise scale of the roughness is chosen to be $\lambda_z = 50$ inflow displacement thicknesses, corresponding to $\beta_R = 0.126$. These values match approximatively the spanwise scale of the roughness array in the experiments by Reibert *et al.* (1996). As shown in the previous section the standard receptivity coefficient C_R is independent of the roughness shape at $\beta_R = 0.126$ and can thus be used here. The dependence of C_R on the chordwise position x_R of the roughness element is depicted in figure 7 (solid line). The dashed line shows the effective receptivity coefficient $C_{R,eff}$, compensating for the local decay or growth of the excited steady cross-flow instability at x_R,

$$C_{R,eff} = \frac{C_R}{e^{N_R}} = C_R \frac{A_I}{A_R} = \frac{A_I}{\varepsilon_h H(\alpha_{CF})} \quad , \tag{24}$$

where N_R is the N-factor of the cross-flow disturbance at x_R, and A_I is the amplitude at the first neutral point of the cross-flow mode. While C_R is a measure for the receptivity process only, $C_{R,eff}$ can be used to determine the disturbance amplitude $A(x)$ in the linear regime downstream of the roughness,

$$A(x) = \varepsilon_h H(\alpha_{CF}) C_{R,eff} e^{N(x)}. \tag{25}$$

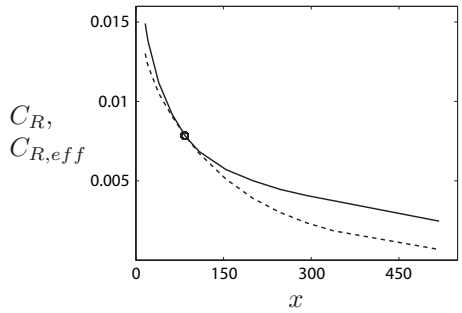

FIGURE 7. Receptivity coefficient for surface roughness as a function of the chordwise station x_R of the roughness element (——). Roughness shape III is used, and $\beta_R = 0.126$. Effective receptivity coefficient $C_{R,eff}$ (----). The circle marks the first neutral point of the excited steady cross-flow mode.

The receptivity process is most efficient upstream of the first neutral point and drops down rapidly downstream of it. This is in line with results for parallel flow, obtained by Finite Reynolds-Number Theory, see for example Crouch (1993).

3.2. *Larger-amplitude roughness*

In the previous section receptivity to localized surface roughness of low amplitude was discussed. The amplitude A_R of the excited unstable cross-flow mode is then proportional to the height ε_h of these tiny roughness elements, leading to constant receptivity coefficients as ε_h is changed. In this section receptivity to roughness with higher amplitude is investigated to identify at which bump height nonlinear behavior starts to affect the receptivity. The roughness elements used here are of shape I, II and III and have a fixed spanwise wavenumber of $\beta_R = 0.19$. This choice guarantees efficient receptivity and negligible nonparallel effects, as seen before. The height of the roughness elements is chosen in the range $0.02 \leq \varepsilon \leq 0.2$. At the highest bump amplitude $\varepsilon = 0.2$ a region of linear growth of the unstable mode is no longer clearly identified, whereas the flow downstream of the roughness is characterized by saturating cross-flow modes. Nonlinear behavior is hence apparent at this roughness amplitude. But also below this height nonlinearity has an effect on receptivity, as illustrated in figure 8. Beyond $\varepsilon = 0.05$ C_R becomes dependent on both the amplitude and the shape of the roughness element. In particular the dashed-dotted curve obtained by inserting the shortest roughness element (shape III) deviates to lower values from the constant C_R found for low roughness height. Bump I, conversely, retains a constant receptivity efficiency even for nonlinearly behaving cross-flow modes. In summary, the deviation of C_R from its value for tiny roughness remains rather small for the plotted range of roughness amplitudes,

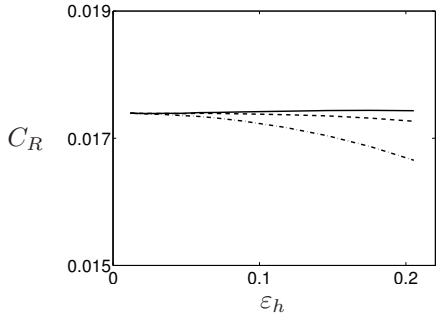

FIGURE 8. Effect of bump height on receptivity to surface roughness. $\beta_R = 0.19$. Bump shape I (——), II (----) and III (-·-·-).

i.e. nonlinearity has a weaker effect on the receptivity process than on the subsequent growth of the triggered instability (saturation).

4. Receptivity of travelling cross-flow modes to vortical free-stream disturbances

In this section we investigate whether three-dimensional boundary-layer flow over a smooth plate is receptive to vortical free-stream perturbations. The disturbance is modelled by means of eigenfunctions from the continuous wavenumber spectrum of the Orr-Sommerfeld/Squire operator, which are often called continuous modes. Since free-stream turbulence is in general an unsteady phenomenon, the study is restricted to the unsteady receptivity process. In particular, receptivity to one single free-stream mode is examined, nonlinear interaction with other modes being neglected. The computation of the Orr-Sommerfeld solution $\tilde{v}$ and the Squire solution $\tilde{\eta}$ in the free stream has been outlined in subsection 2.3.2. The chordwise and spanwise disturbance velocities $\tilde{u}$ and $\tilde{w}$ can be calculated from the normal velocity $\tilde{v}$ and vorticity $\tilde{\eta}$ as

$$\tilde{u} = \tilde{u}_{OS} + \tilde{u}_{Sq} = \frac{i\alpha}{\alpha^2+\beta^2}\mathcal{D}\tilde{v} - \frac{i\beta}{\alpha^2+\beta^2}\tilde{\eta} \ , \tag{26a}$$

$$\tilde{w} = \tilde{w}_{OS} + \tilde{w}_{Sq} = \frac{i\beta}{\alpha^2+\beta^2}\mathcal{D}\tilde{v} + \frac{i\alpha}{\alpha^2+\beta^2}\tilde{\eta} \ . \tag{26b}$$

The Orr-Sommerfeld and the Squire solution are hence coupled in the $\tilde{u}$ and the $\tilde{w}$ component of the eigenmode $(\tilde{u}, \tilde{v}, \tilde{w}, \tilde{\eta})^T$. Instead of such a full continuous-spectrum mode a continuous mode without the $\tilde{\eta}$ contribution can be considered, i.e. $(\tilde{u}_{OS}, \tilde{v}, \tilde{w}_{OS}, 0)^T$. As only the contribution of the Orr-Sommerfeld equation is present in such a mode, it is referred to as Orr-Sommerfeld mode here. The use of Orr-Sommerfeld modes as a model for free-stream vorticity can be justified as follows. In the flow upstream of the leading edge of the plate there is no coupling between normal velocity and vorticity. Homogeneous

isotropic turbulence is an example of an incoming flow with independent evolution of $\tilde{v}$ and $\tilde{\eta}$. The coupling sets in, when the flow attaches to the plate at the leading edge. The Orr-Sommerfeld mode forces the corresponding set of Squire modes and develops gradually into a full mode. This is a viscous, slow process. In the simulations the free-stream mode is introduced a short distance downstream of the leading edge, where the forcing of the Squire modes and thus the coupling between $\tilde{v}$ and $\tilde{\eta}$ has just been initiated. For the cases considered here the shape of the free-stream disturbance is still similar to that of the Orr-Sommerfeld mode without the $\tilde{\eta}$ contribution.

4.1. *Penetration depth and chordwise decay*

Two different characteristics of the Orr-Sommerfeld free-stream modes have been identified to play a role for unsteady receptivity: their ability to penetrate into the boundary layer and their downstream decay rate. Jacobs & Durbin (1998) introduce the penetration depth Δ as the distance from the boundary-layer edge, at which the magnitude of the eigenshape $\tilde{v}$ has decayed to 1% of its free-stream value. They obtained a relationship for Blasius flow between Δ, frequency ω and Reynolds number $Re = \sqrt{U_\infty^* x^*/\nu^*}$,

$$\Delta \sim (\omega Re)^{-b} \quad , \tag{27}$$

where the exponent b takes values of the order of 0.1 depending on the wall-normal wavenumber γ. Zaki & Durbin (2005) point out that not only the penetration depth, but also the decay rate of the vortical disturbance has to be considered. The free-stream mode is efficient in perturbing the boundary layer if it penetrates deeply into it or if it decays slowly and thus carries enough energy downstream. At fixed Re and ω these two features are competitive: Deeply penetrating modes with large γ decay rapidly, while modes with smaller γ penetrate and decay less. Maslowe & Spiteri (2001) present a similar analysis for the continuous-spectrum modes of a two-dimensional boundary layer in a streamwise pressure gradient modelled by the Falkner-Skan similarity solution. They find that relation 27 holds also for the adverse pressure-gradient boundary layer. However, the constant of proportionality is different, as shown in Zaki & Durbin (2006): Penetration depth is reduced in adverse and enhanced in favorable pressure gradient as compared to Blasius flow.

We perform a similar investigation of penetration depth and decay rate of the continuous-spectrum modes in the three-dimensional boundary layer. A parametric study for free-stream modes in Falkner-Skan-Cooke flow is presented in figure 9. The behavior of the penetration depth Δ (solid) and decay rate α_i (dashed) of the continuous Orr-Sommerfeld modes is shown for ranges of Reynolds number (a), angular frequency (b), wall-normal wavenumber (c) and spanwise wavenumber (d). Δ is normalized by the 99% boundary-layer thickness and is defined as the distance below the boundary-layer edge, at which the chordwise disturbance amplitude $|\tilde{u}|$ has dropped to 5% of its maximum value in the outer flow. Figure 9(a), (b) and (c) reveal that deeply penetrating

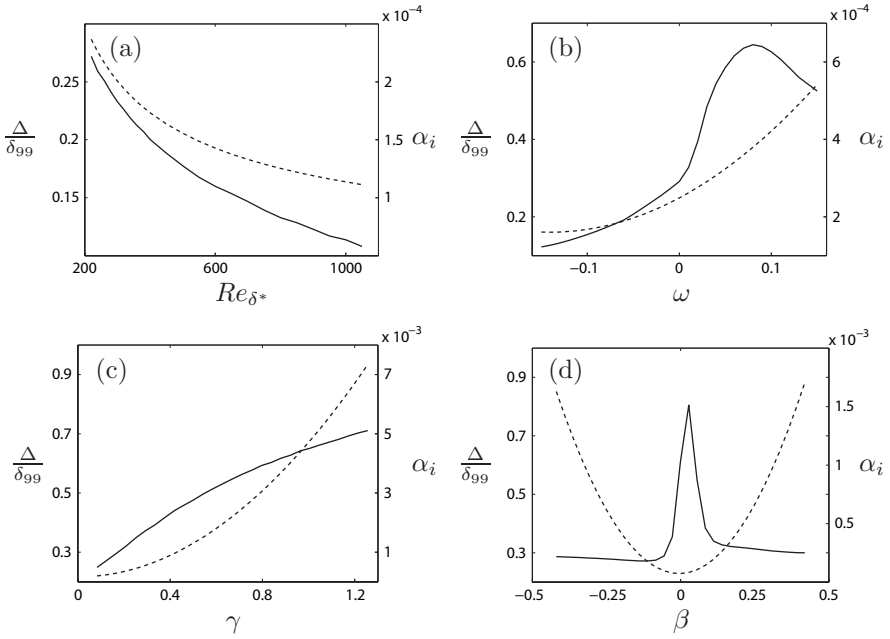

FIGURE 9. Penetration depth Δ (——) and decay rate α_i (- - -) of the continuous Orr-Sommerfeld modes for ranges of Reynolds number Re_δ (a), angular frequency ω (b), wall-normal wavenumber γ (c) and spanwise wavenumber β (d). The plots are based on $(Re_\delta, \omega; \beta, \gamma)$=(220,-0.01;-0.14,0.126).

free-stream modes suffer indeed from a strong decay. In figure 9(a) a large penetration depth of more than 25% of the boundary-layer thickness is obtained at small Reynolds numbers, i.e. close to the leading edge of the plate, while Δ quickly drops downstream.

It is interesting that the penetration depth assumes large values in the positive ω half-plane in figure 9(b) and that the maximum is obtained at $\omega = 0.08$. This is in contrast to the result for Blasius flow, equation (27), where Δ approaches its maximum for $\omega \to 0$. The most unstable cross-flow modes are, however, obtained for $\omega < 0$, i.e. the negative frequency range is more relevant for the study of receptivity to continuous modes. It should be noticed that the counterpart of ω in the dispersion relation for Blasius flow is the quantity $(\omega - \beta W_\infty)$ in equation (16) here, which is positive in figure 9(b) also in the range of negative ω. We could not find a relation for the penetration depth Δ corresponding to equation (27), neither in terms of ωRe nor of $(\omega - \beta W_\infty)Re$. In light of the observation by Maslowe & Spiteri (2001) that the free-stream modes in Falkner-Skan flow behave similar to those in Blasius flow, it can be concluded that the different behavior of Δ with ω, β and Re is a result of the spanwise component of the base flow.

As shown in figure 9(c) penetration depth grows with increasing wall-normal wavenumber. The free-stream modes of smallest normal length scale penetrate the boundary layer to a depth of up to 70% of its thickness, although they die out rapidly.

In figure 9(d) a region of deep penetration exists, while the decay rate is small. The curve for Δ exhibits a remarkable peak at small spanwise wavenumbers. These waves have also a small chordwise wavenumber. At $\beta = 0$ the continuous mode becomes a two-dimensional wave. The most deeply penetrating free-stream modes are thus long waves propagating nearly perpendicular to the leading edge. However, these modes are irrelevant for the present receptivity study, since they do not trigger boundary-layer instabilities. The most unstable travelling eigenmodes are found at negative values of β, while $\alpha > 0$. These disturbances propagate in the direction of the cross flow. In this wavenumber regime the penetration depth for free-stream vorticity is almost constant at a level of $\simeq 28\%$.

To conclude, comparison with the results in Jacobs & Durbin (1998) reveals that in Falkner-Skan-Cooke flow, mean shear hampers the penetration of free-stream vorticity into the boundary layer much more than in Blasius flow.

4.2. *Scale conversion*

Direct excitation of travelling boundary-layer instability waves requires an external perturbation with matching wavenumber vector and frequency. Free-stream disturbances, however, have in general different length scales than the unstable eigenmode of the boundary layer. Goldstein (1985) demonstrates for Blasius flow that there is nonetheless a receptivity mechanism to acoustic free-stream disturbances, triggering Tollmien-Schlichting (TS) instability. He introduces the concept of scale reduction, by which the large length scale of the acoustic wave is converted into the smaller scale of the TS wave. Goldstein (1985) shows that the scale-conversion process is efficient in particular around a surface irregularity. Scattering of acoustic waves at roughness elements, suction holes or other types of wall disturbances has indeed been shown to be an efficient receptivity mechanism for TS waves, e.g. in Crouch (1992), Choudhari & Streett (1992) and Crouch & Spalart (1995).

Also in swept-plate flow the horizontal length scales of the free-stream perturbations differ from those of the boundary-layer disturbances. In Figure 10 the angle $\psi = \arctan(\alpha_r/|\beta|)$ of the horizontal wavenumber vector of a vortical free-stream mode and a travelling cross-flow mode is compared. Both modes are computed at a frequency of $\omega = -0.01$ and a spanwise wavenumber of $\beta = -0.14$. The angle of the outer streamline is also plotted for comparison, showing that the free-stream vortex is closer aligned with the external streamlines than the unsteady cross-flow wave. Clearly, the wavenumber vectors for the free-stream wave and the cross-flow mode are not aligned at any location, which reflects their different chordwise wavenumber $\alpha_r = \mathrm{Re}\{\alpha\}$. Specifically, the chordwise wavenumber of the travelling cross-flow mode is smaller than that

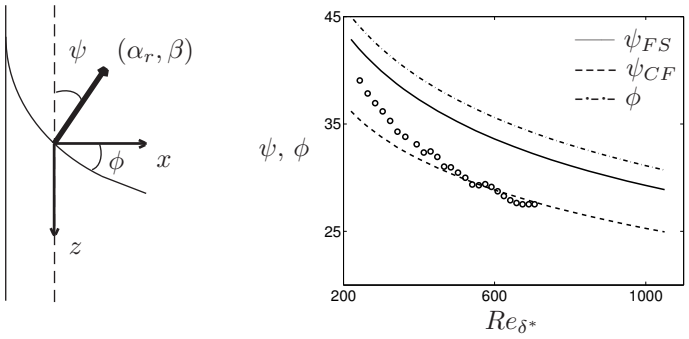

FIGURE 10. Horizontal wavenumber angle $\psi = \arctan(\alpha_r/|\beta|)$ for the continuous Orr-Sommerfeld mode ($\omega = -0.01$, $\beta = -0.14$, $\gamma = 0.126$, ——) and the excited travelling cross-flow wave (----) and local angle ϕ of the external streamline (-·-·-). The symbols mark the wave angle of the forced boundary-layer disturbance and are extracted from DNS data.

of the free-stream disturbance. Further, the relative misalignment between the two waves is nearly constant versus Re_{δ^*}. Therefore there is no direct resonance between the vortical free-stream disturbance and the unsteady cross-flow instability at any location in the flow, and it can be concluded that length-scale conversion will be a key element for unsteady receptivity also in three-dimensional boundary layers. This becomes in fact evident in figure 10 by the symbols showing the wave-vector angle of the largest fluctuations inside the boundary layer, when it is forced by a vortical free-stream mode. These data have been extracted from a DNS velocity field. Upstream, the wave vector of the forced disturbance is closer aligned with the free-stream mode, while it turns into the direction of the excited cross-flow mode further downstream. It becomes also apparent that in contrast to Blasius flow, the chordwise length scale of the free-stream disturbance needs to be enhanced rather than reduced to match that of the boundary-layer eigenmode. Since scale conversion relies on rapid mean-flow changes, it is expected to be efficient in particular in the strongly developing upstream region of the boundary layer and around wall roughness.

4.3. *Receptivity coefficient*

Receptivity of the Blasius boundary layer to vortical disturbances in the outer flow has been thoroughly investigated in the past. Different models for free-stream vorticity have been employed: streamwise vortices by Bertolotti (1997) and Bertolotti & Kendall (1997), oblique waves by Berlin & Henningson (1999) and eigenmodes from the continuous spectrum of the Orr-Sommerfeld/Squire operator by e.g. Jacobs & Durbin (2001), Brandt *et al.* (2002), Brandt *et al.* (2004) and Zaki & Durbin (2005). In all cases the receptivity process was characterized by the formation of streamwise elongated structures, referred to

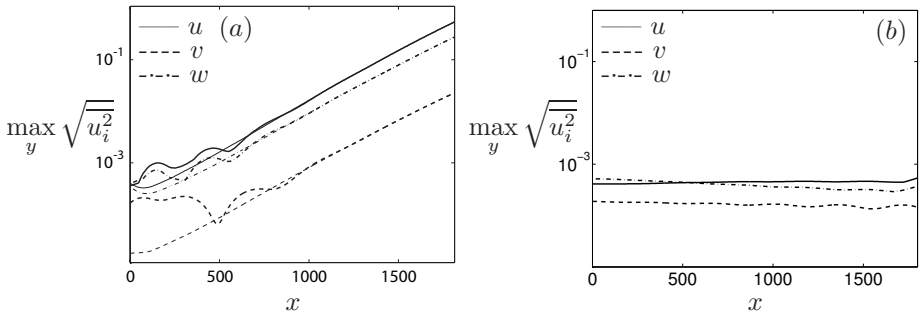

FIGURE 11. (a) Response of the non-parallel three-dimensional boundary layer to free-stream vorticity. Thick lines: Spatial evolution of the boundary-layer disturbance, excited by a continuous Orr-Sommerfeld mode ($\omega = -0.01$, $\beta = -0.14$, $\gamma = 0.126$) at $Re_{\delta^*} = 220$. Thin lines: Spatial evolution of the corresponding cross-flow instability wave. (b) Response of a parallel Falkner-Skan-Cooke boundary layer at $Re_{\delta^*} = 360$ to a continuous Orr-Sommerfeld mode ($\omega = -0.01$, $\beta = -0.14$, $\gamma = 0.126$).

as streaks, while the excitation of TS waves was bypassed. The streaks are not eigenmodes of the base flow and undergo algebraic instead of exponential growth.

In this paper we investigate the receptivity mechanism to free-stream vorticity in the three-dimensional swept-plate boundary layer. Figure 11(a) shows the evolution of the boundary-layer disturbance, when a continuous Orr-Sommerfeld mode is prescribed at the inflow plane of the computational domain. A transient region can be identified up to $x \simeq 1000$, whereas further downstream the evolution of the boundary-layer disturbance is fully determined by exponential growth of unsteady cross-flow instability. Hence, the swept-plate boundary layer supports receptivity for travelling cross-flow modes to free-stream vortices. From figure 10 it is clear that there is no location where the wavenumbers of free-stream disturbance and unstable eigenmode match. Wavenumber reduction from the forcing wavenumber α_{FS} to the eigenmode wavenumber α_{CF} through chordwise mean-flow variations is thus a requirement for the excitation of the observed cross-flow instability.

The upstream transient growth of the boundary-layer disturbance in figure 11(a) is mainly due to the forcing of Squire modes by the Orr-Sommerfeld free-stream mode, as also seen in Zaki & Durbin (2005). These are all stable but non-normal, thus giving rise to non-modal growth. Some transient behavior might also result from the fact that the free-stream modes are eigenmodes of the Orr-Sommerfeld/Squire operator, which might cause some initial adjustment to the non-parallel mean flow. We performed tests on domains with different length of the fringe region and height of the free stream. This had small effects

on the adjustment of the free-stream mode and we found that the growth of the unstable eigenmode was hardly affected.

The significance of the strongly non-parallel upstream region of the three-dimensional base flow for the receptivity due to free-stream vorticity becomes evident through figure 11(b). This plot shows the response of the parallel Falkner-Skan-Cooke boundary layer to forcing with a free-stream vortical mode at an unstable Reynolds number, and the result is obtained by means of DNS of the parallel mean flow. Clearly, no unstable cross-flow wave is excited, that is, removing the non-parallel nature of the base flow deactivates the unsteady receptivity mechanism seen in figure 11(a). This observation also confirms that the required length-scale conversion discussed in the previous sub-section is only supported in the spatially developing flow.

The receptivity mechanism for travelling cross-flow instability is quantified in terms of the receptivity coefficient $C_V = C_V(\beta, \omega; m, \phi_0)$,

$$C_V = \frac{A_R}{\varepsilon_v} \quad , \tag{28}$$

where A_R is the receptivity amplitude of the excited unsteady cross-flow wave, and ε_v is the maximum amplitude of the vortical free-stream mode, assumed to be small. Both amplitudes are taken at the inflow plane of the domain, where the free-stream mode is prescribed. They are measured in terms of the wall-normal maximum of $\sqrt{\overline{u^2}}$. Figure 12 shows the influence of (a) the wall-normal wavenumber, (b) the spanwise wavenumber and (c) the angular frequency of the Orr-Sommerfeld free-stream mode on the receptivity coefficient. The vortical disturbance is computed at $Re_{\delta*} = 220$. Figure 12(d) displays the dependence of C_V on the chordwise station, at which the vortical mode is introduced in the free stream. Figure 12(a) shows that receptivity is most efficient for free-stream modes with a large wall-normal length scale. The maximum in C_V is obtained at $\gamma = 0.063$. This corresponds to a normal scale of $\lambda_y = 30.44$ times the 99% boundary-layer thickness at the inflow plane. Large receptivity coefficients are also observed in the range of small values for λ_y, namely at $\gamma = 1.508$ ($\lambda_y = 1.27$ inlet 99%-thicknesses), where $C_V > 0.3$. In contrast, C_V drops down to almost zero for the intermediate scales. Comparison with figure 9(c) in section 4.1 suggests that the receptivity mechanism is most efficient for vortical free-stream modes of either low decay rate or large penetration depth. On the other hand typical energy spectra for turbulent fields reveal that turbulent kinetic energy is concentrated on the small wavenumbers. Hence, the deeply penetrating vortical modes of large γ might in practice be unimportant for the transition process, in spite of the rather large receptivity coefficients associated with them. In figure 12(b) an optimal spanwise wavenumber of $\beta = -0.14$ can be identified, at which C_V is maximum. Compare with steady receptivity to surface roughness, section 3.1, being most efficient at $\beta = -0.19$.

Figure 12(c) shows that the efficiency of the receptivity process increases when ω approaches zero. The figure is restricted to the negative ω half-plane, where the unstable cross-flow modes are found. Inspection of figure 9(b) reveals

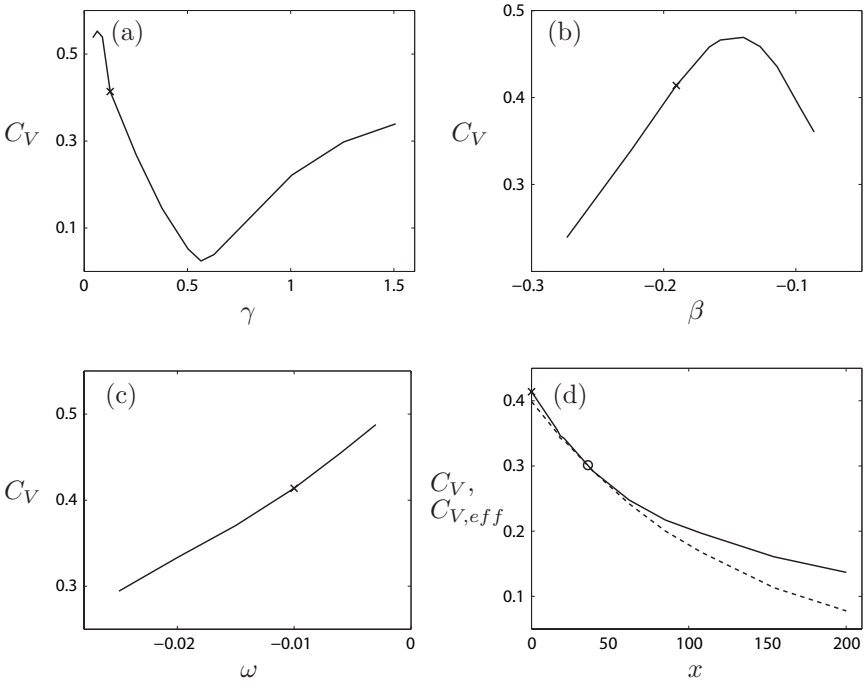

FIGURE 12. Dependence of the receptivity coefficient to free-stream vorticity on the wall-normal wavenumber (a), the spanwise wavenumber (b) and the angular frequency (c) of the vortical mode. In (d) the influence of the chordwise station on C_V is shown, at which the free-stream disturbance is prescribed (——). Effective receptivity coefficient (----). The circle shows the first neutral point of the excited unsteady cross-flow mode. The plots are based on $(Re_\delta, \omega; \beta, \gamma)$=(220,-0.01;-0.19,0.126), marked by the cross.

that the increase of C_V for $\omega \to 0$ can again be attributed to a large penetration depth. Also Jacobs & Durbin (1998) found maximum receptivity in Blasius flow for the deeply penetrating vortical modes of low frequency. Figure 12(d) displays the dependence of C_V on the chordwise station, where the free-stream mode is prescribed. This location is equivalent with the inflow plane. Hence, various domains with different inflow Reynolds numbers $Re_{\delta*,0}$ are used for this study, and the vortical mode is computed at the according inflow Reynolds number. The origin in the figure complies with $Re_{\delta*,0} = 220$. As in section 3.1, figure 6, it is again meaningful to consider the effective receptivity coefficient,

$$C_{V,eff} = \frac{C_V}{e^{N_R}} = C_V \frac{A_I}{A_R} = \frac{A_I}{\varepsilon_v} \quad , \tag{29}$$

to take the decay or growth of the cross-flow instability at the inflow plane into account. N_R is the N-factor of the unsteady cross-flow mode at the inlet and A_I is its amplitude at the first neutral point. Clearly, receptivity to free-stream vorticity is most efficient at $x = 0$ ($Re_{\delta*,0} = 220$) where the boundary layer is thin and highly non-parallel. The same result has been obtained in figure 6 for steady receptivity to surface roughness. It can be concluded that the scale-conversion process required for receptivity is most efficient in the rapidly evolving region near the leading edge. However, the curves in figure 12(d) suggest that even larger receptivity coefficients can be expected upstream of $Re_{\delta*,0} = 220$ in the immediate vicinity of the leading edge. These receptivity sites can, however, not be addressed by the present numerical method.

In summary, the unsteady receptivity mechanism due to vortical free-stream modes herein proposed has characteristics in common with both the localized and non-localized receptivity processes so far discussed in literature. On the one hand, the vortical disturbance resides in the entire free stream and acts non-locally on the boundary layer. In contrast to Blasius flow, on the other hand, where the excitation of streak-like disturbances inside the boundary layer is non-localized, the present mechanism for unsteady cross-flow modes in three-dimensional flow is efficient only near the leading edge. In this limited region, the basic flow is sufficiently non-parallel to provide the length scale of the cross-flow instability through scale conversion. This is a characteristic of localized receptivity.

5. Combination of roughness and free-stream vorticity

In the presence of both surface roughness and free-stream turbulence stationary and travelling cross-flow modes will coexist in three-dimensional boundary layers and compete with each other. This situation is modelled here by considering the combination of a spanwise periodic localized roughness element on the plate and a vortical Orr-Sommerfeld mode in the free-stream, both assumed to have small amplitudes. In section 3 and 4 it was demonstrated that there exists a direct receptivity mechanism to localized roughness and vortical free-stream disturbances, causing the occurrence of stationary and travelling cross-flow modes in the boundary layer. These mechanisms will still be present in the case of combined surface roughness and free-stream vorticity. Both the steady and the unsteady receptivity process may then give amplifying eigenmodes, which interact continuously and force a wavelike disturbance. This process builds thus on the combination of the two direct receptivity mechanisms discussed in the previous sections, followed by nonlinear interaction.

Next we examine whether there exists also a receptivity mechanism based on scattering of free-stream vorticity at the roughness in boundary layers of Falkner-Skan-Cooke type. For this purpose the mean flow is exposed to a vortical mode of spanwise wavenumber $\beta_V = -0.381$ together with a roughness element with $\beta_R = 0.190$. The response of the base flow is plotted in figure 13. While a stationary cross-flow mode evolves from the steady disturbance

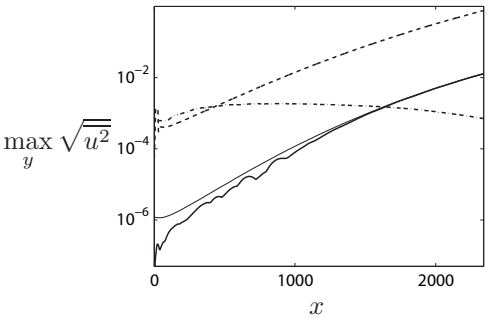

FIGURE 13. Combination of free-stream vorticity and surface roughness. The roughness element ($\beta_R = 0.190$) excites an unstable steady eigenmode (----), while the vortical free-stream mode ($\beta_V = -0.381$) does not trigger a growing travelling mode (-·-·-). In combination, however, they excite travelling cross-flow instability (——, thick curve).

field due to the roughness (dashed line), no unstable travelling cross-flow wave is excited by this particular free-stream mode (dashed-dotted line). Unsteady cross-flow instability is nevertheless observed in figure 13 (solid line), as deduced by comparing with the evolution curve for the travelling cross-flow wave at $\beta_{CF} = -0.190$ (thin solid line). The unsteady cross-flow mode is thus triggered by the interaction between the growing steady disturbance field caused by the roughness and the decaying unsteady perturbation due to the vortical free-stream disturbance. The spanwise wavenumber of the travelling eigenmode is given by $\beta_{CF} = \beta_V + \beta_R$, the frequency ω is provided by the free-stream disturbance and the chordwise wavenumber α_{CF} by the roughness contour. Hence, the roughness element is responsible for the scale-enhancement process. To conclude, a receptivity mechanism for travelling cross-flow instability has been identified, linearly depending on the amplitudes of both the free-stream vorticity and the surface roughness. It can be seen as the cross-flow counterpart of the classical mechanism for Tollmien-Schlichting instability in Blasius flow proposed by Goldstein (1985) and Ruban (1985), which builds on the scattering of acoustic free-stream disturbances at localized surface roughness.

5.1. *Receptivity coefficient*

The receptivity mechanism displayed in figure 13 and explained in the previous section results in the excitation of a travelling unstable eigenmode of the base flow. It can be quantified in terms of a receptivity coefficient,

$$C_{VR} = \frac{A_R}{\varepsilon_v \varepsilon_h H(\alpha_{CF})} \quad , \tag{30}$$

where A_R is the receptivity amplitude of the excited travelling cross-flow wave at the roughness station, and ε_v and ε_h are the amplitudes of the vortical

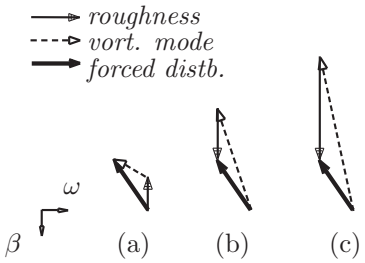

	(a)	(b)	(c)
ω	-0.01	-0.01	-0.01
β_V	-0.063	-0.381	-0.571
β_R	0.127	0.190	0.381
β_{CF}	-0.190	-0.190	-0.190
C_{VR}	0.109	0.067	0.013

FIGURE 14. Interaction between a decaying unsteady disturbance due to free-stream vorticity and an amplifying steady disturbance caused by localized roughness. Three combinations of the spanwise wavenumbers β_V and β_R of the vortical mode and the roughness element are considered. Excitation of an unstable travelling cross-flow mode with spanwise scale $\beta_{CF} = -0.190$.

free-stream disturbance and the roughness element. $H(\alpha_{CF})$ is the Fourier component of the roughness bump at the wavenumber of the steady disturbance. Definition (30) is in analogy with the efficiency coefficient for receptivity to free-stream sound in combination with roughness, as used e.g. by Crouch (1993) and Choudhari (1994) for Finite Reynolds-Number Theory calculations in Falkner-Skan-Cooke flow.

5.2. *Results*

The spanwise wavenumber β_{CF} of the travelling cross-flow wave excited via the combination of roughness and free-stream vorticity is obtained through the sum of the wavenumbers β_V and β_R of the interacting unsteady and steady disturbance,

$$\beta_{CF} = \pm\beta_V \pm \beta_R \ , \tag{31}$$

i.e. four different unsteady waves per (β_V, β_R) combination can be forced at second order. In principle an infinite number of such combinations may be considered. Here, ω, β_V and β_R are chosen to keep the frequency and spanwise scale of the generated mode constant and to examine the efficiency of the receptivity process when varying the spanwise scale of free-stream mode and roughness. In figure 14 three (β_V, β_R) combinations are reported, all summing to $\beta_{CF} = -0.190$. The specific summation of β and ω is highlighted by the arrow diagrams in figure 14. In the inserted table the receptivity coefficient C_{VR} is compiled. The largest coefficient is obtained in case (a), when the spanwise wavenumber of the free-stream mode is one third and that of the roughness element is two thirds of the instability wavenumber β_{CF}. For case (c) the receptivity process is one order-of-magnitude weaker, showing that the difference between the forcing wavenumbers, β_V and β_R, and the forced wavenumber β_{CF} should not be too large.

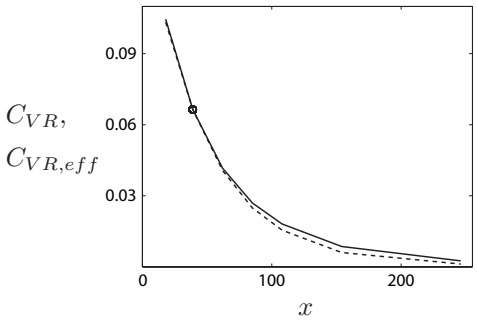

FIGURE 15. Coefficient for receptivity to free-stream vorticity combined with surface roughness versus chordwise location (—–) and effective receptivity coefficient (----). The spanwise wavenumbers of the vortical mode and the roughness element are $|\beta_V| = 0.381$ and $\beta_R = 0.190$ (case (b) in figure 14). Circle: First neutral point of the excited unsteady cross-flow wave.

In figure 15 the receptivity coefficient C_{VR} is plotted versus the chordwise station. Also the effective receptivity coefficient is shown again. Case (b) in figure 14 is considered here. Like the direct receptivity mechanisms for steady and unsteady cross-flow modes, the receptivity process due to combination of free-stream vorticity and roughness becomes most efficient in the region between the leading edge of the plate and the first neutral point of the excited travelling cross-flow wave.

It has been shown above that unstable travelling disturbances can occur, even if the unsteady forcing does not contain any unstable wavenumbers. Another scenario builds on coexisting unstable stationary and travelling cross-flow modes forcing an unsteady disturbance wave by interaction. This is then not a receptivity process on its own but a combination of the two direct receptivity mechanisms, followed by interaction between the triggered instability waves. Such a situation is displayed in figure 16, where the forced wave (solid line) has again a wavenumber of $\beta = -0.190$. The chordwise wavenumber $\mathrm{Re}\{\alpha\}$ and the growth rate $\mathrm{Im}\{\alpha\}$ of this wave are obtained as the sum of the chordwise wavenumbers and growth rates of the interacting cross-flow modes. This explains why the growth rate of the induced wave is larger than that of the unstable cross-flow mode with the same spanwise wavenumber and frequency, figure 13. Modes continuously forced by two unstable waves are therefore expected to have a large influence during the transition process. Both mechanisms, the excitation of unsteady cross-flow instability and the forcing of travelling waves by interacting cross-flow modes, need to be addressed in three-dimensional boundary layers.

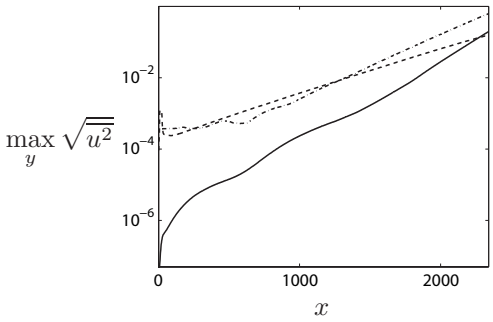

FIGURE 16. Combination of free-stream vorticity and surface roughness. Both the roughness element ($\beta_R = 0.095$, ----) and the vortical free-stream mode ($\beta_V = -0.095$, -·-·-) excite unstable cross-flow eigenmodes, which interact and force a harmonic wave with $\beta_f = -0.190$ (——).

6. Steady versus unsteady cross-flow instability

An important issue of receptivity and instability studies in three-dimensional boundary-layer flow is to determine whether stationary or travelling cross-flow vortices dominate the disturbance environment inside the boundary layer, see for example the review by Saric *et al.* (2003). In the sections 3 through 5 three receptivity mechanisms for steady and unsteady cross-flow instability have been investigated. Their efficiency has been quantified in terms of the receptivity coefficients C_R, C_V and C_{VR}, equations (20), (28) and (30), which can be used to assess the initial amplitude of the disturbance. In contrast to C_V, C_R and C_{VR} involve the spectral amplitude $H(\alpha)$ of the roughness shape. In order to compare the receptivity amplitudes A_R of the excited steady and unsteady cross-flow instabilities it is therefore convenient to re-formulate the receptivity coefficients of the three studied mechanisms in terms of a coefficient $\tilde{C}$,

$$\tilde{C}_R = \frac{A_R}{\varepsilon_h} = H(\alpha_{CF}) C_R \ , \tag{32a}$$

$$\tilde{C}_V = \frac{A_R}{\varepsilon_v} = C_V \ , \tag{32b}$$

$$\tilde{C}_{VR} = \frac{A_R}{\varepsilon_v \varepsilon_h} = H(\alpha_{CF}) C_{VR} \ . \tag{32c}$$

Table 3 compiles the three receptivity processes and the largest associated coefficients $\tilde{C}$. The maximum in $\tilde{C}_R$ is obtained for a roughness element of shape I and a spanwise wavenumber of $\beta_R = 0.157$. $\tilde{C}_V$ is largest for a free-stream mode of $\beta_V = -0.14$. The coefficient $\tilde{C}_{VR}$ for receptivity due to coupling at roughness is maximum, when a roughness element of $\beta_R = 0.127$ is combined with a free-stream mode of $\beta_V = -0.063$.

Whether steady or unsteady cross-flow instability is dominant at the receptivity site will depend on the relative amplitude of the wall roughness and the

TABLE 3. Receptivity mechanisms for steady and unsteady cross-flow ("CF") instability and their efficiency. Amplitude coefficients at the receptivity site ($\tilde{C}$) and at $x = 710$ ($\tilde{C}_{710}$).

Extern. perturb.	Recp. mech.	Excited disturb.	$\tilde{C}$	$\tilde{C}_{710}$
Roughess	direct	steady CF mode	0.221	2.27
Vort. mode	direct	unstd. CF mode	0.469	10.54
Vort. mode+rougn.	coupling	unstd. CF mode	1.784	44.22

vortical free-stream mode. In the following discussion, it is assumed that the amplitude of the roughness element is $\varepsilon_h = 0.025$, i.e. 2.5% of the boundary-layer displacement thickness at the inflow plane and about 2.4% of the local displacement thickness at the roughness station. This value corresponds approximatively to a roughness height of $k = 6\mu m$, as in the experiments by Reibert *et al.* (1996). Such a roughness bump will excite a steady cross-flow mode with an initial amplitude of $A_R = \varepsilon_h \tilde{C}_R = 5.53 \cdot 10^{-3}$. A travelling cross-flow wave of same amplitude is obtained via direct receptivity, if a free-stream vortex with amplitude $\varepsilon_v = A_R/\tilde{C}_V = 0.012$ acts on the boundary layer. To obtain $A_R = 5.53 \cdot 10^{-3}$ via the mechanism due to unsteady disturbance scattering at the roughness, a free-stream mode with amplitude $\varepsilon_v = A_R/(\varepsilon_h \tilde{C}_{VR}) = 0.124$ needs to interact with the roughness-induced steady disturbance. Two conclusions can be drawn: (1) Direct unsteady receptivity for travelling cross-flow instability is about ten times more efficient than unsteady receptivity to free-stream vorticity scattered at roughness of $\varepsilon_h = 0.025$ ($\simeq 6\mu m$) height. (2) Given $\varepsilon_h = 0.025$, stationary cross-flow modes will dominate at the receptivity site as long as the vortical free-stream disturbance has an amplitude lower than $\varepsilon_v = 1.2\%$ of the chordwise free-stream velocity.

The dominating cross-flow modes at the receptivity site are not necessarily the most dangerous instability waves further downstream. To estimate the relevant disturbances in the region of linear growth, the downstream amplitudes of the different instability waves have to be compared with each other, thus accounting for the initial amplification of the different unstable waves. Here, the comparison is performed at the position $x = 710$, which corresponds approximately to the second measurement station in the experiments by Reibert *et al.* (1996). Amplitude coefficients in analogy with equation (32) are used by replacing the receptivity amplitude A_R by the wave amplitude at $x = 710$, A_{710}. They are denoted $\tilde{C}_{710}$ and listed in the last column of table 3. Note that $\tilde{C}_{710}$ is largest for roughness of $\beta_R = 0.217$ and for free-stream vorticity of $\beta_V = -0.190$, i.e. other spanwise wavenumbers than those at the receptivity site are dominant at $x = 710$. The comparison of the downstream disturbance amplitudes leads to the following conclusions: (1) The stationary cross-flow mode caused by $6\mu m$ roughness amplifies to $A_{710} = \varepsilon_h \tilde{C}_{R,710} = 0.057$. Travelling cross-flow instability excited via the direct receptivity process reaches the same amplitude at $x = 710$, when free-stream

vorticity with $\varepsilon_v = A_{710}/\tilde{C}_{V,710} = 5.38 \cdot 10^{-3}$ acts on the boundary layer. (2) The receptivity process for free-stream vorticity combined with roughness requires a continuous-spectrum mode with $\varepsilon_v = A_{710}/(\varepsilon_h \tilde{C}_{VR,710}) = 5.13 \cdot 10^{-2}$ and can again not compete with the direct receptivity mechanism. Also continuous forcing of a non-modal wave by interacting cross-flow instability, briefly mentioned at the end of section 5, is not relevant at $x = 710$, since a free-stream vortex with $\varepsilon_v = 8.63\%$ would be needed to obtain $A_{710} = 0.057$.

For the roughness considered above the amplitude of the disturbance is still relatively low at $x = 710$, namely $\simeq 6\%$ of the free-stream velocity. Further downstream, the competition between the stationary and the travelling cross-flow modes can lead to different results, since unsteady cross-flow modes amplify at larger growth rates than steady cross-flow waves. Therefore, lower free-stream turbulence intensities than those estimated above can lead to a transition scenario dominated by travelling cross-flow modes. Also the wave forced by interaction between two unstable modes grows faster than the stationary cross-flow modes. To summarize, in the presence of micron-sized roughness steady cross-flow instability will dominate in the boundary-layer region up to $x = 710$, unless the free-stream disturbances have amplitudes of more than $\simeq 0.5\%$ of the free-stream velocity.

7. Conclusions

Receptivity of the three-dimensional boundary layer developing on a swept flat plate is investigated by Direct Numerical Simulation. The ability of wall roughness, free-stream vortical modes and their interaction to trigger steady and travelling cross-flow modes is shown. The base flow, solution to the Navier-Stokes equations with Falkner-Skan-Cooke profiles as initial condition, is chosen with a sweep angle of 45° and a Hartree parameter $\beta_H = 0.33$ defining the free-stream acceleration.

Receptivity of steady cross-flow vortices to localized spanwise periodic roughness elements is examined first. Our results reproduce the main features of previous studies in literature: Roughness forces directly the unstable steady eigenmodes inside the boundary layer, and receptivity increases when the surface roughness is located upstream of the neutral stability points. In this work, the focus is on the validity of the local approximation for non-parallel flows, which is based on the assumption that receptivity is proportional to the spectral content of the roughness shape at the chordwise instability wavenumber. This enables the definition of receptivity coefficients independent of the particular shape of the roughness element. The present results show that this approximation is valid as long as the chordwise extension of the roughness is smaller than the wavelength of the unstable mode. For less localized roughness, the receptivity process becomes dependent on the shape of the roughness element. However, a first order correction can be introduced as in Bertolotti (2000); this amounts to a second receptivity coefficient which multiplies the derivative of the spectral shape of the roughness $H'(\alpha)$. This contribution is almost zero

for very localized roughness elements, characterized by flat Fourier transforms with $H'(\alpha) \approx 0$, and significant for waves not represented by the roughness shape, $H(\alpha) \approx 0$, i.e. waves shorter than the characteristic chordwise length of the surface irregularity. However, we found that the correction after Bertolotti (2000) gives roughness-shape independent receptivity coefficients only within a limited range of chordwise bump lengths.

The influence of bump height on receptivity has been presented, as well. For the roughness elements under consideration it has been shown that nonlinear effects on receptivity come into play beyond a bump amplitude of about 5% of the displacement thickness, leading to slowly decreasing efficiency coefficients as the roughness height is increased. Nonlinearity has, however, a weaker effect on receptivity than on the subsequent growth of the unstable cross-flow mode.

Free-stream vortical modes impinging on a three-dimensional boundary layer are modelled by the continuous-spectrum eigenmodes of the linearized Orr-Sommerfeld/Squire operator. To the best of our knowledge, the modes pertaining to the three-dimensional base flow are examined for the first time in this work. The three-dimensional base flow is shown to cause a significantly larger damping of the continuous modes towards the wall, which are therefore confined outside the shear layer. Unlike in two-dimensional boundary layers, the most penetrating modes are found to be quasi two-dimensional waves, with very small values of the spanwise wavenumber. This can be explained by the fact that two-dimensional waves become insensitive to the spanwise (or cross-flow) velocity component. These modes are also associated to low values of the chordwise wavenumber and represent therefore large horizontal structures with scales much larger than those of the unstable waves.

The direct receptivity mechanism in the presence of free-stream modes is entirely due to the non-parallel nature of the base flow. This provides the streamwise variations necessary for the scale-conversion process, by which the unstable cross-flow modes are excited. Free-stream modes have also been used previously to investigate the receptivity of two-dimensional boundary-layer flows, where they are shown to trigger significant transient growth of low-frequency modes. However, this is not observed in the present case, which can be explained by the presence of strong inflectional instabilities in three-dimensional boundary layers and by the favorable pressure gradient, reducing transient effects.

The efficiency of receptivity to free-stream vorticity is measured in terms of a receptivity coefficient, defined by the ratio between the initial amplitude of the unstable travelling mode and the level of fluctuations in the free stream. The magnitude of the receptivity coefficient is determined by two competing effects. On the one hand, modes with fast variations in the wall-normal direction experience larger decay rate in the chordwise direction and are therefore less effective in forcing the boundary layer along significant chordwise distances. At the same time, though, these modes are less sheltered by the mean shear and have therefore larger support inside the boundary layer. The three-dimensional

base flow has been shown to be receptive to both deeply penetrating vortical modes with small wall-normal scale and slowly decaying modes with large normal length scale. The results also demonstrate that the scale conversion of the free-stream mode is more efficient at lower Reynolds numbers, i.e. where the streamwise variations of the base flow are more significant. This points to the need for correct modelling of leading-edge effects in order to capture the initial entrainment of the free-stream modes.

The coupling between steady perturbations excited by wall roughness and unsteady disturbances induced by free-stream vorticity is investigated, as well. The results indicate that the stationary and travelling modes can efficiently force a wave with the frequency of the external vortical disturbance and a spanwise wavenumber given by the sum of those of the generating modes. If the two interacting modes are both unstable, they continuously force an unsteady wave amplifying at a rate equal to the sum of the growth rates of the interacting parent modes. On the other hand, modal travelling cross-flow instability is observed when the vortical free-stream mode cannot directly trigger an unsteady growing disturbance, showing that also a receptivity mechanism related to the scattering of free-stream modes on the roughness surface is available. However, the receptivity coefficients related to this receptivity process are much smaller than for the mechanism in the absence of roughness. Travelling cross-flow instability is therefore triggered via direct receptivity to free-stream vorticity in low-noise environments.

The relative importance of the two direct receptivity mechanisms is estimated by considering a roughness height of the order of 2.5% of the boundary layer displacement thickness. It is found that steady cross-flow instability will dominate in the boundary layer, unless the free-stream disturbances have amplitudes of about $\simeq 0.5\%$ of the free-stream velocity. Note that the latter estimate can be considered conservative for the travelling modes since it is based only on the initial growth of the unstable waves.

The receptivity mechanisms due to coupling of free-stream modes at roughness presented in this work may become important at high levels of free-stream turbulence. In this case, one should also consider the nonlinear interaction among free-stream modes. This type of interaction is indeed found to be the dominant mechanism in the case of streaks forced in the Blasius boundary layer by free-stream turbulence intensities larger than 3.5% (see Brandt *et al.* 2004). In three-dimensional boundary layers, one can expect an even larger relevance of these nonlinear effects; in this case the interaction between two exponentially growing modes may continuously induce waves with large amplification and quickly create a disturbed boundary layer flow. To better analyze this scenario, full nonlinear simulations are the most suitable tool, and future work is planned in this direction.

This research is supported by VR (The Swedish Research Council). SNIC computing facilities located at the Center for Parallel Computers (PDC), KTH, have been used for parts of the computations.

References

Berlin, S. & Henningson, D. S. 1999 A nonlinear mechanism for receptivity of free-stream disturbances. *Phys. Fluids* **11**, 3749–3760.

Bertolotti, F. P. 1997 Response of the Blasius boundary layer to free-stream vorticity. *Phys. Fluids* **9**, 2286–2299.

Bertolotti, F. P. 2000 Receptivity of three-dimensional boundary-layers to localized wall roughness and suction. *Phys. Fluids* **12(7)**, 1799–1809.

Bertolotti, F. P. & Kendall, J.M. 1997 Response of the Blasius Boundary Layer to Controlled Free-Stream Vortices of Axial Form. *AIAA Paper* (97-2018).

Bippes, H. & Deyhle, H. 1992 Das Receptivity-Problem in Grenzschichten mit längswirbelartigen Störungen. *Zeitschrift f. Flugwiss. Weltraumforschung* **16**, 34–41.

Brandt, L., Henningson, D. S. & Ponziani, D. 2002 Weakly non-linear analysis of boundary layer receptivity to free-stream disturbances. *Phys. Fluids* **14**, 1426–1441.

Brandt, L., Schlatter, P. & Henningson, D. S. 2004 Transition in boundary layers subject to free-stream turbulence. *J. Fluid Mech.* **517**, 167–198.

Buter, T. A. & Reed, H. L. 1994 Boundary layer receptivity to free-stream vorticity. *Phys. Fluids* **6 (10)**, 3368–3379.

Chevalier, M., Schlatter, P., Lundbladh, A. & Henningson, D. S. 2007 A Pseudo-Spectral Solver for Incompressible Boundary Layer Flows. *Tech. Rep.* TRITA-MEK 2007:07. Royal Institute of Technology (KTH), Dept. of Mechanics, Stockholm.

Choudhari, M. 1994 Roughness-induced Generation of Crossflow Vortices in Three-Dimensional Boundary Layers. *Theoret. Comput. Fluid Dynamics 6* pp. 1–30.

Choudhari, M. & Streett, C. L. 1992 A finite Reynolds number approach for the prediction of boundary layer receptivity in localized regions. *Phys. Fluids A* **4**.

Collis, S. S. & Lele, S. K. 1999 Receptivity to surface roughness near a swept leading edge. *J. Fluid Mech.* **380**, 141–168.

Crouch, J. D. 1992 Localized receptivity of boundary layers. *Phys. Fluids A* **4 (7)**, 1408–1414.

Crouch, J. D. 1993 Receptivity of three-dimensional boundary layers. *AIAA Paper* (93-0074).

Crouch, J. D. & Spalart, P. R. 1995 A study of non-parallel and nonlinear effects on the localized receptivity of boundary layers. *J. Fluid Mech.* **290**, 29–37.

Fransson, J. H. M., Matsubara, M. & Alfredsson, P. H. 2005 Transition induced by free-stream turbulence. *J. Fluid Mech.* **527**, 1–25.

Goldstein, M. E. 1983 The Evolution of Tollmien-Schlichting Waves Near a Leading Edge. *J. Fluid Mech.* **127**, 59–81.

Goldstein, M. E. 1985 Scattering of Acoustic Waves into Tollmien-Schlichting Waves by Small Streamwise Variations in Surface Geometry. *J. Fluid Mech.* **154**, 509–529.

Grosch, C. E. & Salwen, H. 1978 The continuous spectrum of the Orr-Sommerfeld equation. Part 1. The spectrum and the eigenfunctions. *J. Fluid Mech.* **87**, 33–54.

Högberg, M. & Henningson, D. S. 1998 Secondary instability of cross-flow vortices in Falkner-Skan-Cooke boundary layers. *J. Fluid Mech.* **368**, 339–357.

Jacobs, R. G. & Durbin, P. A. 1998 Shear sheltering and continuous spectrum of the Orr-Sommerfeld equation. *Phys. Fluids* **10(8)**, 2006–2011.

Jacobs, R. G. & Durbin, P. A. 2001 Simulations of bypass transition. *J. Fluid Mech.* **428**, 185–212.

Kendall, J.M. 1998 Experiments on boundary-layer receptivity to freestream turbulence. *AIAA Paper 98-0530* .

Lin, N., Reed, H. & Saric, W. 1992 Effect of leading edge geometry on boundary-layer receptivity to freestream sound. In *Instability, Transition and Turbulence* (ed. M. Hussaini, A. Kumar & C. Streett). Springer.

Malik, M. R., Zang, T. A. & Hussaini, M. Y. 1985 A spectral collocation method for the Navier-Stokes equations. *J. Comp. Phys.* **61**, 64–88.

Maslowe, S. A. & Spiteri, R. J. 2001 The continuous spectrum for a boundary layer in a streamwise pressure gradient. *Phys. Fluids* **13(5)**, 1294–1299.

Ng, L. L. & Crouch, J. D. 1999 Roughness-induced receptivity to crossflow vortices on a swept wing. *Phys. Fluids* **11(2)**, 432–438.

Nordström, J., Nordin, N. & Henningson, D. S. 1999 The fringe region technique and the Fourier method used in the direct numerical simulation of spatially evolving viscous flows. *SIAM J. Sci. Comp.* **20**, 1365–1393.

Reibert, M. S., Saric, W. S., Carillo, R. B. & Chapman, K. L. 1996 Experiments in nonlinear saturation of stationary crossflow vortices in a swept-wing boundary layer. *AIAA Paper* (96-0184).

Ruban, A. I. 1985 On the Generation of Tollmien-Schlichting Waves by Sound. *Fluid Dynamics* **19**, 709–716.

Saric, W. S., Reed, H. L. & Kerschen, E. J. 2002 Boundary-Layer Receptivity to Freestream Disturbances. *Annu. Rev. Fluid Mech.* **34**, 291–319.

Saric, W. S., Reed, H. L. & White, E. B. 2003 Stability and Transition of Three-Dimensional Boundary Layers. *Annu. Rev. Fluid Mech.* **35**, 413–440.

Schlichting, H. 1979 *Boundary-Layer Theory*, seventh edn. McGraw-Hill.

Schmid, P. J. & Henningson, D. S. 2001 *Stability and Transition in Shear Flows*. Springer.

Zaki, T. A. & Durbin, P. A. 2005 Mode interaction and the bypass route to transition. *J. Fluid Mech.* **531**, 85–111.

Zaki, T. A. & Durbin, P. A. 2006 Continuous mode transition and the effects of pressure gradient. *J. Fluid Mech.* **563**, 357–388.

Zavol'skii, N. A., Reutov, V. P. & Ryboushkina, G. V. 1983 Generation of Tollmien-Schlichting Waves via Scattering of Acoustic and Vortex Perturbations in Boundary Layer on Wavy Surface. *J. Appl. Mech. Tech. Phys.* pp. 79–86.

2

Paper 2

Transition to turbulence in the boundary layer over a smooth and rough swept plate exposed to free-stream turbulence

By Lars-Uve Schrader, Subir Amin & Luca Brandt

Linné Flow Centre, Department of Mechanics
Royal Institute of Technology, SE-100 44 Stockholm, Sweden

Internal report

Receptivity, disturbance growth and transition to turbulence of the three-dimensional boundary layer developing on a swept flat plate are studied for both smooth and rough walls by means of numerical simulations. The flow under investigation is subject to a favorable pressure gradient and represents therefore a model for swept-wing flow downstream of the leading edge and upstream of the pressure minimum of the wing. The boundary layer is perturbed through two different disturbance sources: free-stream turbulence and localized surface roughness with random distribution in the spanwise direction. The intensity of the turbulent free-stream fluctuations ranges from conditions typical for free flight to the high levels usually encountered in turbo-machinery applications. The free-stream turbulence excites initially non-modal streak-like disturbances as in two-dimensional boundary layers, soon evolving into modal instabilities in the form of unsteady cross-flow modes. The latter grow faster and dominate the downstream disturbance environment inside the boundary layer. Hence, the laminar-turbulent transition of the studied flow does not follow the bypass route. The results show that the receptivity mechanism is linear for the disturbance amplitudes under consideration, while the subsequent growth of the primary disturbances rapidly becomes affected by nonlinear saturation in particular for free-stream fluctuations with high intensity. The flow is also receptive to the localized roughness strip, and the boundary-layer response is characterized by stationary cross-flow modes. The mode with most efficient receptivity dominates the disturbance environment inside the boundary layer, and the disturbance environment in the layer is less complex than in the case of free-stream turbulence. When both free-stream fluctuations and wall roughness act at the same time on the boundary layer, the transition is dominated by steady cross-flow waves unless the incoming turbulence intensity is larger than about 0.5%. Transition to turbulence occurs in the form of localized turbulent spots appearing randomly in the flow. For the case of travelling cross-flow modes induced by free-stream turbulence, the flow structures at the breakdown are analyzed.

1. Introduction

Receptivity, disturbance growth and breakdown – these are the fundamental stages through which a laminar flow becomes turbulent. Numerous issues are involved in the transition process, e.g. how external perturbations enter the boundary layer and excite internal disturbances (receptivity), how the latter grow (instability), and when and where the flow first becomes turbulent (breakdown). The relevance of these issues is closely related to the ability of predicting the flow and thus to applications, where for instance drag reduction on aircraft wings by suppression or downstream delay of transition is of interest (flow control). Such measures require a clear understanding of how the flow becomes turbulent.

1.1. *Transition in two-dimensional boundary layers*

Transition originating from exponentially growing eigenmodes of the two-dimensional base flow known as Tollmien-Schlichting (TS) waves is called *natural transition* and is observed in flow with low background disturbance levels. When these primary waves grow above a threshold amplitude, the flow becomes susceptible to secondary instability which is three-dimensional in nature and characterized by the occurrence of the so called lambda vortices. Depending on the intensity of the external disturbance environment two kinds of secondary instability with different frequency, called H- and K-type have been observed before the flow becomes fully turbulent. A review of natural transition can be found in Herbert (1988) and Kachanov (1994).

Several experiments, see e.g. Taylor (1939), Klebanoff (1971), Kendall (1985), Westin *et al.* (1994) and Fransson *et al.* (2005), reveal however that transition in boundary-layer flows exposed to free-stream turbulence of high intensity does not origin from exponentially growing TS-waves, but rather from the growth of perturbations elongated in the streamwise direction: Natural transition is 'bypassed'. Ellingsen & Palm (1975) have demonstrated that initial disturbances can amplify linearly with time in inviscid shear layers, producing a streaky pattern of alternating high and low velocity. This kind of amplification has been termed 'transient growth' in Hultgren & Gustavsson (1981) and shown to exist also in viscous flow. Landahl (1980) proposes a physical explanation, which builds on the wall-normal displacement of fluid particles in shear flows by weak pairs of counter-rotating streamwise vortices causing streamwise velocity perturbations. This so-called lift-up mechanism is effective in forcing streamwise oriented streaks of high and low streamwise velocity alternating in the spanwise direction. The mathematical framework for transient growth is compiled in Schmid & Henningson (2001) and is based on the non-normality of the linear Navier-Stokes operator in shear flows. Transient amplification is not described by a single growing eigenmode but by a sum of eigenmodes of Orr-Sommerfeld and Squire type (non-modal growth). This results in a boundary-layer disturbance changing its shape as individual modes grow or decay in time and space at different rates. Transient growth

may for this reason occur before the subsequent exponential behavior, and it is the underlying mechanism of *bypass transition*.

Bypass transition is observed in the presence of free-stream turbulence. While most components of the turbulent fluctuations are highly damped inside the boundary layer, the low-frequency oscillations can enter it and form long streaky structures. Besides the wind-tunnel experiments mentioned above, this transition scenario has also been investigated in numerical studies (Jacobs & Durbin 2001; Brandt *et al.* 2004) where the breakdown to turbulence could be analyzed in detail. As the streaks grow downstream, they become susceptive to high-frequency secondary instability triggered by the free-stream turbulence (Zaki & Durbin 2005; Hœpffner & Brandt 2008) or by streak interactions (Brandt & de Lange 2008), and breakdown to turbulent spots is initiated. These spots appear at random locations, grow in size and number and merge with each other, until the flow is completely turbulent.

1.2. *Transition in three-dimensional boundary layers*

Boundary layers on swept wings, plates and wedges, on cones or on rotating disks are three-dimensional, and the transition mechanisms differ from those in two-dimensional flows owing to the existence of different instability types. Saric *et al.* (2003) list four kinds of instability being active in different regions of the boundary layer: attachment-line, Görtler, streamwise (TS-waves) and cross-flow instability. The focus is here on the latter instability type since the basic flow under consideration is accelerated swept-plate flow. Cross-flow instability is related to the inflectional velocity profile of the cross component of the mean flow. The base flow is therefore characterized by strong inviscid instability, unlike two-dimensional boundary layers, and the cross-flow modes can also be stationary (see also the review article by Bippes 1999). Instabilities typical for two-dimensional boundary layers are usually most relevant in decelerating flows, for instance in the rear portion of a wing, whereas cross-flow instability is intensified in the forward part by the favorable pressure gradient downstream of the leading edge. At the same time, the favorable pressure gradient in this region suppresses the growth of TS-waves, and cross-flow instability becomes therefore the dominant transition mechanism for this type of flows. Whether steady or unsteady cross-flow waves lead to transition is a frequently addressed issue in the context of swept flows, the relevance of which is also connected to the need of correlating wind-tunnel experiments to free-flight tests with significantly lower levels of external vortical disturbances. Experiments by Deyhle & Bippes (1996) and White *et al.* (2001) and numerical studies by e.g. Crouch (1993), Choudhari (1994) and Schrader *et al.* (2008) suggest that steady cross-flow modes induced by wall roughness dominate in an environment of low-amplitude free-stream disturbances (at free-flight conditions), whereas travelling modes become dominant at higher intensities of the background disturbance (e.g. in turbo-machines or some wind-tunnel tests).

As the cross-flow waves grow downstream in amplitude they distort the chordwise mean-velocity profiles in spanwise direction. This causes doubly inflected profiles being inviscidly unstable and susceptive to high-frequency secondary instability. Results on secondary instability building on the Parabolized Stability Equations (PSE) are available in Malik *et al.* (1994) for swept Hiemenz flow and Malik *et al.* (1999) and Haynes & Reed (2000) for the swept-wing configuration, and findings from Direct Numerical Simulation (DNS) are presented in Wintergerste & Kleiser (1996, 1997) using the temporal framework and in Högberg & Henningson (1998) and Wassermann & Kloker (2002, 2003) for the spatial perspective.

The purpose of the present work is to study the receptivity and growth of cross-flow instability and non-modal streaky disturbances in swept-plate flow under free-stream turbulence, surface roughness and a combination of both. Simulations of the flow over a swept plate exposed to free-stream turbulence are presented here for the first time. In a previous investigation, Schrader *et al.* (2008) analyzed the receptivity mechanisms for three-dimensional swept boundary layers. The aim of that study was to isolate the effect of different components of a realistic disturbance source. Free-stream perturbations were modelled by single free-stream (Orr-Sommerfeld) modes. That study demonstrated that travelling cross-flow modes can be forced directly by vortical disturbances in the free stream via a scale-conversion process. In addition, the scattering of free-stream modes on chordwise localized surface roughness with spanwise periodicity was examined. The results in Schrader *et al.* (2008) show that the receptivity mechanism based on the coupling of free-stream modes at roughness may become important only for high levels of free-stream turbulence. However, in three-dimensional boundary layers, one can expect that the interaction between two exponentially growing modes may continuously induce waves with large amplification and quickly create a disturbed boundary-layer flow. To better analyze this scenario, full nonlinear simulations are therefore the most suitable tool, and they are presented here. We employ more complex models for the disturbance sources by considering a superposition of a large number of Orr-Sommerfeld/Squire modes with random phases and a turbulent energy spectrum to represent free-stream turbulence as well as localized roughness with spanwise random amplitude. These more realistic disturbances will bring nonlinear effects into play, and a comparison with the results in Schrader *et al.* (2008) will enable us to identify the impact of nonlinearity on receptivity to free-stream turbulence and roughness.

Besides the receptivity and the disturbance growth, also the breakdown of the three-dimensional boundary layer is herein investigated. The first part of the results is meant to illustrate the disturbance structures inside the boundary layer during growth, saturation and breakdown of the primary instabilities. In the second part, the focus is on the early receptivity process, where the receptivity coefficients for unsteady and steady cross-flow instability are compared with those in Schrader *et al.* (2008).

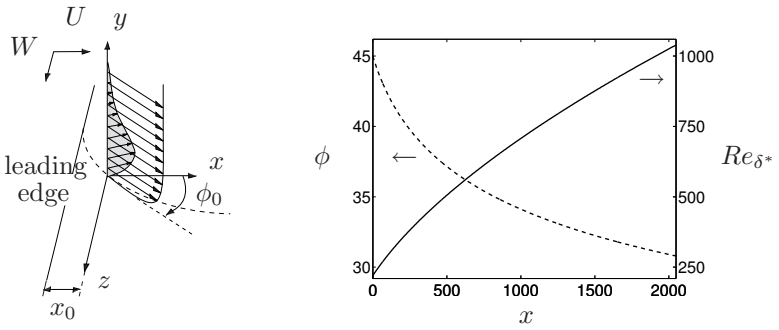

FIGURE 1. (a) Wall-normal profiles of the streamwise and the cross-flow velocity for Falkner-Skan-Cooke boundary-layer flow. (b) Reynolds number (——) and external streamline angle (----) as a function of the chordwise coordinate.

2. Flow configuration and numerical approach

2.1. *Base flow*

Boundary-layer flow over a swept flat plate is herein considered. The mean flow is obtained by solving the Navier-Stokes equations with the Falkner-Skan-Cooke velocity profiles as initial condition. This configuration often serves as a prototype for swept-wing boundary-layer flow, including many of its characteristics as the chordwise pressure gradient, the streamline curvature and the cross flow, while the leading edge and the surface curvature are not taken into account. The chordwise pressure gradient is quantified by the Hartree parameter β_H, which is chosen to be $\beta_H = 0.333$. This defines a favorable pressure-gradient boundary layer with chordwise flow acceleration,

$$U^*_\infty(x^*) = U^*_{\infty,0}\left(\frac{x^* + x^*_0}{x^*_0}\right)^{\frac{\beta_H}{2-\beta_H}} \quad \text{and} \quad W^*_\infty = U^*_{\infty,0}\tan\phi_0 \ , \qquad (1)$$

where U and W indicate the chord- and spanwise mean velocity and the star denotes dimensional quantities. The sweep angle ϕ_0 is defined at a reference station x^*_0, which corresponds to the inflow plane of the computational domain. The sweep together with the chordwise flow acceleration causes curved streamlines and a force imbalance inside the boundary layer driving a secondary mean-flow component in the cross-stream direction, the cross flow. The stream- and cross-wise velocity profiles of a swept boundary-layer flow are depicted in figure 1(a), where the coordinate system adopted is also shown. Due to its inflection point, the cross-flow profile supports inviscid instability modes, denoted also *cross-flow modes*. Note that instability waves propagating in the cross-stream direction have negative spanwise wavenumber β and positive chordwise wavenumber α in the chosen coordinate system.

The Falkner-Skan-Cooke boundary layer is homogeneous in the spanwise direction z^*. This, together with the free-stream velocity distribution in equation (1), enables the introduction of a similarity variable $\eta = \eta(x^*, y^*)$ and the derivation of ordinary differential equations for the functions $f(\eta)$ and $g(\eta)$. The mean-flow profiles U^* and W^*, defined as $f'(\eta)$ and $g(\eta)$, exhibit therefore a self-similar behavior. They are referred to as Falkner-Skan-Cooke velocity profiles, and further details on their derivation can be found in Högberg & Henningson (1998) and Schrader *et al.* (2008).

In the continuation, non-dimensional variables will be used, where lengths are normalized by the chordwise boundary-layer displacement thickness $\delta_0^* \equiv \delta^*(x_0^*)$ at the reference location x_0^* and velocities by the chordwise free-stream velocity $U_{\infty,0}^* \equiv U_\infty^*(x_0^*)$. Reference length and velocity define the Reynolds number at the computational inlet,

$$Re_{\delta_0^*} = \frac{U_{\infty,0}^* \delta_0^*}{\nu^*} \quad , \tag{2}$$

where ν^* is the kinematic viscosity. The local Reynolds number Re_{δ^*} is obtained by replacing δ_0^* and $U_{\infty,0}^*$ in (2) by their local values $\delta^*(x)$ and $U_\infty^*(x)$. Figure 1(b) shows the Reynolds number Re_{δ^*} and the local angle ϕ of the external streamline versus the chordwise coordinate x. The inflow Reynolds number is fixed at $Re_{\delta_0^*} = 220$, which translates into a reference station of $x_0 = 167\delta_0^*$ downstream of the virtual boundary-layer origin. Also the Reynolds number Re_x based on the chordwise location will occasionally be used; it is related to $Re_{\delta_0^*}$ via

$$Re_x = [x_0 + xU_\infty(x)]Re_{\delta_0^*} \quad . \tag{3}$$

The plate sweep angle is $\phi_0 = 45°$: The chord- and spanwise free-stream velocities are equal at x_0, and their normalized value is $U_\infty(x_0) = W_\infty(x_0) = 1$. The sweep angle under investigation is characterized by a significant cross-flow component and thus by a strong cross-flow instability. The basic flow is completely described by $Re_{\delta_0^*}$, β_H and ϕ_0, which are chosen to correspond to the values used in Schrader *et al.* (2008). This set of parameters defines conditions similar to those of the airfoil experiments at Arizona State University reported in Reibert *et al.* (1996).

2.2. *Numerical method*

The present results are obtained using a spectral method to solve the three-dimensional time-dependent incompressible Navier-Stokes equations, see Chevalier *et al.* (2007). The simulation code builds on a Fourier representation along the chord- and spanwise coordinates x and z and on Chebyshev polynomials in wall-normal direction y, along with a pseudo-spectral treatment of the nonlinear terms. Time advancement is based on a four-step third-order Runge-Kutta method for the nonlinear terms and a second-order Crank-Nicholson scheme for the linear terms. Aliasing errors from the computation of the nonlinear terms are removed in wall-parallel planes by the $\frac{3}{2}$-rule, while grid refinement in normal direction has turned out to be more convenient than dealiasing.

Along the wall a zero-slip condition is imposed for the mean velocity and disturbance, while von-Neumann conditions are employed at the far-field boundary above the plate. The choice of a periodic condition at the spanwise boundaries of the computational domain follows from the independence of the mean flow from the spanwise coordinate z and the assumption of a spanwise periodic perturbation velocity field. The swept-plate boundary layer develops along the chordwise direction: the boundary layer grows and the streamlines change continuously direction. To obtain nonetheless the chordwise periodicity required by a Fourier representation, a "fringe region" is used at the downstream end of the computational domain, as described by Nordström *et al.* (1999). In this region the velocity field $\vec{\mathcal{U}}$ is forced to the desired inflow velocity profiles $\vec{\mathcal{U}}_0$; they consist of the Falkner-Skan-Cooke similarity profiles in the present case with/without incoming disturbances, i.e. free-stream turbulence. The forcing is accomplished by an extra term in the Navier-Stokes equations, and the equation solved reads,

$$\frac{\partial \vec{\mathcal{U}}}{\partial t} = \mathcal{NS}(\vec{\mathcal{U}}) + \lambda(x)(\vec{\mathcal{U}}_0 - \vec{\mathcal{U}}) \ , \tag{4}$$

where $\mathcal{NS}$ indicates the right-hand side of the momentum equations, and $\lambda(x)$ is a smooth forcing function active only in the fringe region. $\vec{\mathcal{U}}$ denotes the instantaneous velocity field; note that $\vec{U}$ will be used to indicate the reference base flow.

2.3. *Sub-grid scale modelling*

The present study requires a computational domain of rather large spanwise and wall-normal size to accommodate a free-stream turbulence field with a wide enough range of length scales. The resolution of all scales would, however, result in prohibitively large computational costs such that the simulations are only affordable by employing a Large-Eddy Simulation (LES) model. The ADM-RT subgrid-scale model by Schlatter *et al.* (2006) is used for the present simulations, building on the Approximate Deconvolution Model (ADM) by Stolz & Adams (1999). This model has been successfully applied in incompressible transitional and turbulent flow (see, among others, the recent work by Monokrousos *et al.* 2008). LES relies on spatial filtering of the flow field and on the solution for filtered velocities, as indicated with the bar in the equations of momentum and mass conservation,

$$\frac{\partial \bar{u}_i}{\partial t} + \frac{\partial \bar{u}_i \bar{u}_j}{\partial x_j} = -\frac{\partial \bar{p}}{\partial x_i} + \frac{1}{Re}\frac{\partial^2 \bar{u}_i}{\partial x_j \partial x_j} - \frac{\partial \tau_{ij}}{\partial x_j} \ , \tag{5a}$$

$$\frac{\partial \bar{u}_i}{\partial x_i} = 0 \ . \tag{5b}$$

The spatial filtering is implicit through the reduced resolution of the LES grid here. The main ingredient of the ADM-RT model is the so-called relaxation

term (RT) used as a closure for the subgrid-scale stresses τ_{ij},

$$\frac{\partial \tau_{ij}}{\partial x_j} = \chi H_N * \bar{u}_i \quad \text{with} \quad H_N = (I - G)^{N+1} \ . \tag{6}$$

H_N denotes a three-dimensional high-pass filter of high order derived from the low-order low-pass filter G in Stolz *et al.* (2001), and the star stands for convolution in physical space. Here, H_N is characterized by the exponent $N = 5$ and the cut-off wavenumber $\kappa_c = 2\pi/3$ of the filter G. Numerical stability is ensured by a model coefficient χ in the range $0 \leq \chi \leq 1/\Delta t$. Here we chose $\chi = 0.2$, as in Schlatter *et al.* (2006, 2007); Monokrousos *et al.* (2008). The role of the RT term in (8) is to drain kinetic energy from the resolved fluctuations at the smallest represented length scale and thereby to model the impact of the unresolved motion on the resolved structures. In contrast to the classical Smagorinsky model the term χH_N of the ADM-RT model acts directly on the filtered velocities and not indirectly via the eddy viscosity and the mean strain rate. Further details can be found in the references mentioned above. Note that all the simulations were performed adding the sub-grid scale stresses. However, the computations focusing on the boundary-layer receptivity consider only the initial phase of the disturbance growth. In these cases, the extra relaxation term is practically zero and the computations can be considered as direct numerical simulations.

2.4. *Disturbance generation*

As in Schrader *et al.* (2008), two different disturbance sources are considered, a vortical perturbation in the free stream and a roughness element on the wall near the inflow plane of the computational domain. These two types of disturbances have been shown to be the most relevant in swept boundary layers in several studies. However, while the disturbances in Schrader *et al.* (2008) consist of one single spanwise wavenumber to isolate the wavenumber dependence of the receptivity, a more realistic disturbance environment is studied here. The free-stream perturbation is composed of a large number of vortical modes with random phase angles to obtain an adequate model for free-stream turbulence, while the surface roughness exhibits a random shape in spanwise direction. Care has been taken to include the modes with spanwise wavenumber at or near the wavenumbers of maximum growth and of largest receptivity as identified in Schrader *et al.* (2008). The free-stream turbulence at the inflow plane and the roughness element are shown in figure 2(a) and (b), and their numerical generation is described below.

2.4.1. *Free-stream turbulence*

The turbulent inflow disturbances are numerically generated in the same way as in Jacobs & Durbin (2001) and Brandt *et al.* (2004), i.e. by the superposition of eigenmodes from the continuous spectrum of the Orr-Sommerfeld and Squire operator – however, modified here for the Falkner-Skan-Cooke base

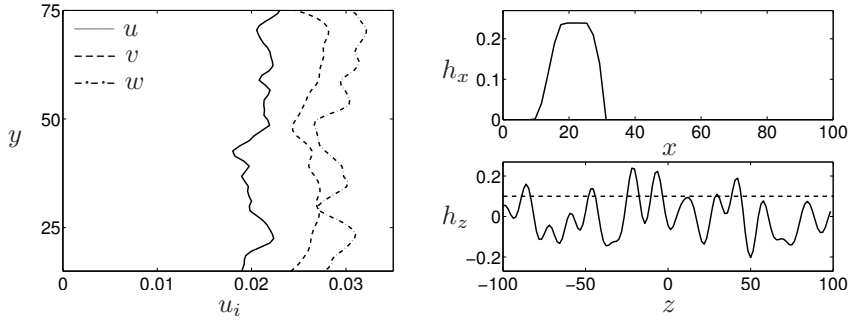

FIGURE 2. (a) Turbulent free-stream fluctuations at the inflow plane of the computational domain for a turbulence intensity of 2.53% of $U_{\infty,0}$. (b) Chord- and spanwise contour of the wall roughness. The root-mean-square amplitude is 0.1 (----).

flow. In contrast to the Fourier modes, these waves accommodate the presence of the plate and the boundary layer in that they are oscillatory only in the free stream while damped toward the wall; they are therefore often labelled *free-stream modes*. A wave vector $\vec{\kappa} = (\mathrm{Re}\{\alpha\}, \gamma, \beta)^T$ is associated to each free-stream mode, where the complex chordwise wavenumber α is the eigenvalue of the corresponding Orr-Sommerfeld and Squire problem and the wall-normal wave-number γ determines the position along the continuous spectrum (see e.g. Schmid & Henningson 2001). After choosing spanwise and wall-normal wavenumber β and γ and angular frequency ω, the eigenvalue α of the continuous-spectrum modes can be easily obtained from analytical expressions, as the set of Orr-Sommerfeld and Squire equation simplifies to a system of ordinary differential equations in the free stream. The velocity profiles pertaining to each eigenfunction can be computed numerically whereas the free-stream behavior can also be obtained analytically. The derivation of the dispersion relation and the details on the computation of the eigensolutions in Falkner-Skan Cooke flow are presented in Schrader *et al.* (2008), and the dispersion relation, repeated here, reads

$$\alpha = \frac{i}{2}[\sqrt{(Re_{\delta^*}U_\infty)^2 + 4(iRe_{\delta^*}(\beta W_\infty - \omega) + \beta^2 + \gamma^2)} - Re_{\delta^*}U_\infty] \ . \qquad (7)$$

An isotropic perturbation field is obtained in Fourier space by considering 20 concentric spherical shells of radius κ spanning the range of wave vectors of length $\kappa_l \leq \kappa \leq \kappa_u$. The limits κ_l and κ_u depend on the size and resolution of the computational domain and are chosen to be $\kappa_l = 0.05$ and $\kappa_u = 1.1$. Forty points are distributed with constant spacing on each shell: These define the wave vectors and continuous-spectrum eigenmodes to be included in the expansion for the free-stream disturbance,

$$\vec{u}_{FST} = \sum_{k=1}^{20} a_k \sum_{l=1}^{40} \hat{\vec{u}}_{kl}(y;\gamma) e^{i(\alpha_{kl}x + \beta_{kl}z - \omega_{kl}t)}. \qquad (8)$$

In the expression above, $\hat{\vec{u}}_{kl}$ denotes the wall-normal disturbance-velocity profiles of the free-stream mode and contains the wall-normal oscillations. The randomness inherent in turbulent fields is obtained through a random rotation of the shells, provided by random phase angles of the complex coefficients a_k in (8) as well as by the random phase in the complex function $\hat{\vec{u}}_{kl}$ (see Brandt *et al.* 2004). The amplitude of a_k is defined according to

$$|a_k| = |a(\kappa_k)| = \sqrt{\frac{1}{40} E(\kappa_k)(\kappa_{k+1} - \kappa_k)} \ , \tag{9}$$

i.e. the energy density pertaining to the wavenumber κ_k of the k-th shell is equally distributed among all modes in the shell. The energy distribution is approximated by the von-Kármán spectrum

$$E(\kappa) = \frac{2}{3} L \, Tu_0 \frac{a(\kappa L)^4}{[b + (\kappa L)^2]^{\frac{17}{6}}} \qquad \text{with} \qquad a = 1.606, \quad b = 1.350 \ . \tag{10}$$

$L \approx 1.56 L_{11}$ is a characteristic large length scale of the fluctuating field with L_{11} being the longitudinal length scale derived from the two-point velocity correlations. The turbulence intensity Tu is the relevant measure for the disturbance amplitude, defined as

$$Tu = \sqrt{\frac{1}{3}(\overline{u^2} + \overline{v^2} + \overline{w^2})} \ . \tag{11}$$

The vortical free-stream perturbation generated in this fashion is inserted in the fringe region of the computational domain, from where it is recycled to the inflow plane. The wall-normal distribution of the free-stream fluctuations at the inlet are depicted in figure 2(a).

2.4.2. *Surface roughness*

The surface roughness is modelled in a similar way as in Schrader *et al.* (2008), that is, through non-homogeneous boundary conditions for the disturbance velocities u, v and w at the wall,

$$\begin{pmatrix} u \\ v \\ w \end{pmatrix}_{wall} = \begin{cases} \begin{pmatrix} -h(x,z)\frac{\partial U}{\partial y} \\ 0 \\ -h(x,z)\frac{\partial W}{\partial y} \end{pmatrix}_{wall} , & h_{start} \le x \le h_{end} \\ \vec{0} \ , & \text{elsewhere} \ . \end{cases} \tag{12}$$

In the expression above, $h(x,z)$ is the shape of the roughness bump,

$$h(x,z) = \varepsilon_h h_x(x) h_z(z) \ , \tag{13}$$

with the amplitude ε_h and the functions $h_x(x)$ and $h_z(z)$ depending on the chord- and spanwise coordinate, respectively. $h_x(x)$ builds on the smooth step function S used in Schrader *et al.* (2008), rising from $x = h_{start}$ along the flank h_{rise}, falling till $x = h_{end}$ along h_{fall} and centered at the location $x_r = (h_{start} + h_{end})/2$, which is the nominal roughness station. $h_z(z)$ is obtained through an

TABLE 1. Parameters of the surface-roughness shape in equation (16).

ε_h	h_{start}	h_{end}	h_{rise}	h_{fall}
0.05, 0.1	6	34	12	12

expansion in sinusoidal functions with 16 different spanwise wavenumbers and random phases. $h_x(x)$ and $h_z(z)$ then read

$$h_x(x) = \left[S\left(\frac{x-h_{start}}{h_{rise}}\right) - S\left(\frac{x-h_{end}}{h_{fall}}+1\right)\right] \tag{14a}$$

$$h_z(z) = \sum_{n=1}^{16} \sin\left(n\beta_0 z + \phi_n^{rand}\right) \tag{14b}$$

with the fundamental spanwise wavenumber $\beta_0 = 2\pi/L_z$ defined by the spanwise width L_z of the computational domain and a random angle ϕ_n^{rand}. The characteristic roughness height ε_h in equation (13) is

$$\varepsilon_h = \sqrt{\overline{h_z^2}}\Big|_{x_r} \quad , \tag{15}$$

i.e. the root-mean-square of the random spanwise hump contour at the roughness station x_r. The parameters of the roughness contour are compiled in table 1, and the chord- and spanwise roughness contours h_x and h_z are shown in figure 2(b) for a characteristic amplitude of $\varepsilon_h = 0.1$.

2.5. *Computational domain*

The present study consists of two parts – (1) the identification of the characteristic disturbance structures inside the layer throughout the entire transition process and (2) the description of the receptivity and the early stages of instability of the swept-plate boundary layer. Therefore, two computational domains with different chordwise length are used herein, a long one, "L", to capture the breakdown of the boundary layer and a short one labelled "S" for the receptivity study. The size $L_x \times L_y \times L_z$, resolution $N_x \times N_y \times N_z$ and length L_{fringe} of the fringe region of the boxes L and S are listed in table 2 together with the Reynolds number $Re_{\delta^*,0}$ defining the location of the inflow plane. Dimension and resolution of the numerical domain have been chosen after a preceding study on the influence of the domain size and the sub-grid scale stresses reported in the following.

2.5.1. *Domain size and resolution study*

The resolution in wall-normal direction y is finer than in the wall-parallel planes, see table 2, in particular inside the boundary layer due to the clustering of the Chebyshev points near the wall. The normal resolution is in fact comparable to that in Brandt *et al.* (2004), where sub-grid scale models were not used. Since the flow is swept at 45°, the resolution requirements in x and z direction are

TABLE 2. Size and resolution of the computational domains "L" and "S", length of the fringe region and inflow Reynolds number.

Box	$Re_{\delta^*,0}$	$L_x \times L_y \times L_z$	$N_x \times N_y \times N_z$	L_{fringe}
L	220	$1500 \times 90 \times 200$	$768 \times 121 \times 128$	135
S	220	$750 \times 90 \times 200$	$384 \times 121 \times 128$	80

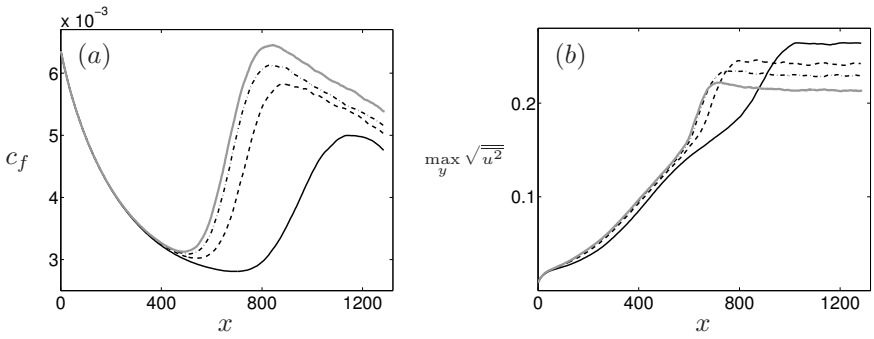

FIGURE 3. Boundary-layer response to free-stream turbulence with $Tu_0 = 3.96\%$ and $L = 10$. Study of the influence of chordwise resolution of the computational domain "L" on (a) the skin-friction coefficient and (b) the evolution of the wall-normal maximum of the root-mean-square of the chordwise disturbance-velocity component. $N_x = 256$ (—-); 384 (----); 512 (-·--·) and 768 (——, grey).

expected to be similar. The choice of resolution is motivated by the disturbance structures inside the boundary layer, which are expected to be elongated and almost aligned with the free-stream velocity. The laminar structures preceding the breakdown, which will be cross-flow modes, can thus be fully resolved, while the SGS model will compensate mainly for unresolved small wall-parallel length scales occurring after the turbulent breakdown. The simulations feature a wall-normal resolution typical for DNS and the resolution study is therefore restricted to the chord- and spanwise direction. Figure 3 shows in (a) the influence of the chordwise resolution on the skin-friction coefficient and in (b) the chordwise fluctuation amplitude in terms of the maximum of the root-mean-square, both obtained with the long box L. The downstream development of skin friction is often used as an indicator for the laminar-turbulent transition location in the boundary layer. The results are clearly resolution dependent: The transition location, identified by the rapid increase of the skin-friction, moves drastically upstream as the chordwise resolution is increased from $N_x = 256$ to $N_x = 384$. This trend becomes slower at a further increase in resolution, and the transition location is observed at nearly the same downstream location when the numerical resolution is further refined from $N_x = 512$ to 768. The

reason for the strong dependence of the transition location especially at the lowest values of N_x becomes evident in figure 3(b): While the early transient and linear growth phase is captured with similar accuracy in the different cases, the subsequent rapid amplification observed around $x \approx 600$ is completely underpredicted on the coarser domains (as discussed later, this stage is related to the appearance of high-frequency secondary instability of the cross-flow modes). Small structures responsible for the excitation of secondary instability are not represented on the coarsest grids. As shown in Monokrousos *et al.* (2008), an accurate LES of transitional flows needs to account for all physical mechanisms involved. These authors demonstrate that, despite the lower resolution used in the LES a good prediction of the dominating flow physics and the processes leading to turbulent breakdown can be obtained via appropriate subgrid-scale modelling. It is also shown in Monokrousos *et al.* (2008) that the LES is able to capture the instantaneous structures just prior to turbulent breakdown. Here, it is concluded from figure 3 that a further refinement of the mesh beyond 768 nodes (below $\Delta x = 1.95$) will only weakly affect the results while significantly increasing the computational costs. As shown later, we are indeed able to resolve the relevant instantaneous structures just prior to turbulent breakdown at this resolution.

On the short domain S, on the other hand, a finer resolution is computationally feasible. Two modifications of box S in table 2 are considered, first a refinement in the streamwise direction, from $\Delta x = 1.95$ to 1.46, and second a higher resolution (1.5 times) in the z direction. The vortical perturbation prescribed at the inlet of the original and the modified domains is composed of modes with wavenumbers between $\kappa_l = 0.05$ and $\kappa_u = 1.1$ with a turbulence intensity of $Tu_0 = 2.53\%$ and a characteristic length of $L = 10$. It becomes clear from figure 4(a) that the receptivity and the subsequent growth of the instability obtained on the coarsest grid do not differ from the results on the two refined meshes. From this plot and figure 3 it can be concluded that the resolution adopted here is fine enough.

Next, the influence of the width L_z of the numerical domain on the boundary-layer response is examined. This is investigated here by considering the shorter box S with $L_z = 300$ and $N_z = 192$, i.e. the spanwise resolution is kept fixed. For a fair comparison, the parameters defining the free-stream turbulence are left unchanged: the turbulence intensity considered is $Tu_0 = 3.96\%$ and the integral length $L = 10$. Figure 4(b) shows the downstream evolution of the excited boundary-layer disturbance in the wider domain as well as in box S. The initial transient disturbance growth is slightly enhanced in the wider domain whereas the disturbance growth rate further downstream is hardly affected. This difference can be explained by the nonlinear interactions occurring between wider structures at the initial receptivity phase. The spanwise scale of the disturbance is not changed by the increased domain size as shown by the identical growth rates downstream. Note, however, that the results are obtained for the second highest free-stream turbulence intensity studied, $Tu_0 = 3.96\%$,

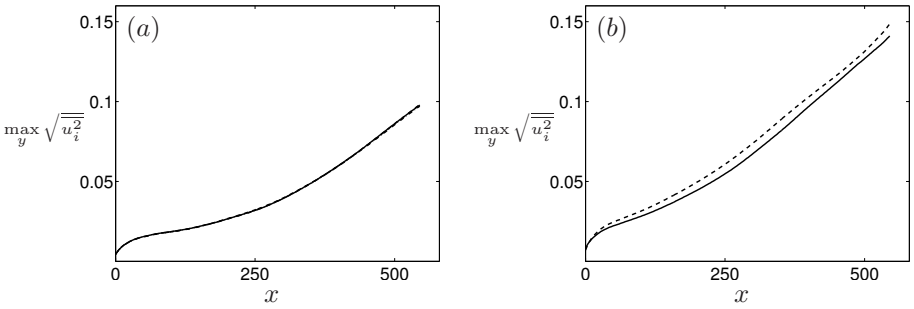

FIGURE 4. Study of the influence of resolution and size of the computational domain. Boundary-layer response to free-stream turbulence with $L = 10$. (a) $Tu_0 = 2.53\%$. Variation of chord- and spanwise resolution of box S, see table 2. $N_x \times N_y \times N_z = 384 \times 121 \times 128$ (——); $512 \times 121 \times 128$ (----); $384 \times 121 \times 192$ (-·-·-). (b) $Tu_0 = 3.96\%$. Variation of spanwise size of box S. $L_z = 200$ (——); $L_z = 300$ (----).

and the agreement between the curves is expected to become better at lower Tu_0. In light of the rather small influence of L_z on the boundary-layer response and for the sake of the computational costs the subsequent simulations are performed on the default domain in table 2 with $L_z = 200$.

2.6. *Characterization of the free-stream turbulence*

The numerical generation of the turbulent free-stream perturbation has been outlined in subsection 2.4. Due to the distribution of the disturbance wavenumbers on concentric spherical shells with equidistant spacing the resulting disturbance field is homogeneous and isotropic. In swept-plate flow with favorable pressure gradient, however, the mean flow is subject to chordwise acceleration, i.e. $\frac{\partial U}{\partial x} > 0$. This gives rise to non-zero production terms in the Reynolds-stress transport equation, see for instance Pope (2001). Thus, the three fluctuation components will not decay at the same rate, but a redistribution of turbulent kinetic energy among the components is expected. The turbulent disturbance field will then deviate from the initial isotropic state as the perturbation is convected downstream. Figure 5 displays the behavior of the artificial turbulence field in the free stream. In figure 5(a), the downstream decay of the turbulence intensity at three different levels above the plate is plotted. The turbulent inflow conditions are $Tu_0 = 3.96\%$ with $L = 10$. It is apparent that the turbulence intensity decays at a rate similar to that in homogeneous isotropic turbulence, where the energy decay obeys a power law. In Fransson *et al.* (2005) the exponent of this law has been experimentally determined as -0.6 for grid-generated turbulence, while the parameters C and x_r depend on the turbulence grid. Here, the curve fit has been done with $C = 1.73$ and $x_r = -600$. The plot also shows that the decay rate depends only weakly

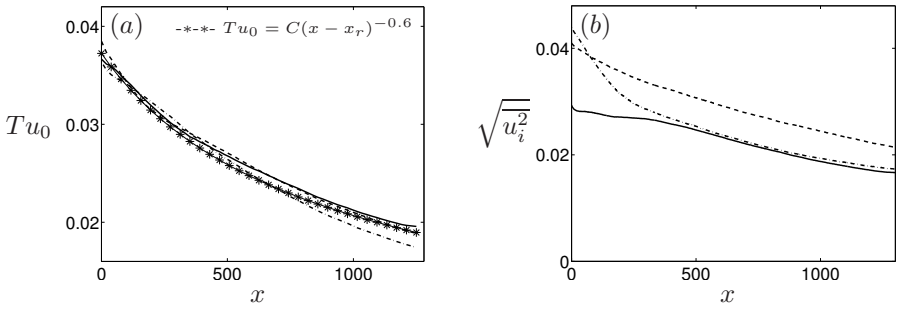

FIGURE 5. Downstream decay of free-stream turbulence with inflow turbulence intensity of $Tu_0 = 3.96\%$ and integral length $L = 10$. (a) Downstream evolution of Tu_0 measured at three levels above the plate, $y = 30$ (——); 35 (----) and 45 (-·-·-). Comparison with energy decay characteristic for grid turbulence (-∗-∗-), see Fransson *et al.* (2005). Here, $C = 1.73$ and $x_r = -600$. (b) Decay of the three fluctuation components measured at $y = 40$ for free-stream turbulence with $Tu_0 = 3.96\%$. $\sqrt{\overline{u^2}}$ (——); $\sqrt{\overline{v^2}}$ (----) and $\sqrt{\overline{w^2}}$ (-·-·-).

on the wall-normal level and hence that homogeneity is maintained across the free stream. However, figure 5(b) reveals that the turbulent kinetic energy is not equally distributed among the fluctuation-velocity components, and their individual decay differs. The adjustment to the free-stream conditions is occurring already in the fringe region and in the region near the inflow plane where $\frac{\partial U}{\partial x}$ and the streamline curvature are maximum. The wall-normal fluctuations are larger than their chordwise counterpart. This can be explained by considering the production terms in the Reynolds-stress transport equation for the chordwise u and wall-normal v fluctuations in accelerating flows.

$$\mathcal{P}_{11} = -2\overline{u^2}\frac{\partial U}{\partial x} \quad , \tag{16a}$$

$$\mathcal{P}_{22} = -2\overline{v^2}\frac{\partial V}{\partial y} = 2\overline{v^2}\frac{\partial U}{\partial x} \quad . \tag{16b}$$

A negative production term is seen in the first equation, whereas positive production of wall-normal fluctuations is caused by the flow acceleration where the continuity equation has been used to relate the mean flow gradients. Energy is drained from the u-component of the free-stream turbulence into the v-component by the chordwise acceleration of the underlying mean flow. The spanwise velocity fluctuations, initially strong, decay rapidly until they reach amplitudes similar to those pertaining to u. The relative enhancement of the wall-normal fluctuations can be also related to the stretching of chordwise vorticity, as observed e.g. in the convergent section of a wind tunnel, while the drop of u and w to the decrease of wall-normal vorticity induced by the negative $\frac{\partial V}{\partial y}$.

TABLE 3. Amplitude of the forcing disturbance. Turbulence intensity of the free-stream turbulence at the inflow plane and root-mean-square height of the surface-roughness strip.

Disturbance source	Amplitude	
Free-stream turbulence	$Tu_0 \cdot 10^2$	0.17; 0.42; 0.84; 1.26; 1.69; 2.11; 2.53; 2.95; 3.96; 5.06
Surface roughness	$\varepsilon_h \cdot 10^2$	5; 10

3. Results

The response of the three-dimensional swept-plate boundary layer to different disturbance environments is studied under the condition of a favorable pressure gradient. Three perturbation scenarios are considered: a turbulent field residing in the free stream and entering the numerical domain at the inflow plane, a spanwise oriented surface-roughness strip with random amplitude placed just downstream of the inlet and the combination of both disturbance sources. The effect of the disturbance amplitude on the boundary-layer response is investigated, where the amplitude is expressed in terms of the turbulence intensity for the free-stream disturbance and the root-mean-square height for the roughness. The values considered are compiled in table 3. First, results obtained on the long computational domain (box L) under a high-amplitude disturbance environment are presented. This ensures that the breakdown of the boundary layer to the turbulent state is captured inside the computational domain. The aim of this first part is to illustrate the transition to turbulence of the swept-plate boundary layer and to identify the relevant disturbance structures prior to transition. In the second part, the early stages – receptivity and growth of the primary instabilities – are documented through results obtained on the short domain (box S). Here, also perturbation sources with lower amplitude are considered to identify when and where nonlinear interaction between the different boundary-layer disturbance structures becomes important. The statistics presented in the following are obtained by averaging in time and in the spanwise direction.

3.1. *Part I: Breakdown*

The skin-friction coefficient provides a good indication of the transition location. This is shown in figure 6(a) for free-stream turbulence with inflow intensities of $Tu_0 = 2.53\%$ and 3.96%. The completion of transition is observed at lower Re_x when increasing the level of the external disturbance.

Perturbations enter the boundary layer in the form of low-frequency modes elongated in the free-stream direction. The wall-normal maximum of the chordwise and spanwise velocity fluctuations is reported in figure 6(b). In swept boundary layers, susceptible to cross-flow exponential instabilities, all components of the perturbation velocity are seen to grow at a similar rate, see the range $Re_x \in [1 \cdot 10^5, 2 \cdot 10^5]$. This is typical of modal instability; in the

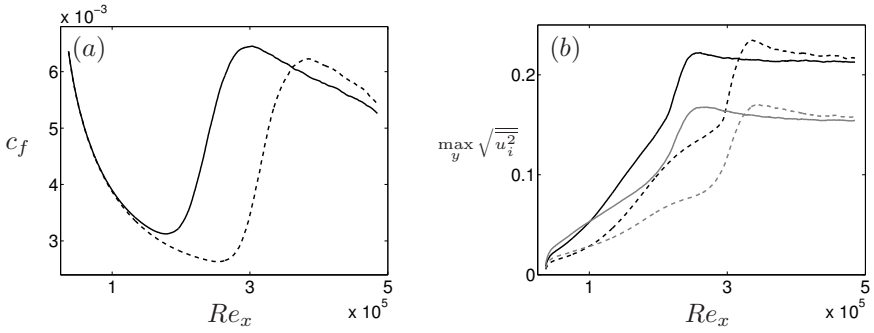

FIGURE 6. Visualization of the breakdown to turbulence of swept-late boundary-layer flow exposed to free-stream turbulence with inflow turbulence intensity of $Tu_0 = 2.53\%$ (----) and 3.96% (——) through (a) the rise in skin friction and (b) the downstream evolution of the chord- (black) and spanwise disturbance-velocity components (grey).

two-dimensional flat-plate boundary layer, indeed, only the streamwise velocity component is seen to grow at the initial stages of the transition while the cross-stream components decay (Brandt *et al.* 2004). This flow is characterized by the non-modal amplification of the streaks. After this initial phase, a fast increase in amplification rate is observed first for the case of highest free-stream turbulence, $Re_x \approx 2.2 \cdot 10^5$, and later for the lower intensity $Tu_0 = 2.53\%$, $Re_x \approx 3 \cdot 10^5$. This is associated to the rise in skin friction coefficient in figure 6(a) and to the appearance in the flow of high-frequency secondary instabilities and of turbulent spots. The overshoot in the curves for the velocity fluctuations can be related to the maximum values of the skin friction. At the end of the computational domain the level of velocity fluctuations is almost the same for the two cases; this indicates that the flow is reaching a fully turbulent state. An overall picture of the transition in swept boundary layers exposed to free-stream turbulence is provided in figure 7. This figure displays a time series of snapshots of the flow in a wall-parallel plane in side the boundary layer, $y = 2$, together with a view of the free-stream fluctuations in a plane located at $y = 40$, that is well above the shear layer close to the wall, figure 7(a). The results are obtained with an inflow turbulence of intensity $Tu_0 = 3.96\%$ and length scale $L = 10$, and the snapshots are taken after the flow field has reached a statistically converged state. The flow is from left to right. As seen in (a), the finer length scales of the external disturbance disappear further downstream, indicating the decay of the free-stream turbulence. Plots (b) through (g) show that the instabilities in the laminar region of the boundary layer appear in the form of long structures, tilted about 45° with respect to the chord of the plate. Around $x = 500$ these structures have reached an amplitude high enough for

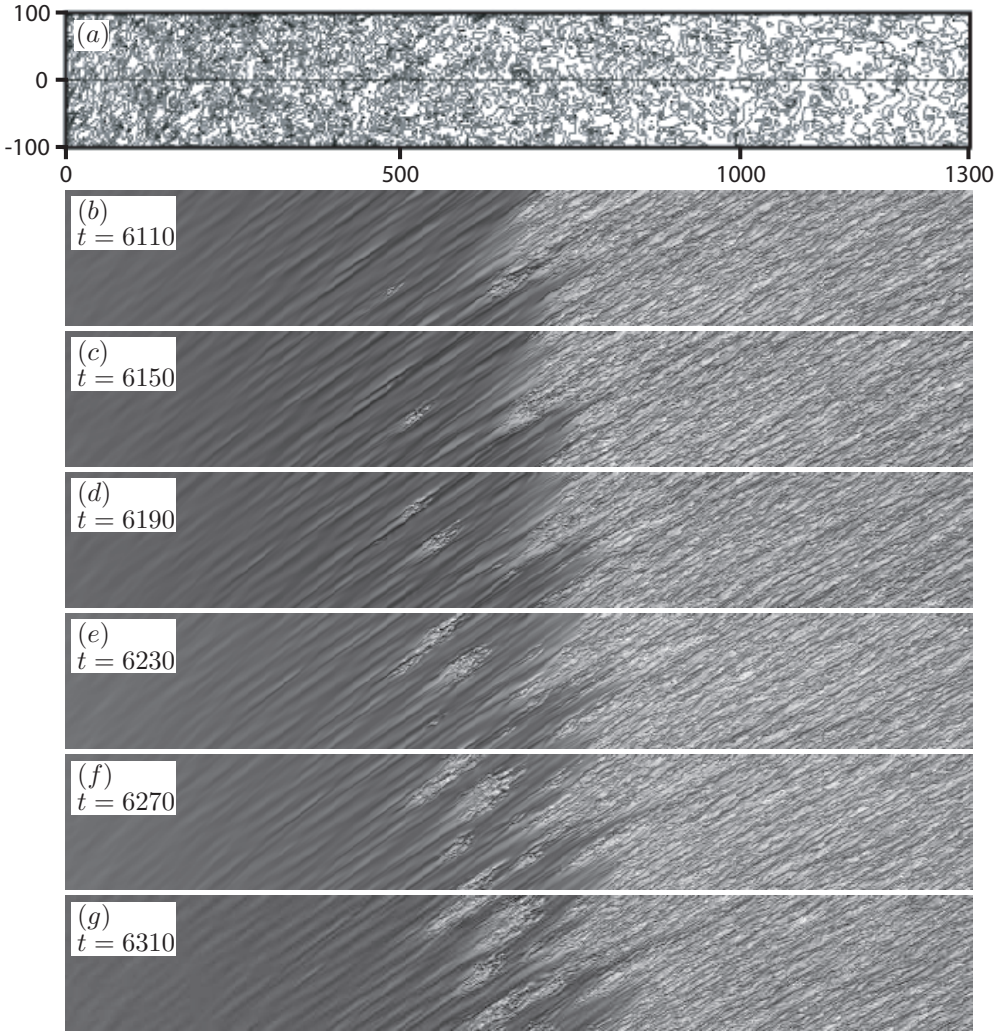

FIGURE 7. Free-stream turbulence with intensity $Tu_0 = 3.96\%$ and integral length $L = 10$ and the response of the swept-plate boundary layer to it. The flow is from left to right. (a) Downstream evolution of the chordwise fluctuation u in the free stream at $y = 40$. (b)-(g) Boundary-layer response in terms of the chordwise fluctuation u at $y = 2$ at different instants of time.

the boundary layer to become susceptive to secondary instabilities. These high-frequency modes are triggered at random locations by the high-frequency components of the free-stream turbulence and grow rapidly in amplitude. Patches

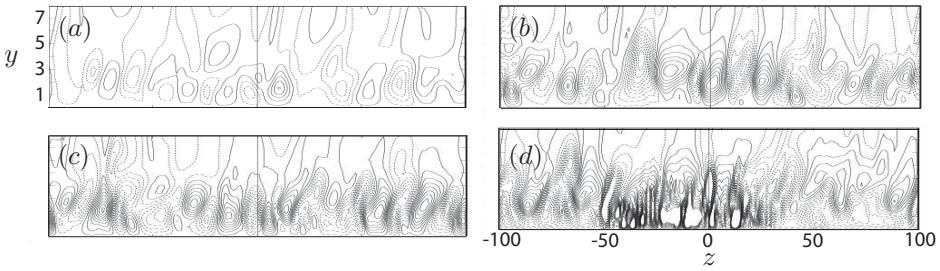

FIGURE 8. Boundary-layer response to free-stream turbulence with intensity $Tu_0 = 3.96\%$ and integral length $L = 10$. y-z planes showing contour lines of chordwise disturbance velocity in the boundary layer at four chordwise locations upstream of the breakdown location. (a) $x = 200$, (b) $x = 400$, (c) $x = 500$ and (d) $x = 600$. The contour lines show level between -0.1 and +0.1 with spacing $\Delta = 0.01$; solid lines indicate $u \geq 0$, dashed lines $u < 0$. Note that the plots are not at an equal aspect ratio.

of irregular motion are seen to appear further downstream, forming local regions of turbulence called spots. The spot first seen in figure 7(b) grows in size with time; a second spot occurs in plot (c) and both become wider and longer as they travels downstream. At time $t = 6230$, figure 7(e), a third spot can be identified in the lower part of the domain, and later , image (g), the three turbulent spots have almost merged to form one large region of turbulent motion. Downstream of $x = 700$ the boundary layer is fully turbulent, and the turbulent region is constantly fed by new merging spots incident from the upstream laminar part of the layer. It becomes apparent that the dominant disturbance structures in the fully turbulent boundary layer are still elongated and tilted in the free-stream direction (Schlatter & Brandt 2008).

Figure 8 characterizes the wall-normal and spanwise length scales of the disturbance structures inside the boundary layer by showing contour lines of the chordwise disturbance velocity in the cross-stream plane at four different downstream locations. At $x = 200$, plot (a), the instability structures still feature rather low amplitudes and large spanwise length scales of about 10, i.e. comparable to the integral length of the forcing free-stream turbulence. Further downstream, at $x = 400$ and 500, the cross-flow modes have amplified, the gradients in u have become steeper and the structures have grown in size in the wall-normal direction with the boundary layer, while their spanwise size has decreased with respect to the layer thickness, see plots (b) and (c). In figure 8(d) a region of large disturbance amplitudes, steep gradients in u and fine spanwise scales is identified near the center of the domain, while the perturbation field in the neighborhood is smoother. This highly perturbed region is what we refer to as turbulent spot and indicates where the boundary layer first approaches the turbulent state. Note also that these turbulence patches are located closer

to the wall than the original cross-flow modes. Similarly to the case of two-dimensional boundary layers, the late-stage high-frequency instability is coming from the upper part of the boundary layer towards the wall (Jacobs & Durbin 2001; Brandt *et al.* 2004; Zaki & Durbin 2005).

3.2. *Part II: Receptivity*

First, free-stream turbulence with different turbulence intensity is considered. The synthetic turbulence is prescribed at the inflow plane of the computational domain and is convected in the free stream while decaying. This disturbance source will therefore fill the entire free stream and act non-locally on the boundary layer. Secondly, the boundary-layer response to surface roughness is investigated. A thin roughness strip with a step-like contour in x- and a random shape in z direction is placed parallel to the leading edge near the inflow plane of the domain. This disturbance source is hence confined to a small downstream region and interacts locally with the boundary layer, in contrast to the free-stream turbulence. Finally, both free-stream turbulence and roughness are included at the same time in the simulation. This enables us to address a frequently discussed issue in the context of three-dimensional swept-plate boundary layers, namely whether the boundary-layer response is dominated by steady or unsteady disturbances. The following results are obtained on the short domain, box S, which is sufficiently long to include receptivity, primary disturbance growth and nonlinear interaction even for the lowest amplitudes of the forcing disturbance.

3.2.1. *Response to free-stream turbulence*

Figure 9 depicts the downstream evolution of the boundary-layer disturbance forced by free-stream turbulence with different intensities in the range $Tu_0 \in [0.17, 5.06]\%$. The free-stream turbulence intensity is defined by its value at the inflow plane, thus when the effects of the flow acceleration have already been active, see discussion in section 2.6. In figure 9(a) and (b) the wall-normal maximum of the root-mean-square of the chordwise fluctuation u is shown versus Re_x for increasing inflow turbulence intensities. This quantity is the most commonly used indicator of the growth of the disturbances inside the boundary layer. The results pertaining to the lowest turbulence intensities are reported in (a), while those for the highest free-stream turbulence levels are shown in (b). Note that the curve obtained at lowest Tu_0 is repeated in figure (b) for comparison. Initially, $Re_x \lesssim 5 \cdot 10^4$, the instability growth is dominated by transient behavior, followed by a region of almost linear growth. The linear regime extends nearly throughout the whole domain for the weak free-stream perturbations with $Tu_0 = 0.17\%$ and $Tu_0 = 0.42\%$, whereas the curves obtained in a disturbance environment of higher intensity start to bend off for $Re_x > 1.5 \cdot 10^5$. This indicates that nonlinear interaction between individual disturbance components becomes relevant for $Tu_0 > 0.42\%$, causing

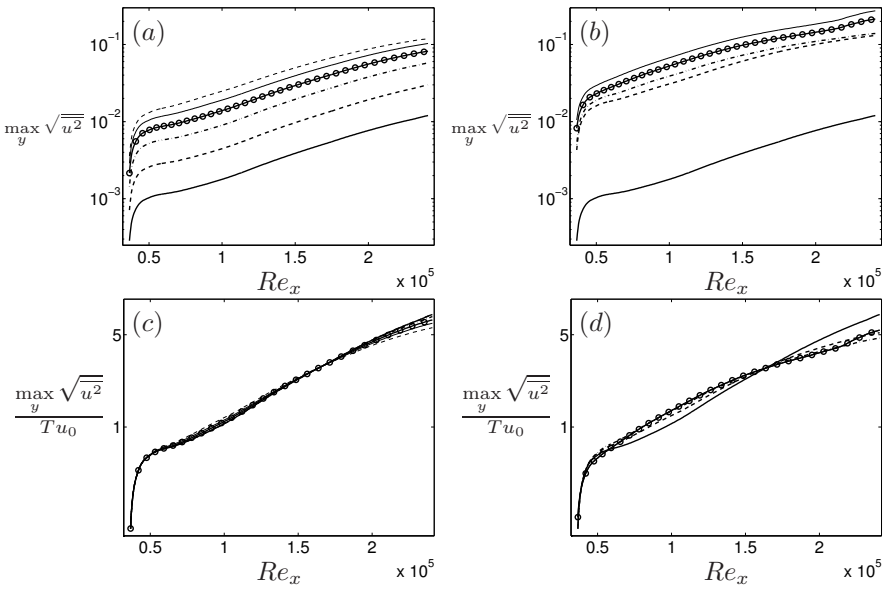

FIGURE 9. Boundary-layer response to free-stream turbulence with integral length $L = 10$ and different intensities: (a) $Tu_0 =$ 0.17% (——); 0.42% (----); 0.84% (-·-·-); 1.26% (-○–○-); 1.69% (——, thin) and 2.11% (----, thin). (b) $Tu_0 = 0.17\%$ (——); 2.53% (----); 2.95% (-·-·-); 3.96% (-○–○-) and 5.06% (— –, thin). (c) shows the data from (a) scaled with the inlet turbulence intensity Tu_0 and (d) the curves from (b) scaled by Tu_0.

saturation of the primary disturbances. At the highest inflow turbulence levels of $Tu_0 = 3.96\%$ and 5.06%, secondary instability growth is already seen within the short domain, apparent through the upward bending growth curve for $Re_x \gtrsim 2.2 \cdot 10^5$. The extent of the region of linear exponential growth and the onset of nonlinear behavior becomes clearer in the figures 9(c) and (d), where the curves of the plots (a) and (b) are shown after re-scaling with the inflow turbulence intensity. Clearly, the initial disturbance amplitude and the incipient transient growth scale with Tu_0 for all intensities under investigation, indicating that the receptivity process is linear. In particular, the first data point at $Re_{x,0}$ can be interpreted as the receptivity coefficient based on Tu_0, describing the efficiency of receptivity to free-stream turbulence. Here, a value of about 0.17 is obtained. At the lower intensities in figure 9(c), the primary instability growth depends linearly on Tu_0 in the region with $Re_x \lesssim 1.7 \cdot 10^5$, while saturation of the amplitude sets in further downstream. Figure 9(d) reveals that the curves obtained at the higher intensities Tu_0 do not collapse as well with the data for $Tu_0 = 0.17\%$ as in (c), showing that the dependence

of the primary instability evolution on the incoming turbulence intensity becomes nonlinear at the highest levels of Tu_0 considered here. In particular, the larger amplification observed can be explained by the nonlinear forcing among unsteady modes of low frequency and different spanwise scale.

The turbulent free-stream perturbation is composed of a large number of spanwise length scales and time scales and will therefore excite cross-flow modes with different spanwise wavenumbers β and angular frequencies ω inside the boundary layer. This leads on the one hand to initial transient disturbance growth, as discussed above, but on the other hand also to a competition between unstable modes with different β and ω, growing at different rates and becoming dominant at different downstream locations. Therefore, the curves for the evolution of the boundary-layer instabilities in figure 9 do not exhibit a clean exponential behavior; instead, they represent the envelope for the evolution of individual unstable cross-flow waves. Figure 10(a) provides data for the downstream development of the amplitude of a large number of unstable modes with $\omega = -0.01$ and with various spanwise wavenumbers. The curves are obtained through the solution of the Parabolized Stability Equations (PSE). As the receptivity is not included in the PSE framework, the evolution curves need to be weighted with the corresponding receptivity coefficients. Here, the coefficients for vortical free-stream disturbances computed by Schrader *et al.* (2008) and displayed in the insertion of figure 10(a) are used. In order to obtain the total amplitude of the boundary-layer disturbance, the envelope of the weighted amplitude-evolution curves is computed and compared with the present results from the full nonlinear simulation of a swept boundary layer exposed to free-stream turbulence in figure 10(b). Although the envelope curve only includes cross-flow modes with frequency $\omega = -0.01$ it provides a good approximation of the actual disturbance growth observed in the simulations. This demonstrates on the one hand that low frequencies like $\omega = -0.01$ play a major role during the receptivity process and on the other hand that the receptivity coefficients computed in Schrader *et al.* (2008) for the single free-stream vortex also describe receptivity to free-stream turbulence properly.

Next, the characteristic size and spacing of the boundary-layer instability structures is investigated. In figure 11 the spacing Δz between the disturbance structures in the region of primary instability growth is displayed versus the chordwise coordinate. Δz is determined by computing the spanwise two-point correlations $\overline{u(z)u(z+\Delta z)}/\overline{u^2(z)}$ for the chordwise fluctuation u and is defined as twice the location Δz_{min} of the first minimum of the obtained correlation curve, $\Delta z(x) = 2\Delta z_{min}(x)$. It can be interpreted as the spanwise spacing between two adjacent instability structures with a disturbance velocity in the same direction, for instance two contiguous cross-flow modes or two high-speed streaks. Figure 11(a) shows the characteristic spacing obtained under free-stream turbulence of the lower intensities $Tu_0 \leq 1.69\%$, revealing that Δz is independent of Tu_0 in this range and that it slowly drops downstream. In (b)

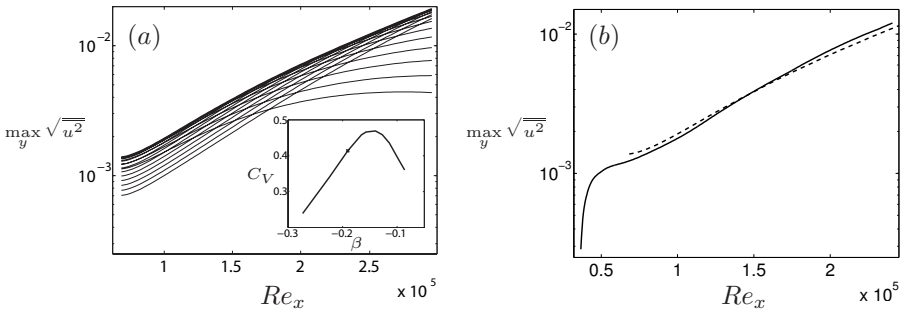

FIGURE 10. Boundary-layer response to forcing with free-stream turbulence of $Tu_0 = 0.17\%$. (a) Growth of cross-flow modes with angular frequency $\omega = -0.01$ and various spanwise wavenumbers in the range (-0.27,-0.09) obtained through the PSE method (——, thin). The curves are weighted with the corresponding receptivity coefficients (insertion, from Schrader *et al.* (2008)). The envelope curve is also shown (——, thin). (b) Boundary-layer response for $Tu_0 = 0.17\%$ (——) in comparison with the envelope curve from (a) (----).

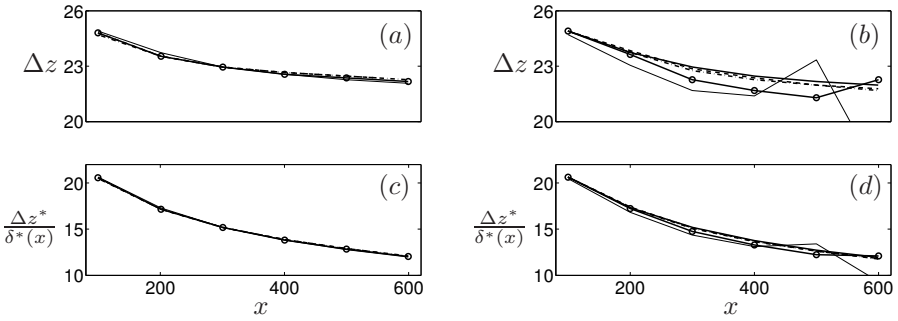

FIGURE 11. Characteristic spanwise spacing between the disturbance structures excited by free-stream turbulence at various intensities. (a) $Tu_0 = 0.17\%$ (——); 0.42% (----); 0.84% (-·-·-); 1.26% (-○–○-); 1.69% (——, thin) and 2.11% (----, thin). (b) $Tu_0 = 0.17\%$ (——); 2.53% (----); 2.95% (-·-·-); 3.96% (-○–○-) and 5.06% (——, thin). (c) and (d) show the same data as (a) and (b), respectively, but Δz is normalized by the local instead of the inflow displacement thickness.

a slightly faster decrease of the spacing is observed for the more intense free-stream fluctuations, in particular for the two largest values of $Tu_0 = 3.96\%$ and 5.06%. This is in line with the experimental findings in Matsubara & Alfredsson (2001) for the two-dimensional boundary layer exposed to turbulence from grid B, where the downstream decrease in spacing has been reported to be slower

under free-stream turbulence of low intensity than in high-level turbulence. Note also the rapid drop in Δz for $Tu_0 = 5.06\%$ downstream of $x = 500$, revealing that breakdown to turbulence is observed within the domain at this high intensity. The disturbance structures prior to transition break rapidly up into smaller scales in this region. Upstream of the location of breakdown, Δz increases somewhat before it finally drops. The increase in spacing is also seen at the second highest turbulence intensity of $Tu_0 = 3.96\%$, indicating that transition is imminent. In the plots 11(c) and (d) the data from (a) and (b) are shown re-scaled with the local displacement thickness instead of its inflow value. These figures demonstrate that the characteristic size of the primary instability decreases relative to the local size of the boundary layer for all values of Tu_0.

3.2.2. *Response to surface roughness*

As demonstrated in Crouch (1993), Choudhari (1994) and Schrader *et al.* (2008), for example, steady surface roughness provides an efficient receptivity mechanism for steady cross-flow vortices. Here, a chordwise localized spanwise surface-roughness strip with the shape shown in figure 2(b) is placed on the plate near the inflow plane of the computational domain, while the free stream is now disturbance-free. Two roughness elements with different root-mean-square heights are considered, $\varepsilon_h = 0.05$ and 0.1. In comparison with the humps used in Schrader *et al.* (2008) these amplitudes appear to be large; however, the total perturbation induced by the roughness strip will be distributed among the 16 spanwise wavenumbers present in the bump shape. Due to the forcing at various wavelengths, different cross-flow waves may appear at the same time and compete with each other. This is seen in figure 12, showing the response of the boundary layer to forcing through the roughness strips with $\varepsilon_h = 0.05$ and 0.1. In figure 12(a) the growth of various steady cross-flow modes with spanwise wavenumbers included in the roughness contour is depicted. The curves are weighted with the corresponding receptivity coefficients for roughness taken from Schrader *et al.* (2008) and their envelope is computed and compared with the downstream evolution of the disturbance amplitude observed in the simulations with random roughness strip, see figure 12(b). The envelope is dominated by the cross-flow mode $\beta = -0.22$, the mode of strongest receptivity among those forced in the simulation (Schrader *et al.* 2008). The agreement between the envelope and the evolution curve for the boundary-layer disturbance is good, revealing that the receptivity coefficients computed within the linear approximation and for the simplified roughness model in Schrader *et al.* (2008) are also valid for the receptivity to the more complex roughness strip considered here. The nonlinear interaction between the forced cross-flow waves is not significant at the present roughness amplitudes; instead, the disturbance growth exhibits a rather clean exponential behavior. Moreover, the dependence of the boundary-layer response on the characteristic roughness height is linear for the values of ε_h considered, that is, the solid curve for $\varepsilon_h = 0.05$ in figure 12(b) collapses with the dashed line for $\varepsilon_h = 0.1$, if the former is multiplied by

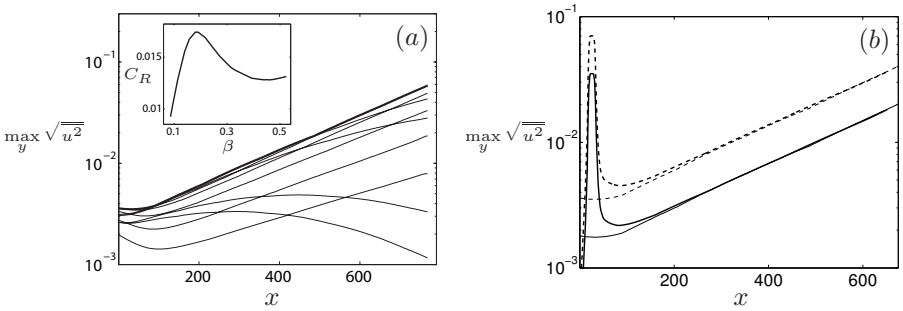

FIGURE 12. Boundary-layer response to forcing by means of a surface-roughness strip. (a) Growth of steady cross-flow modes with various spanwise wavenumbers in the range (-0.47,-0.097) and included in the spanwise shape of the roughness (——, thin). The curves are from Schrader *et al.* (2008) and weighted with the corresponding receptivity coefficients from the same reference (insertion). The envelope curve is also shown (——, thick). (b) Boundary-layer response for $\varepsilon_h = 0.05$ (——) and $\varepsilon_h = 0.1$ (----) in comparison with the envelope curve from (a) (—— and ----, thin).

2. Note again that the *rms*-value of the roughness amplitude is 10% of the local boundary-layer displacement thickness, a value higher than those typically expected in real configurations.

3.2.3. *Response to free-stream turbulence with surface roughness*

Three-dimensional boundary-layer flow in engineering applications is often subject to disturbances from more than one source. Examples are free-stream sound from the jet engine of an aircraft impinging on the boundary layer over a wing with surface imperfections or free-stream turbulence interacting with the layer over a slightly rough turbine blade. Here, we consider the combination of the two perturbation sources studied in the previous sections: turbulent fluctuations in the free stream and a localized random-roughness strip in the upstream part of the swept-plate boundary layer. As seen before, these two perturbations excite travelling and stationary cross-flow instability, respectively, which will coexist and compete with each other for the combined disturbance environment considered here. It is then of interest to determine which type of disturbance – steady or unsteady cross-flow vortices – dominate inside the boundary-layer prior to transition and cause its breakdown to turbulence. This issue has so far mostly been addressed through wind-tunnel experiments, see the review by Saric *et al.* (2003). In Schrader *et al.* (2008), a numerical analysis of the same boundary-layer flow as considered here is presented, involving the combination of simplified models for free-stream vorticity and roughness. In

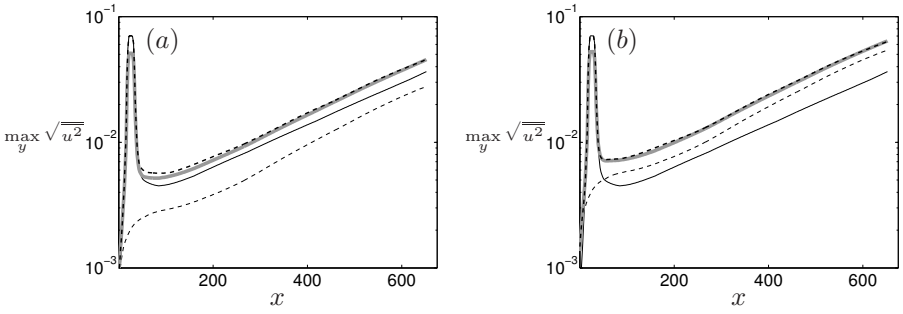

FIGURE 13. Swept-plate boundary layer exposed to turbulent fluctuations of (a) $Tu_0 = 0.42\%$ and (b) $Tu_0 = 0.84\%$ and a localized wall-roughness strip with root-mean-square amplitude $\varepsilon_h = 0.1$. The thin grey curves represent the unsteady (----) and the steady disturbance evolution (——) due to turbulence and roughness alone. Their sum (——, thick, grey) is compared with the total disturbance (----, black) observed in the simulations with combined perturbation sources.

that work, the threshold in turbulence intensity, above which travelling cross-flow instability dominates over the stationary disturbance waves has been estimated to $Tu_0 = 0.5\%$. We perform a similar analysis here but apply the more complex representations for free-stream turbulence and surface roughness described in subsection 2.4. Figure 13 shows the response of the swept-plate boundary layer for different combinations of the amplitudes Tu_0 and ε_h of the free-stream turbulence and the roughness. Two situations differing in the inflow intensity Tu_0 of the turbulent free-stream fluctuations are considered, $Tu_0 = 0.42\%$ in (a) and 0.84% in (b). The amplitude of the roughness strip is identical in both cases, namely $\varepsilon_h = 0.1$. The evolution of the boundary-layer disturbance obtained in the presence of the two perturbation sources is displayed together with the development of the perturbation induced by the free-stream fluctuations and wall roughness acting separately. In figure 13(a) the steady cross-flow modes dominate over the travelling waves, while the situation is the opposite for the larger free-stream turbulence intensity as shown in (b). It can thus be concluded that the threshold, above which the unsteady modes become significant is passed in the region $0.42\% < Tu_0 < 0.84\%$. This estimate is in agreement with the value of 0.5% given in Schrader *et al.* (2008). Figure 13 further reveals that the total boundary-layer disturbance seen in the simulations with both turbulence and roughness can be correctly estimated by summing the unsteady and the steady contribution. This observation holds in the steady wave dominated case in (a) as well as in the travelling mode dominated situation in (b) and one can speculate that it will also apply for larger and lower values of the free-stream turbulence when the unsteady and steady cross-flow modes will more clearly dominate the perturbed boundary layer.

The interaction between the travelling and stationary disturbance appears to be negligible for the configuration under consideration and an accurate prediction of the boundary layer response can therefore be obtained by considering the different disturbance sources independently.

4. Conclusions

Receptivity, disturbance growth and breakdown in the three-dimensional boundary layer developing on a swept flat plate under a favorable pressure gradient has been investigated. The flow has been perturbed through a non-localized source – a turbulent flow field in the free stream – and a localized source – a wall-roughness strip with random spanwise distribution. Also the combination of both disturbance sources has been considered. At the conditions under investigation the basic flow is unstable to cross-flow instability, and both disturbance sources are efficient in exciting travelling and stationary cross-flow vortices, respectively, inside the boundary layer.

In the first part of the paper the route of laminar-turbulent transition is illustrated by describing the disturbance structures being dominant during the different stages of transition. While there exist publications on wind-tunnel experiments in swept-plate flow, e.g. by Bippes (1999), the present work is to our knowledge the first presenting a numerical simulation of cross-flow mode dominated transition in the swept-plate boundary layer exposed to free-stream turbulence. Our study reveals that the early stages on the route to turbulence are characterized by the co-existence of non-modal disturbances (streaks) and modal instability (unsteady cross-flow waves), when free-stream turbulence acts on the boundary layer. Due to their large amplification rates the cross-flow modes dominate the disturbance environment inside the layer prior to the breakdown. This is in opposite to the two-dimensional boundary layer, where modal and non-modal disturbances co-exist, as well, but the TS-waves are not relevant in comparison to the streaks. In the three-dimensional boundary layer the growth of the unstable eigenmodes is thus not "bypassed", that is, for the present configuration laminar-turbulent transition in swept-plate flow triggered by free-stream turbulence is not bypass transition, in contrast to two-dimensional boundary-layer transition. When the roughness strip is placed on the wall the dominant pre-transitional structures are steady cross-flow vortices. Even if some transient behaviour is observed in the vicinity of the roughness, non-modal disturbances do not play any role in transition triggered through localized random roughness.

The second part of the paper focuses on the receptivity of the three-dimensional boundary layer and the early stages of primary disturbance growth. The receptivity coefficients derived in Schrader *et al.* (2008) for simplified receptivity models are applied here and compared with the amplification curves obtained from the present fully nonlinear simulations. This is in practice done by weighting the curves for the evolution of the various excited unstable modes with their individual receptivity coefficients and computing the envelope curve.

Although the receptivity model in Schrader *et al.* (2008) accounts for one – however, dominant – angular frequency only, good agreement between the amplification seen in the present simulations and the envelope has been found for the case of free-stream turbulence. This suggests that the receptivity mechanisms for the different excited modes are independent of each other and that the linear receptivity model from Schrader *et al.* (2008) is also valid for the receptivity to a complex free-stream turbulence field of relatively high intensity. The same conclusion can be drawn for receptivity to localized roughness with random spanwise amplitude, for which the agreement between the disturbance amplitudes predicted by the linear receptivity model and the amplitudes observed in the simulations is even better than for forcing through free-stream turbulence. This is, however, expected in light of the less complex disturbance environment inside the boundary layer in the case of surface roughness.

Finally, a situation has been herein studied, where unsteady and steady cross-flow vortices co-exist in the boundary layer. This is the case when free-stream turbulence acts on a three-dimensional boundary layer over a plate with localized wall roughness. As stated in the review by Saric *et al.* (2003), the stationary cross-flow vortices dominate the pre-transitional boundary layer when the intensity of the free-stream turbulence is low. This has been confirmed here: For low-amplitude roughness and an inflow turbulence intensity of about 0.4% the total boundary-layer disturbance is dominated by the steady contribution triggered by the roughness, while at a turbulence level of 0.8% the unsteady cross-flow instability is more energetic than the steady mode. This is also in line with the estimation given in Schrader *et al.* (2008), where the threshold above which travelling cross-flow waves become important has been found for a free-stream disturbance amplitude around 0.5%. Thus, for the boundary-later flow examined here, even in the presence of two distinct disturbance sources, where nonlinear interactions could be expected, a correct prediction of the transition location can be obtained investigating the development of individual cross-flow modes.

In summary, the receptivity coefficients obtained from the simplified linear models used in Schrader *et al.* (2008) can be combined with established transition-prediction tools such as the e^N-method to provide a refined prediction method including the receptivity process. This presumes, however, the exact knowledge of the receptivity coefficients for the disturbances being relevant in the flow of interest. In Schrader *et al.* (2008) it has been shown that simplified methods with less computational costs than DNS or LES, for instance the method based on Finite-Reynolds Number Theory (e.g. Crouch (1992); Choudhari (1994)), can provide accurate enough receptivity coefficients for different flows and disturbance conditions. However this is not always the case; Collis & Lele (1999) investigated by direct numerical simulation the receptivity to roughness close to the leading edge of a parabolic body. The results show that receptivity is enhanced by convex surface curvature and suppressed by non-parallelism. Comparing the receptivity coefficients from the

direct numerical simulations with several theoretical approaches, these authors concluded that the accurate prediction of cross-flow instability receptivity near a realistic leading edge must account for the strongly non-parallel flow near the upstream neutral point. Unfortunately, stability predictions using a perturbation approach for non-parallel effects proved inadequate for the most dangerous cross-flow mode for the conditions studied in this work. A similar indication on the relevance of the leading-edge region was drawn in Schrader *et al.* (2008) when analyzing the receptivity to free-stream vortical modes. Thus, while the good news are that receptivity coefficients obtained for single modes appear to be sufficient to predict the transition location in swept boundary layers even in the presence of free-stream turbulence, simpler perturbation approaches for theoretical non-parallel receptivity prediction may prove inadequate. Further research is indeed required to verify this claim.

The authors wish to acknowledge Philipp Schlatter, Antonios Monokrousos, Ardeshir Hanifi and Dan Henningson for fruitful discussions. The PSE data used were kindly provided by David Tempelmann. This research is supported by VR (The Swedish Research Council). SNIC computing facilities located at the Center for Parallel Computers (PDC), KTH, and the National Supercomputer Centre, Linköpings universitet, have been used for the computations.

References

Bippes, H. 1999 Basic experiments on transition in three-dimensional boundary layers dominated by crossflow instability. *Prog. Aerosp. Sci.* **35**, 363–412.

Brandt, L. & de Lange, H. C. 2008 Streak interactions and breakdown in boundary layer flows. *Phys. Fluids* **20** (024107), 1–16.

Brandt, L., Schlatter, P. & Henningson, D. S. 2004 Transition in boundary layers subject to free-stream turbulence. *J. Fluid Mech.* **517**, 167–198.

Chevalier, M., Schlatter, P., Lundbladh, A. & Henningson, D. S. 2007 A Pseudo-Spectral Solver for Incompressible Boundary Layer Flows. *Tech. Rep.* TRITA-MEK 2007:07. Royal Institute of Technology (KTH), Dept. of Mechanics, Stockholm.

Choudhari, M. 1994 Roughness-induced Generation of Crossflow Vortices in Three-Dimensional Boundary Layers. *Theoret. Comput. Fluid Dynamics 6* pp. 1–30.

Collis, S. S. & Lele, S. K. 1999 Receptivity to surface roughness near a swept leading edge. *J. Fluid Mech.* **380**, 141–168.

Crouch, J. D. 1992 Localized receptivity of boundary layers. *Phys. Fluids A* **4 (7)**, 1408–1414.

Crouch, J. D. 1993 Receptivity of three-dimensional boundary layers. *AIAA Paper* (93-0074).

Deyhle, H. & Bippes, H. 1996 Disturbance growth in an unstable three-dimensional boundary layer and its dependence on environmental conditions. *J. Fluid Mech.* **316**, 73–113.

Ellingsen, T. & Palm, E. 1975 Stability of linear flow. *Phys. Fluids* **18**, 487–488.

Fransson, J. H. M., Matsubara, M. & Alfredsson, P. H. 2005 Transition induced by free-stream turbulence. *J. Fluid Mech.* **527**, 1–25.

Haynes, T. S. & Reed, H. L. 2000 Simulation of swept-wing vortices using nonlinear parabolized stability equations. *J. Fluid Mech.* **405**, 325–349.

Herbert, T. 1988 Secondary instability of boundary layers. *Annu. Rev. Fluid Mech.* **20**, 487–526.

Hœpffner, J. & Brandt, L. 2008 Stochastic approach to the receptivity problem applied to bypass transition in boundary layers. *Phys. Fluids* **20** (024108), 1–4.

Högberg, M. & Henningson, D. S. 1998 Secondary instability of cross-flow vortices in Falkner-Skan-Cooke boundary layers. *J. Fluid Mech.* **368**, 339–357.

Hultgren, L. S. & Gustavsson, L. H. 1981 Algebraic growth of disturbances in a laminar boundary layer. *Phys. Fluids* **24**, 1000–1004.

Jacobs, R. G. & Durbin, P. A. 2001 Simulations of bypass transition. *J. Fluid Mech.* **428**, 185–212.

Kachanov, Y. S. 1994 Physical mechanisms of laminar boundary-layer transition. *Annu. Rev. Fluid Mech.* **26**, 411–482.

Kendall, J. M. 1985 Experimental study of disturbances produced in a pre-transitional laminar boundary layer by weak free-stream turbulence. *AIAA Paper* **85** (85-1695), 1–10.

Klebanoff, P. S. 1971 Effect of free-stream turbulence on the laminar boundary layer. *Bull. Am. Phys. Soc.* **10**, 1323.

Landahl, M. T. 1980 A note on an algebraic instability of inviscid parallel shear flows. *J. Fluid Mech.* **98, part 2**, 243–251.

Malik, M. R., Li, F. & Chang, C.-L. 1994 Crossflow disturbances in three-dimensional boundary layers: nonlinear development, wave interaction and secondary instability. *J. Fluid Mech.* **268**, 1–36.

Malik, M. R., Li, F., Choudhari, M. M. & Chang, C.-L. 1999 Secondary instability of crossflow vortices and swept-wing boundary-layer transition. *J. Fluid Mech.* **399**, 85–115.

Matsubara, M. & Alfredsson, P. H. 2001 Disturbance growth in boundary layers subjected to free-stream turbulence. *J. Fluid Mech.* **430**, 149–168.

Monokrousos, A., Brandt, L., Schlatter, P. & Henningson, D. S. 2008 DNS and LES of estimation and control of transition in boundary layers subject to free-stream turbulence. *Int. J. Heat Fluid Flow* **29**, 841–855.

Nordström, J., Nordin, N. & Henningson, D. S. 1999 The fringe region technique and the Fourier method used in the direct numerical simulation of spatially evolving viscous flows. *SIAM J. Sci. Comp.* **20**, 1365–1393.

Pope, S. B. 2001 *Turbulent Flows*. Cambridge University Press.

Reibert, M. S., Saric, W. S., Carillo, R. B. & Chapman, K. L. 1996 Experiments in nonlinear saturation of stationary crossflow vortices in a swept-wing boundary layer. *AIAA Paper* (96-0184).

Saric, W. S., Reed, H. L. & White, E. B. 2003 Stability and Transition of Three-Dimensional Boundary Layers. *Annu. Rev. Fluid Mech.* **35**, 413–440.

Schlatter, P. & Brandt, L. 2008 DNS of spatially-developing three-dimensional turbulent boundary layers. In *Direct and Large Eddy Simulation VII*. In press.

Schlatter, P., Lange, H. C. De & Brandt, L. 2007 Numerical study of the stabilisation of Tollmien-Schlichting waves by finite amplitude streaks. In *Turbulence and Shear Flow Phenomena 5* (ed. R. Friedrich, N. A. Adams, J. K. Eaton, J. A. C. Humphrey, N. Kasagi & M. A. Leschziner), , vol. II, pp. 849–854.

Schlatter, P., Stolz, S. & Kleiser, L. 2006 LES of spatial transition in plane channel flow. *J. Turbul.* **7 (33)**, 1–24.

Schmid, P. J. & Henningson, D. S. 2001 *Stability and Transition in Shear Flows*. Springer.

Schrader, L.-U., Brandt, L. & Henningson, D. S. 2008 Receptivity mechanisms in three-dimensional boundary-layer flows. *J. Fluid Mech.* .

Stolz, S. & Adams, N. A. 1999 An approximate deconvolution procedure for large-eddy simulation. *Phys. Fluids* **11 (7)**, 1699–1701.

Stolz, S., Adams, N. A. & Kleiser, L. 2001 An approximate deconvolution model for large-eddy simulation with application to incompressible wall-bounded flows. *Phys. Fluids* **13 (4)**, 997–1015.

Taylor, G. I. 1939 Some recent developments in the study of turbulence. In *Proc. 5th Intl. Congr. Appl. Mech.* (ed. J. P. Den Hartog & H. Peters), pp. 294–310. Wiley.

Wassermann, P. & Kloker, M. 2002 Mechanisms and passive control of crossflow-vortex-induced transition in a three-dimensional boundary layer. *J. Fluid Mech.* **456**, 49–84.

Wassermann, P. & Kloker, M. 2003 Transition mechanisms induced by travelling

crossflow vortices in a three-dimensional boundary layer. *J. Fluid Mech.* **483**, 67–89.

Westin, K. J. A., Boiko, A. V., Klingmann, B. G. B., Kozlov, V. V. & Alfredsson, P. H. 1994 Experiments in a boundary layer subjected to free stream turbulence. part 1. boundary layer structure and receptivity. *J. Fluid Mech.* **281**, 193–218.

White, E. B., Saric, W. S., Gladden, R. D. & Gabet, P. M. 2001 Stages of swept-wing transition. *AIAA Paper* (2001-0271).

Wintergerste, T. & Kleiser, L. 1996 Direct numerical simulation of transition in a three-dimensional boundary layer. In *Transitional Boundary Layers in Aeronautics , Proc. Colloquium of the Royal Netherlands Academy of Arts and Sciences* (ed. R. A. W. M. Henkes & J. L. van Ingen). Amsterdam, NL: North-Holland.

Wintergerste, T. & Kleiser, L. 1997 Breakdown of a crossflow vortex in a three-dimensional boundary layer. In *Direct and Large Eddy Simulation II* (ed. J.-P. Chollet), pp. 179–190. Kluwer.

Zaki, T. A. & Durbin, P. A. 2005 Mode interaction and the bypass route to transition. *J. Fluid Mech.* **531**, 85–111.

Paper 3

3

Receptivity to free-stream vorticity of flow past a flat plate with elliptic leading edge

By Lars-Uve Schrader[*], Luca Brandt[*], Catherine Mavriplis[†] & Dan S. Henningson[*]

[*]Linné Flow Centre, Department of Mechanics
Royal Institute of Technology, SE-100 44 Stockholm, Sweden

[†]Department of Mechanical Engineering, University of Ottawa, Ottawa, K1N 6N5 Canada

Internal report

Receptivity of the two-dimensional boundary layer developing on a flat plate with elliptic leading edge is studied. Vortical perturbations in the oncoming free stream are considered, impinging on two leading edges with different aspect ratio to identify the effect of bluntness. The relevance of the three vorticity components of a realistic free-stream turbulence field is illuminated by considering axial, vertical and spanwise free-stream vorticity separately at different angular frequencies. It has been found that the boundary layer is most receptive to low-frequency axial vorticity, triggering a streaky disturbance pattern dominated by alternating positive and negative streamwise perturbation velocity. This is in line with earlier numerical studies on the flat-plate boundary layer disregarding the leading edge, and we find that the effect of leading-edge bluntness is weak in the presence of axial free-stream vortices alone. On the other hand, the spanwise free-stream vorticity component is also able to excite non-modal instability in particular at low frequencies, and the upstream transient boundary-layer response to this kind of forcing is considerably stronger when the leading edge is blunt. It can thus be concluded that the total boundary-layer response to a full free-stream turbulence field is enhanced especially in the presence of a bluff leading edge. Vertical free-stream vortices are found to be least relevant for the excitation of boundary-layer instability. At high frequencies the boundary layer becomes receptive for Tollmien-Schlichting (TS) modes in particular due to spanwise free-stream vorticity. However, the amplitude of the TS waves is small compared with the streak amplitudes for the boundary layers and the free-stream perturbations investigated here.

1. Introduction

In early numerical receptivity studies on flat-plate boundary-layer flow under free-stream disturbances the effects of the leading edge have not been taken into

account. Instead, the plate has been assumed to be infinitely thin and the focus has been on the boundary-layer region downstream of the leading edge. An example is the work on acoustic receptivity based on Finite Reynolds-Number Theory, e.g. in Crouch (1992) and Choudhari & Streett (1992). Flow around a flat plate of finite thickness with an upstream vortical free-stream disturbance has theoretically been investigated by Goldstein & Wundrow (1998). Since the 1990s there is also a larger number of numerical simulations on acoustic receptivity of flow around leading edges. Here, we present results obtained by means of the Spectral-Element Method with the aim to study the receptivity to free-stream vorticity of flow over a flat plate with blunt and sharp elliptic leading edge.

1.1. *Leading-edge receptivity to sound*

In most numerical studies about receptivity to free-stream perturbations in combination with leading-edge effects the focus is on free-stream sound. Lin *et al.* (1992) investigate receptivity of the two-dimensional boundary layer on a flat plate with elliptic leading edge to a planar sound wave of frequency parameter $F = 110$, 230 and 333. The acoustic disturbance is modelled through an unsteady free-stream boundary condition for the streamwise velocity component. Three leading-edge aspect ratios are considered, $a{:}b = 3$, 6 and 9. Further, Lin *et al.* (1992) introduce the modified super-elliptic (MSE) leading edge with zero curvature at the juncture to the plate and with nearly the same nose radius of curvature as the ordinary elliptic leading edge. The mean flow is at Reynolds number $Re_b = 2400$ based on the plate half-thickness b. The authors find that receptivity of Tollmien-Schlichting (TS) waves to sound decreases with increasing aspect ratio (decreasing nose radius). The total receptivity, i.e. the sum of the contributions from the leading edge and the juncture, remains nearly constant when replacing the ordinary elliptic leading edge by a MSE shaped of same aspect ratio. The contribution of juncture receptivity to the downstream TS amplitude is substantial (up to 50%), which is due to the decay of the leading-edge induced TS wave upstream of branch I. Fuciarelli *et al.* (2000) present results obtained for a MSE leading edge with aspect ratio $a{:}b = 6$ and a mean flow at $Re_b = 2400$, as in Lin *et al.* (1992). Receptivity is measured in terms of branch-I coefficients in that work. Moreover, the effect of angle of incidence of the sound wave is studied with the result that receptivity is more than four times as efficient at an angle of 15° than in the symmetric case.

Wanderley & Corke (2001) consider sharper MSE leading edges with aspect ratios of $a{:}b = 20$ and 40. The Reynolds number is again $Re_b = 2400$ when based on plate half-thickness and $Re_L = 10^6$ when expressed in terms of the plate length. The frequency parameter of the acoustic forcing is varied between $F = 30$ and 120. The authors do not only show branch-I receptivity coefficients but also extrapolated coefficients at the leading edge. While the TS-wave amplitude at branch I is again the weakest for the sharpest leading

edge, the opposite holds for the receptivity amplitude at the leading edge. This is due to the larger decay rate of the TS wave from the leading edge to branch I in the lower adverse pressure gradient of the 40 : 1 leading edge. Wanderley & Corke (2001) also show the superposition of TS instability triggered at the leading edge and at the junction with the plate, which becomes apparent through local maxima and minima in the receptivity amplitude when plotted versus the downstream coordinate.

1.2. *Leading-edge receptivity to vortical free-stream disturbances*

In comparison with receptivity to sound, less publications on leading-edge receptivity to free-stream vortical disturbances are available. Buter & Reed (1994) present results obtained for a two-dimensional plate with MSE leading edge of aspect ratio 6 and a baseline flow at Reynolds number $Re_b = 2400$, as in Lin *et al.* (1992). The free-stream disturbance, however, is of vortical type and imposed along parts of the far-field boundary. Both symmetric and asymmetric vortical disturbances with respect to the airfoil axis are considered, and the frequency parameter is $F = 230$. The asymmetric perturbation results in an oscillating vertical disturbance component at the nose (oscillating stagnation point), leading to larger TS-wave amplitudes as compared with the symmetric vortical forcing. The TS-mode amplitudes are found to depend linearly on the forcing amplitude for both symmetric and asymmetric free-stream vorticity. However, both types of vortical disturbances cause weaker receptivity for TS waves than free-stream sound presented in Lin *et al.* (1992). Buter & Reed (1994) also investigate the influence of surface curvature by replacing the ordinary elliptic leading edge by the MSE type. Although receptivity at the juncture to the plate becomes weaker for the smoother MSE leading edge the total receptivity increases due to a larger pressure-gradient maximum and an upstream shift of branch I of the TS instability.

Due to the limitation to two spatial directions, the study of Buter & Reed (1994) is restricted to spanwise free-stream vorticity. As soon as streamwise vortices are present the disturbance environment inside the boundary layer and the transition scenario change. Modal boundary-layer disturbances like TS waves are no longer dominant, while non-modal streaky structures become important. This so-called bypass transition has been extensively studied in wind-tunnel experiments on flat-plate flow, e.g. by Kendall (1985, 1998) and Matsubara & Alfredsson (2001); Fransson *et al.* (2005), revealing the importance of low-frequency chordwise free-stream vortices for the excitation of the primary streaks. In Bertolotti & Kendall (1997) an experiment with a controlled axial free-stream vortex generated by a micro wing upstream of the leading edge is described. This type of disturbance is in fact shown there to be efficient in exciting non-modal streak-like instability in the boundary layer. A comparison between measured and numerically obtained disturbance-amplitude functions is also included in Bertolotti & Kendall (1997) and exhibits good agreement. In most of theses wind-tunnel experiments the plates were equipped with an

elliptic leading edge, which highlights the relevance of this geometry also for numerical simulations. There are numerical studies on bypass transition of the flat-plate boundary layer available in literature, for instance in Jacobs & Durbin (2001), Brandt *et al.* (2004) and Zaki & Durbin (2005). The leading edge is not included there; however, the characteristic structures of bypass transition observed in the experiments could be reproduced in these simulations. Nagarajan *et al.* (2007) consider the effect of leading-edge bluntness on bypass transition through a mixed DNS/LES approach (DNS inside the boundary layer, LES in the free stream). The leading edge is of super-elliptic shape with two aspect ratios, $a{:}b = 6$ and 10. Homogeneous isotropic turbulence is imposed at the inflow plane, and the turbulence intensity is set to $Tu = 3.5\%$ and 4.5%, while the integral length scale is $L_t = 0.03a$ and $L_t = 0.045a$. The mean-flow Reynolds number based on the semi-major axis a of the leading edge is $Re_a = 50000$. The authors show that for the sharper leading edge and lower turbulence intensity studied, transition is initiated through instabilities on low-speed streaks, as demonstrated before by Jacobs & Durbin (2001) and Brandt *et al.* (2004). In contrast, increasing the leading-edge bluntness and/or the turbulence intensity leads via the growth of a *localized*, wave-packet like streamwise vortical disturbance to transition, and the onset of transition is moved upstream. Xiong & Lele (2007) investigate by means of LES the flow around an isothermal leading edge exposed to free-stream turbulence. They consider a blunt leading edge in the form of a regular ellipse with aspect ratio $a{:}b = 3$. The mean flow is at $Re_D = 42000$, where D is the leading-edge diameter of curvature, and the free-stream turbulence intensity and length scale are $Tu = 5\%$ and $L_t = 0.1D$, respectively. The focus of their work is on the explanation of heat-transfer enhancement typically observed around the leading edge in stagnation-point flows, when free-stream turbulence is present.

Since the model for vortical free-stream perturbations used in Nagarajan *et al.* (2007) and Xiong & Lele (2007) – numerically generated isotropic turbulence – is already rather complex, it is difficult to extract details about the early receptivity process from their data. The purpose of this work is to employ simpler models for free-stream vorticity by considering streamwise, wall-normal and spanwise free-stream vortices separately.

2. Numerical approach and flow configuration

2.1. *Numerical method*

The results are obtained by using the Spectral-Element Method (SEM) proposed by Patera (1984) to solve the three-dimensional time-dependent incompressible Navier-Stokes equations. The implementation used here has been developed and described by Tufo & Fischer (1999). Within the SEM the physical domain is decomposed into sub-domains called spectral elements. In three-dimensional space these can be for instance hexahedra, tetrahedra, prisms or pyramids with or without deformation, allowing for geometric flexibility and

hence applicability to complex engineering problems. The SEM shares this flexibility with the Finite-Element Method (FEM) and is likewise a local approach. The major difference between SEM and FEM is in the choice of the basis functions to represent the solution to the governing equations on the elements: While piece-wise linear profiles are usually addressed in the FEM framework, high-order orthogonal polynomials are employed in the SEM. In the original implementation by Patera (1984) the Lagrange interpolation polynomials were defined on Gauss-Lobatto-Chebyshev points, whereas the simulation code employed here builds on interpolation at Gauss-Lobatto-Legendre (GLL) nodes. The expansion for the flow variables reads,

$$\vec{u}[\vec{x}^{(l)}(r,s,t)] = \sum_{i=0}^{N}\sum_{j=0}^{N}\sum_{k=0}^{N} \hat{\vec{u}}_{ijk}^{(l)} h_i(r) h_j(s) h_k(t) \quad . \tag{1}$$

$(r,s,t)^T$ is the local coordinate vector for element l, and $\vec{x}^{(l)}$ is the mapping onto the global GLL mesh; h_i, h_j and h_k are the N^{th}-order Lagrange polynomials in the three local spatial directions of element l and $\hat{\vec{u}}_{ijk}$ is the nodal spectral velocity coefficient. The polynomial order N of the basis functions is usually between 7 and 15 and is identical in the three spatial directions here. The spectral nature of the SEM is reflected in the exponential convergence of the solution for sufficiently smooth flow fields, as the resolution of the numerical domain is refined by raising the polynomial degree N. Apart from this so-called p-refinement the SEM provides a second refinement strategy, the h-refinement, through reduction of the size of the spectral elements. This allows for localized refinement of the computational domain, in contrast to the grids used in global spectral methods.

The time integration of the Navier-Stokes equations in the present SEM simulation code is discussed at length in Fischer (1997) and employs a high-order operator-splitting method for the temporal discretization such as in Maday *et al.* (1990). The convective terms are computed either with an explicit third-order Adams-Bashforth scheme or via a third-order backward-differentiation method, where the latter has been used for the present simulations. The spatial discretization follows from a variational formulation (see for example Fischer *et al.* 2002).

Besides the availability of local refinement, the paramount benefit of the SEM is its suitability for element-wise parallelization of the computations. The implementation by Tufo & Fischer (1999) used here is optimized for simulations on large parallel supercomputers.

2.2. *Base flow*

Semi-infinite flat plates with leading edges of modified super-elliptic shape (MSE) are considered. The super-ellipse is defined by

$$\left(\frac{y}{b}\right)^2 = 1 - \left(\frac{a-x}{a}\right)^p \quad , \tag{2}$$

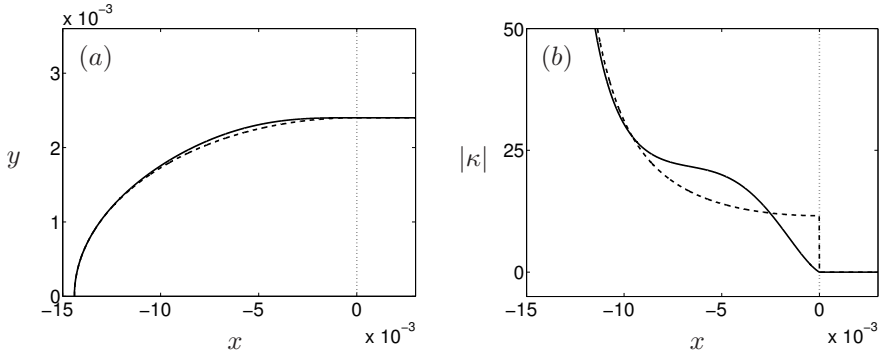

FIGURE 1. (a) Leading edge with aspect ratio a:$b = 6$ of MSE (——) and ordinary elliptic shape (----). The y axis is five times enlarged. (b) Surface curvature of the leading edges in (a). The dotted line marks the juncture between leading edge and flat plate.

where the exponent p is

$$p = 2 + \left(\frac{x}{a}\right)^2 \quad . \tag{3}$$

This type of geometry has been proposed in Lin *et al.* (1992), as it provides smoothness in curvature at the juncture to the plate, in contrast to an ordinary ellipse. a and b are the semi-major and -minor axes of the ellipse. The exponent p rises smoothly from 2 to 3 from the tip of the leading edge to the juncture with the plate, which results in zero-curvature at the juncture. To identify the influence of leading-edge curvature and thus mean-flow pressure gradient, two leading edges are herein investigated, a blunt one with aspect ratio a:$b = 6$ and a sharp one with a:$b = 20$. Figure 1(a) shows the 6:1 MSE leading edge in comparison to a leading edge with ordinary elliptic shape. The MSE type is slightly fuller than the ordinary elliptic type; however, the most remarkable feature is the smoothness in curvature at the junction with the plate seen in figure 1(b).

Figure 2 displays the mesh around the 6:1 leading edge, on which the governing equations are discretized. In (a) the elements in the upstream part of the grid are depicted, while (b) gives a close-up view of the nose region including the distribution of the GLL nodes inside the spectral elements. In the upstream region of the grid the full body is meshed, which allows for the introduction of disturbances being non-symmetric about the symmetry plane of the body. A large portion of the mesh is clipped in the lower part of the domain to reduce the computational effort. Since the base flow is independent of the spanwise direction, a two-dimensional grid is sufficient to compute it. The parameters of the mesh are listed in table 1. The number of elements in tangential direction is slightly raised in the grid around the body with the 20:1 leading edge, as its sharper nose needs a finer resolution. Note that some of the

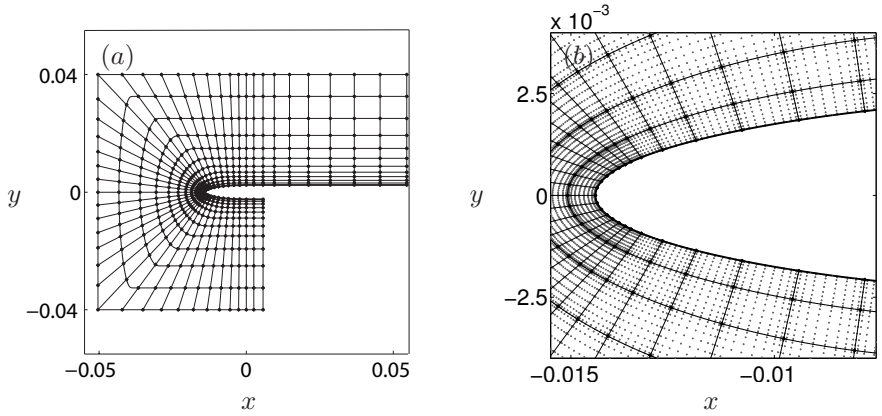

FIGURE 2. Computational grid for the leading edge with aspect ratio $a{:}b = 6$. (a) Distribution of the spectral elements in the upstream part of the body. (b) Close-up view of the nose region. Grey dots: Gauss-Lobatto-Legendre (GLL) points.

TABLE 1. Parameters of the numerical grids used to compute the two-dimensional basic an the three-dimensional unsteady flow: Size of the domain in axial, vertical and spanwise direction ($L_{ax} \times L_{vt} \times L_{sp}$), number of spectral elements in tangential, normal and spanwise direction ($n_{tg} \times n_{no} \times n_{sp}$), spectral polynomial order N and total number of degrees-of-freedom N_{tot}.

	$a{:}b$	$L_{ax} \times L_{vt} \times L_{sp}$	$n_{tg} \times n_{no} \times n_{sp}$	N	N_{tot}
Mean flow	6	0.324×0.08	69×11	9	62200
	20	0.324×0.08	72×11	9	64900
Unsteady flow	6	$0.324 \times 0.08 \times 0.036$	$69 \times 11 \times 8$	9	4540600
	20	$0.324 \times 0.08 \times 0.036$	$72 \times 11 \times 8$	9	4737700

elements in surface-tangential direction are located below the symmetry plane of the body. For the numerical grid around the blunt body with 6:1 leading edge, for example, 50 out of the 69 elements in tangential direction are located above the axis of symmetry. The polynomial order inside the elements is 9 in either directions. Thus, the number of points in tangential direction is 622 with 451 points above the symmetry plane, and 100 points are used in normal direction.

The semi-minor axis b of the elliptic leading edge, which is at the same time the half-thickness of the plate, is set to $b = 2.4{\cdot}10^{-3}$. The reference velocity U_∞ is one, and the kinematic viscosity is chosen such that the Reynolds number based on b is $Re_b = U_\infty b/\nu = 2400$, as in Lin *et al.* (1992), Buter & Reed (1994) and Wanderley & Corke (2001). The outflow boundary is located at

$Re_L = U_\infty L/\nu = 288000$, where L is the length of the body captured in the domain.

On the wall no-slip conditions are prescribed. The condition for the mean flow along the far-field boundary (inflow plane and free-stream boundary) is of Dirichlet type and is obtained from a potential-flow solution around the body thickened by the displacement thickness of the boundary layer on it. The thickness of the layer is estimated by combining a preliminary inviscid solution with a boundary-layer solver. This procedure allows for far-field boundaries located rather close to the body, while the desired zero-pressure gradient along the flat plate is still obtained. The inflow plane is 15 plate half-thicknesses ahead of the nose of the body, where the free stream is still nearly uniform and the presence of the body is hardly felt. This is seen in figure 3 showing the far-field boundary conditions for the mean velocities when the blunt obstacle with $a{:}b = 6$ is considered. The axial velocity defect on the stagnation streamline is less than 2.5% of the reference velocity U_∞, and the displacement expressed in vertical mean velocity is about $\pm 1\%$ of U_∞. Varying the inflow location revealed that the chosen position is an adequate compromise between the two intentions of obtaining inflow uniformity on the one hand and limiting the upstream domain size and thus the computational cost on the other hand. Note also that the deviance from the uniform inflow is less for the flow around the sharp body with $a{:}b = 20$. The upper and lower free-stream boundaries are 16.7 times the half-thickness away from the centerline of the body. This corresponds to a distance between the flat plate and the free-stream boundary of 12.5 outflow boundary-layer thicknesses δ_{99}^{out}. At the outflow boundaries above and below the symmetry plane a von-Neumann condition implying zero mean stress is applied to U and V.

2.3. *Perturbed flow*

The perturbed flow is computed on a three-dimensional mesh, the x-y planes of which correspond to the two-dimensional base-flow grid. In spanwise direction 8 spectral elements with a total of 73 points are used, and the width of the domain is 15 times the plate half-thickness. The three-dimensional simulations are initialized with the plane base flow, and a periodic condition is applied at the spanwise boundaries of the computational domain.

Time-dependent vortical free-stream disturbances are imposed at the inlet boundary of the domain. The study is separated into three parts by considering free-stream perturbations composed of only one vorticity component at a time, that is, the other two components of the vorticity vector $(\xi, \eta, \zeta)^T$ are put to zero. Disturbance velocities representing pure axial vorticity, for instance, can be derived from the definition of ξ and the incompressibility constraint,

$$\xi = \frac{\partial w}{\partial y} - \frac{\partial v}{\partial z} \ , \tag{4a}$$

$$0 = \frac{\partial u}{\partial x} + \frac{\partial v}{\partial y} + \frac{\partial w}{\partial z} \ . \tag{4b}$$

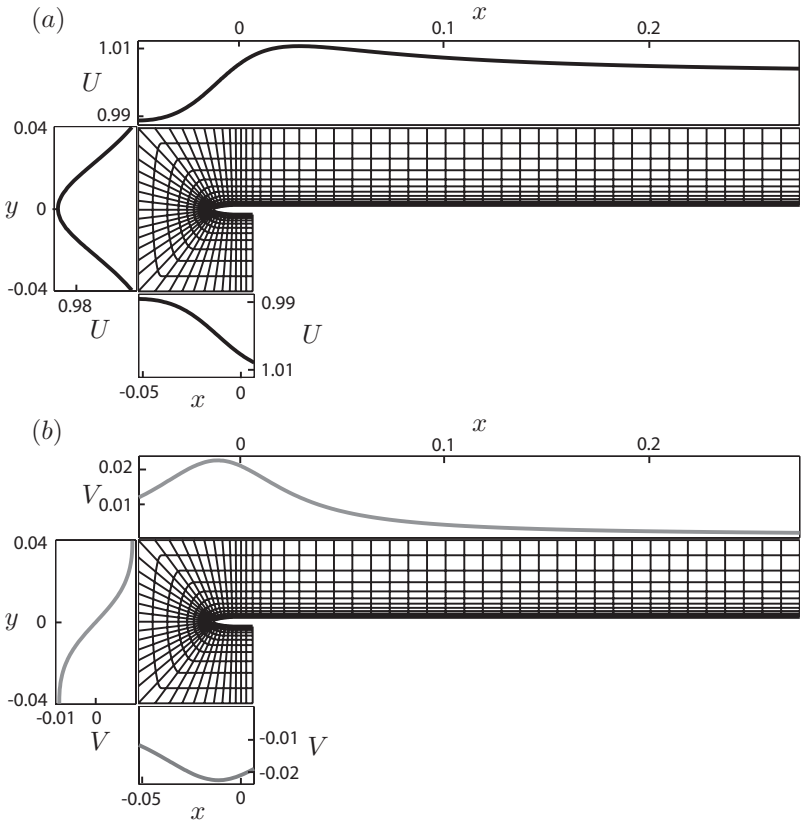

FIGURE 3. Dirichlet conditions for the mean flow at the far-field boundaries, extracted from the potential-flow solution around the blunt body (a:b = 6 with $b = 2.4 \cdot 10^{-3}$) thickened by the displacement thickness. (a) Axial and (b) vertical mean velocity.

The vorticity and velocity component pointing in the same direction (ξ and u here) evolve independently of each other in a uniform free stream. Therefore, without loss of generality, the disturbance velocity parallel to the non-zero vorticity component is set to zero in the inflow region, and the corresponding term on the right-hand side of (4b) is dropped. However, a disturbance field with one vorticity component alone is sustained only in the absence of mean shear, as is the case in the flow field far upstream of a body. Figure 3 shows, though, that the mean flow is weakly sheared at the inflow plane such that a small adjustment of the vortical disturbance to the underlying flow is expected.

Assuming spatially periodic solutions, that is, Fourier modes of the form $\phi = \hat{\phi} e^{i(\alpha x + \beta z + \gamma y)}$, where ϕ is a placeholder for the velocity respective vorticity components, system (4) can be rewritten as

$$i\hat{\xi} = \beta\hat{v} - \gamma\hat{w} \ , \tag{5a}$$

$$0 = \gamma\hat{v} + \beta\hat{w} \ . \tag{5b}$$

The velocity amplitudes $\hat{v}$ and $\hat{w}$ can therefore be expressed in terms of the streamwise vorticity $\hat{\xi}$,

$$\hat{v} = \frac{i\beta}{\beta^2 + \gamma^2}\hat{\xi} \quad \text{and} \quad \hat{w} = -\frac{i\gamma}{\beta^2 + \gamma^2}\hat{\xi} \ . \tag{6}$$

$\hat{v}$ and $\hat{w}$ are thus obtained by selecting a certain wavenumber vector $(\gamma, \beta)^T$ in the inflow plane, the size $L_y \times L_z$ of which defines the fundamental wavenumber $(\gamma_0, \beta_0)^T = 2\pi(1/L_y, 1/L_z)^T$. Here, 19 modes with spanwise wavenumbers ranging from 0 to 18 times β_0 are superposed, and the normal wavenumber is 5 times γ_0. The total disturbance is then

$$\phi = \mathrm{Re}\left\{ \sum_{j=0}^{18} \hat{\phi}_j e^{i(\alpha x + \beta_j z + 5\gamma_0 y + \theta_{r,j})} \right\} \ , \tag{7}$$

where θ_r is a random phase angle. The vorticity amplitude $\hat{\xi}$ in relation (6) can be arbitrarily chosen and is set to one here, implying that the vorticity of the 19 components in the sum of (7) is equal. The total disturbance velocities v and w in the form of (7) are scaled such that the mean fluctuation amplitude ε_v on the inflow plane, defined here as

$$\varepsilon_v = \sqrt{0.5(\overline{v^2} + \overline{w^2})} \ , \tag{8}$$

is $\varepsilon_v = 10^{-4}$. The bar in equation (8) denotes the vertical average of the spanwise root mean square of the disturbance velocities. The chordwise wavenumber α in the oscillatory term in (7) can be freely selected and is in practice replaced by the angular frequency ω via Taylor's hypothesis, assuming $U_\infty = 1$ at the inlet boundary.

The velocity amplitude functions resulting from wall-normal vorticity η plus $v = 0$ and spanwise vorticity ζ along with $w = 0$ are derived in the same way as shown above, and the expressions read

$$\hat{u} = -\frac{i\beta}{\alpha^2 + \beta^2}\hat{\eta} \quad \text{and} \quad \hat{w} = \frac{i\alpha}{\alpha^2 + \beta^2}\hat{\eta} \tag{9}$$

in the case of vertical vorticity and

$$\hat{u} = \frac{i\gamma}{\alpha^2 + \gamma^2}\hat{\zeta} \quad \text{and} \quad \hat{v} = -\frac{i\alpha}{\alpha^2 + \gamma^2}\hat{\zeta} \ , \tag{10}$$

when pure spanwise vorticity is considered. In the expression (8) for the disturbance amplitude ε_v, v and w are substituted by the respective non-zero velocity components. Again, α in the above relations is replaced by the frequency ω, herein expressed in terms of the frequency parameter $F = (\nu \cdot 10^6 / U_\infty^2)\omega$. The

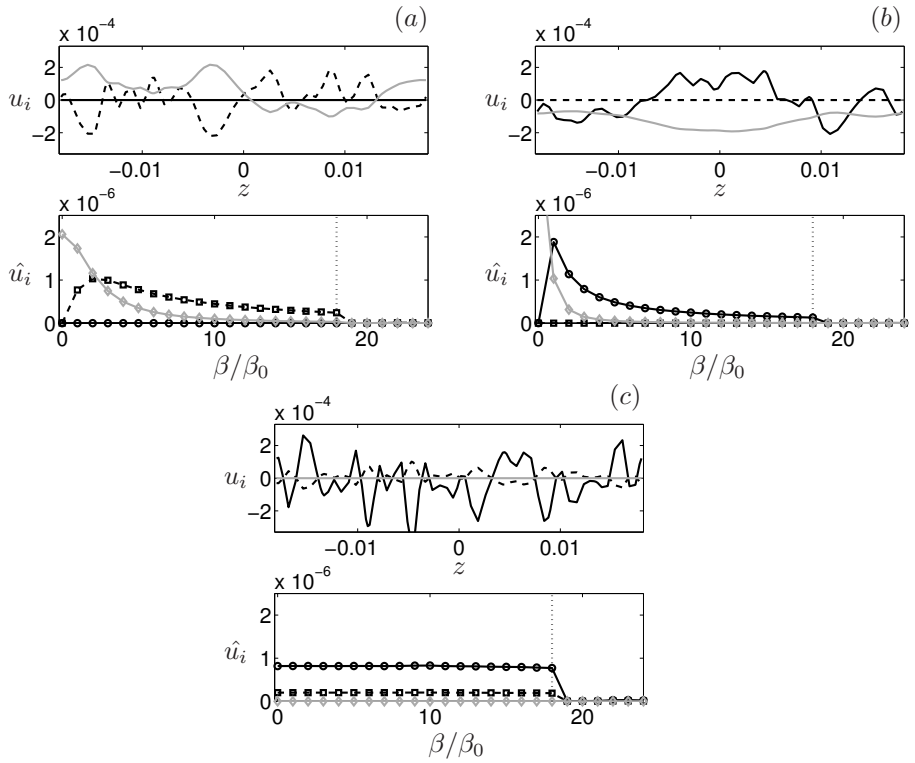

FIGURE 4. Vortical free-stream disturbances at the inflow plane with normalized frequency $F = 96$. Streamwise (——), vertical (----) and spanwise (——, grey) disturbance velocities in physical (top) and wavenumber space (bottom) corresponding to (a) axial vorticity $(\xi, 0, 0)^T$, (b) vertical vorticity $(0, \eta, 0)^T$ and (c) spanwise vorticity $(0, 0, \zeta)^T$. The curves are extracted at $y = 1.4 \cdot 10^{-2}$. The symbols in the bottom plots mark the $\beta_0 = 0$ contribution, the fundamental β_1 component and its harmonics. The dotted line shows the cut-off wavenumber.

resulting disturbance velocities ensure a divergence free incoming field and are shown in figure 4. In (a) the free-stream perturbation is characterized by axial, in (b) by vertical and in (c) by spanwise vorticity, and the normalized frequency is $F = 96$. The profiles are plotted versus the spanwise coordinate z (top) and wavenumber β (bottom) at a fixed vertical level above the symmetry plane of the plate. The representation in spectral space indicates the contribution of the components with different spanwise wavenumber to the total perturbation and follows from equations (6), (9) and (10) along with the constraint of equal vorticity in all components. Note that the individual spectral components of

TABLE 2. Parameters for the leading edge and the free-stream vortical disturbances.

a:b	6:1	20:1
Vort. comp.	$\xi,\ \eta,\ \zeta$	$\xi,\ \eta,\ \zeta$
F	16, 96	16, 96

the spanwise vortical free-stream disturbance in figure 4(c) are all at equal strength, following from the independence of (10) from β. In contrast, the axial and vertical disturbance-vorticity fields are dominated by low-wavenumber components. Further note that the mean component $\beta = 0$ is a sinusoidal function of the normal coordinate y with zero average across the vertical coordinate, i.e. the mean flow is not altered on average by the perturbation. At the vertical level chosen in figure 4 the mean contribution has its maximum.

3. Results

Results are obtained for a blunt and a sharp MSE leading edge to capture the effect of nose radius, surface curvature and the resultant pressure distribution on receptivity to free-stream vortices. Only one component of the vorticity vector $(\xi, \eta, \zeta)^T$ is not zero at a time, that is, receptivity to axial, vertical and spanwise free-stream vorticity is studied separately to isolate the single contributions. Further, the effect of angular frequency is illuminated by considering low as well as high values for the frequency parameter F. Spanwise size and resolution of the computational domain are chosen to accommodate 18 different spanwise wavelengths, of which the shortest is about 0.8 times and the longest 15 times the plate half-thickness b (0.6 times and 11.3 times the 99% boundary-layer thickness δ_{99}^{out} at the outflow plane). The vortical disturbances also contain a component with spanwise wavenumber $\beta = 0$. The vertical wavenumber γ is chosen such that the normal length scale is about 6.7 times as large as b (5 times δ_{99}^{out}). The amplitude of the free-stream perturbation is $\varepsilon_v = 10^{-4}$ such that nonlinear interaction between disturbance structures of different spanwise scales remains small. In summary, the parameter study amounts to the 12 simulations compiled in table 2.

3.1. *Basic flow*

3.1.1. *Validation of the far-field boundary conditions*

In order to validate the method described in subsection 3.1 to compute the Dirichlet boundary conditions for the basic flow we have chosen to compare the pressure distribution obtained through two-dimensional simulations with the present SEM code with results published in Wanderley & Corke (2001). There, a 20:1 and a 40:1 MSE leading edge are considered. Figure 5 depicts the chordwise distribution of the pressure coefficient c_p. As seen from the plot, the desired constant pressure is obtained downstream in the flat-plate region of

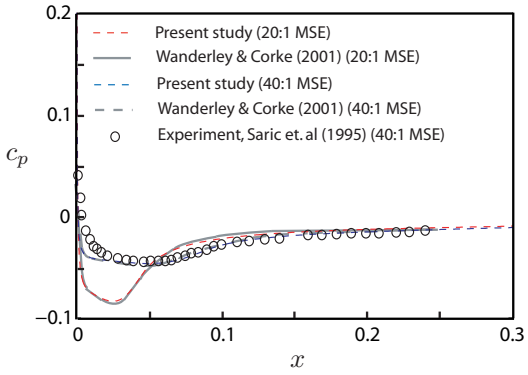

FIGURE 5. Chordwise distribution of the pressure coefficient along a body with 20:1 and with 40:1 leading edge. Comparison with results published in Wanderley & Corke (2001).

the body, and good agreement between the c_p-curves calculated here and those shown in Wanderley & Corke (2001) is observed for both leading edges.

3.1.2. *Mean flow*

Figure 6 gives a characterization of the mean flow around the body with blunt (6:1) and sharp leading edge (20:1) in comparison with Blasius boundary-layer flow. In (a) the pressure coefficient c_p is plotted versus the streamwise coordinate x. The juncture with the plate is located at $x = 0$ for both bodies. The suction peak on the blunt leading edge is more distinct and located nearer the junction than on the sharp one, and the adverse pressure gradient is stronger. Therefore, the constant pressure distribution expected in the flat plate region is attained further downstream on the body with blunt nose. Figure 6(b) shows the mean wall vorticity ζ_w along the surface coordinate s. As expected, the ζ_w distribution according to the Blasius approximation is reached further upstream on the plate with slender leading edge. In (c) the boundary-layer displacement thickness δ^* is displayed versus s. While δ^* follows the $\sqrt{s}$ distribution typical for the zero pressure-gradient boundary layer downstream of the junction, it increases more rapidly on the curved part of the surface than it would do in Blasius flow. In particular on the blunt leading edge the boundary layer grows faster in the region of flow deceleration.

3.2. *Unsteady flow*

Unsteady flow caused by vortical free-stream perturbations is considered. First, a preceding study on a two-dimensional grid involving spanwise free-stream vortices is carried out to estimate the significance of Tollmien-Schlichting (TS) instability. Subsequently, results from three-dimensional simulations characterizing the behavior of the vortices in the free stream are presented to show how the perturbation field prescribed at the inflow plane changes due to the

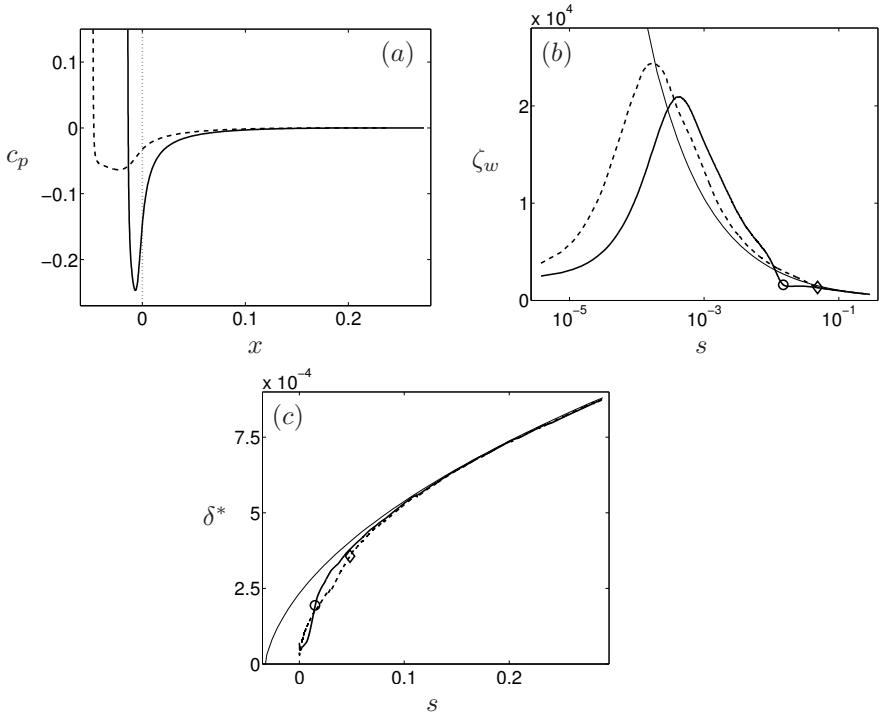

FIGURE 6. Comparison of the mean flow past the blunt (——, a:b=6) and the sharp leading edge (----, a:b=20) with the Blasius boundary layer (——, thin). (a) Pressure coefficient versus streamwise coordinate. The juncture with the plate is located at $x = 0$, as indicated by the dotted line. (b) Wall vorticity versus surface coordinate. The juncture is marked with symbols (○, a:b=6; ◇, a:b=20). (c) Displacement thickness. The symbols in (c) correspond to those in (b).

presence of the body as the vortices are convected downstream. The knowledge of the downstream variation of the free-stream disturbance is crucial, since free-stream modes are a non-localized disturbance source acting on the entire boundary layer. In the second part, the response of the layer to the different vortical components of the free-stream disturbance is investigated. Receptivity to perturbations of different angular frequency is discussed, and the effect of leading-edge bluntness on receptivity to free-stream vorticity is identified.

3.2.1. *TS instability*

Simulations on a two-dimensional domain similar to those in Buter & Reed (1994) have been performed. The grid resembles that for the mean flow listed in table 1 except for the number of elements in tangential direction, n_{tg}, which

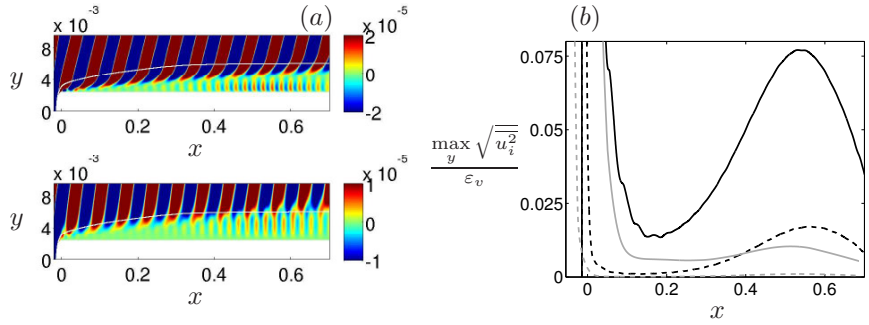

FIGURE 7. (a) Boundary-layer response to spanwise free-stream vorticity with $\beta = 0$, $F = 96$ and $\varepsilon_v = 10^{-4}$. Instantaneous disturbance velocities u (top) and v (bottom) in the x-y plane. Leading edge with aspect ratio $a{:}b = 6$. (b) Wall-normal maximum of the r.m.s. of u (——) and v (----) normalized by ε_v for the blunt ($a{:}b = 6$, black lines) and the sharp leading edge ($a{:}b = 20$, grey lines).

has been increased to 125 for the blunt and 136 for the sharp leading edge. Therefore, the outflow Reynolds number is $Re_L = 7.7 \cdot 10^5$. Spanwise free-stream vorticity with the same vertical wavenumber as that in figure 4(c) is considered, but only the spanwise wavenumber $\beta = 0$ is included. The amplitude of the free-stream disturbance is $\varepsilon_v = 10^{-4}$ and the frequency is $F = 96$. Figure 7 shows the response of the boundary layer to this kind of forcing. In (a) planes of streamwise and vertical disturbance velocity u and v are shown for the blunt leading edge, $a{:}b = 6$, and in (b) the r.m.s. of u and v, normalized by the forcing amplitude, is displayed for both leading edges. Both plots show that TS instability is observed at $F = 96$ and that the entire unstable region is captured inside the domain. In figure 7(b) it is apparent that the amplitude of the TS waves is more than three times larger for the blunt leading edge than for the sharp one. However, the normalized amplitude achieves a maximum of only 7.5% of the amplitude of the oncoming free-stream disturbance, i.e. TS instability is weak even on the plate with blunt nose.

3.2.2. *Free stream*

In the following results from three-dimensional simulations with free-stream perturbations like those in figure 4 are presented. Figure 8 illustrates the downstream evolution of the vortical free-stream disturbances at two vertical levels: near the boundary-layer edge and far above it. Plots (a), (b) and (c) show the root mean square (r.m.s.) in time and spanwise direction of the disturbance velocities due to axial, vertical and spanwise free-stream vorticity at a frequency of $F = 16$. In (d), (e) and (f) the evolution of the velocities is shown for $F = 96$. It is apparent in particular in (e) and (f) for the high frequency that the zero velocity component at the inflow plane is rapidly forced when the

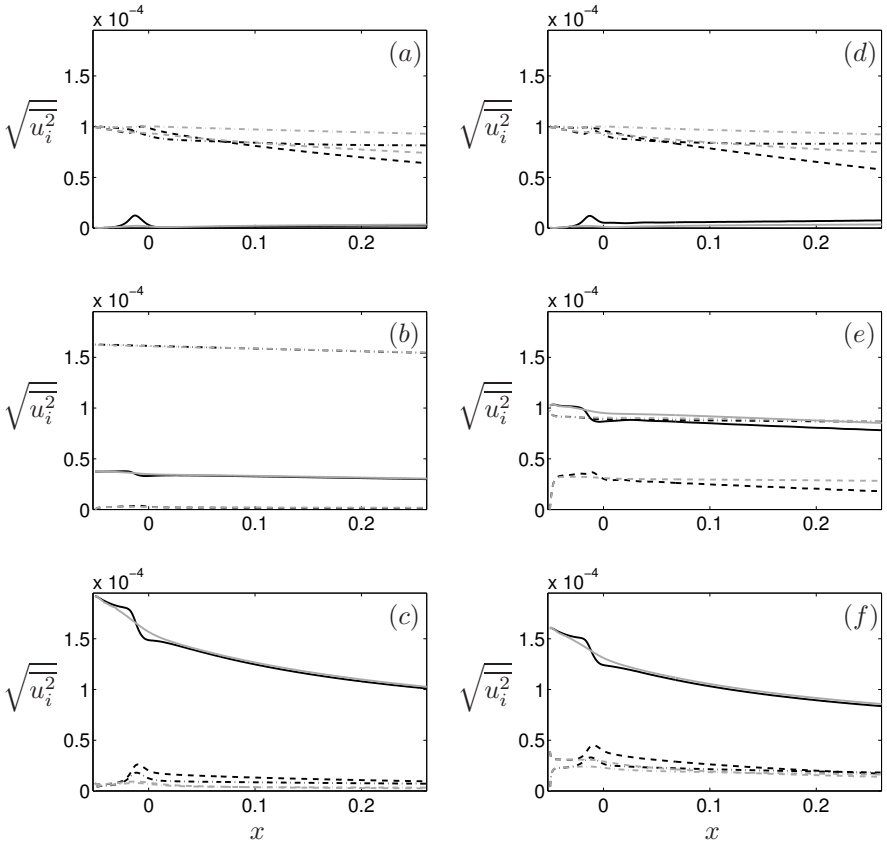

FIGURE 8. Downstream evolution of the free-stream perturbation. The disturbance amplitude at the inlet is $\varepsilon_v = 10^{-4}$. The r.m.s. in time and spanwise direction of the three disturbance velocities u (——), v (----) and w (-·-·-) is displayed at two vertical levels: near the boundary-layer edge at $y = 6.6 \cdot 10^{-3}$ ($1.3\delta_{99}^{out}$, thick black curves) and far in the free stream at $y = 2.4 \cdot 10^{-2}$ ($6.8\delta_{99}^{out}$, thin grey lines), where δ_{99}^{out} is the boundary-layer thickness at the outflow. (a)–(c) $F = 16$; (d)–(f) $F = 96$. (a) and (d) Axial free-stream vorticity; (b) and (e) vertical free-stream vorticity; (c) and (f) spanwise free-stream vorticity.

flow approaches the body. Two regions of adjustment are observed: an initial adaptation at the inflow plane related to the tilting of the incoming vorticity by the curved streamlines around the obstacle and an adjustment due to the attachment of the flow to the body, apparent as a "jump" in the curves. In the

case of vorticity $(0, \eta, 0)^T$ in plot (b) and (e) the mean shear leads to a tilting of the vertical vorticity parcels around the z axis such that the streamwise disturbance velocity decreases in favor of the normal component. In (c) and (f) it is seen that the spanwise vortex parcels are tilted around the x axis, which leads to an increase of the spanwise disturbance account of the normal velocity component. This mechanism is caused by the velocity fluctuations rather than the mean flow. No rapid forcing of the zero u component at the inflow plane is in contrast seen in figures 8(a) and (d) since the mean shear is not able to tilt the axial vortex tubes. Moreover, the figures show the expected downstream decay of the disturbance velocities. The spanwise vortical free-stream perturbation displayed in (c) – especially its streamwise velocity component – suffers from the strongest decay, as it also contains significant energy at the smallest scales, compare with figure 4(c).

In summary, figure 8 shows that the mean flow and the fluctuations correct the free-stream perturbation prescribed at the inflow plane by tilting and stretching the vortex tubes. The vortices with short streamwise scale at $F = 96$ are more sensitive to these processes than those with large streamwise length scale at $F = 16$. The adjustment is fast such that the free-stream disturbance is physically correct when it impinges on the obstacle. Tilting and stretching of free-stream vortices is generally observed in flows around aerodynamic bodies, and these processes will have an impact on the receptivity of the boundary layer. An example is a field of homogeneous isotropic turbulence generated by a turbulence grid in a wind tunnel, which will become anisotropic as it approaches the aerodynamic model in the test section.

3.2.3. *Boundary layer*

Figure 9 provides an illustration of the boundary-layer response to a low-frequency free-stream disturbance with axial vorticity at $F = 16$ – (a) to (c) – and to a high-frequency free-stream perturbation of spanwise vorticity at $F = 96$ – (d) to (f). As shown in figure 4 the axial free-stream vortical disturbance is dominated by large velocity structures, whereas in the spanwise vorticity field, the smallest prescribed wavelengths are also visible. The length-scale distribution in the free stream is enforced around the nose of the body, as seen in figure 9(a) and (d). However, further downstream where the boundary layer forms, the disturbance environment is characterized by smaller spanwise scales than those in the attachment region in (a), whereas the forced scales in (d) are sustained. The free-stream perturbation enforces also a streamwise length scale upon the flow inside the boundary layer, see figures (b) and (e). The elongated low-frequency streamwise disturbances in (b) due to axial free-stream vorticity persist inside the entire layer and grow in amplitude downstream. The structures in (e) are, by contrast, only strong in the curved part of the body while decaying in the flat-plate region. Clearly, the strength of the boundary-layer response to low-frequency axial vorticity is significantly larger than that to high-frequency spanwise vortical modes. Figures 9(c) and

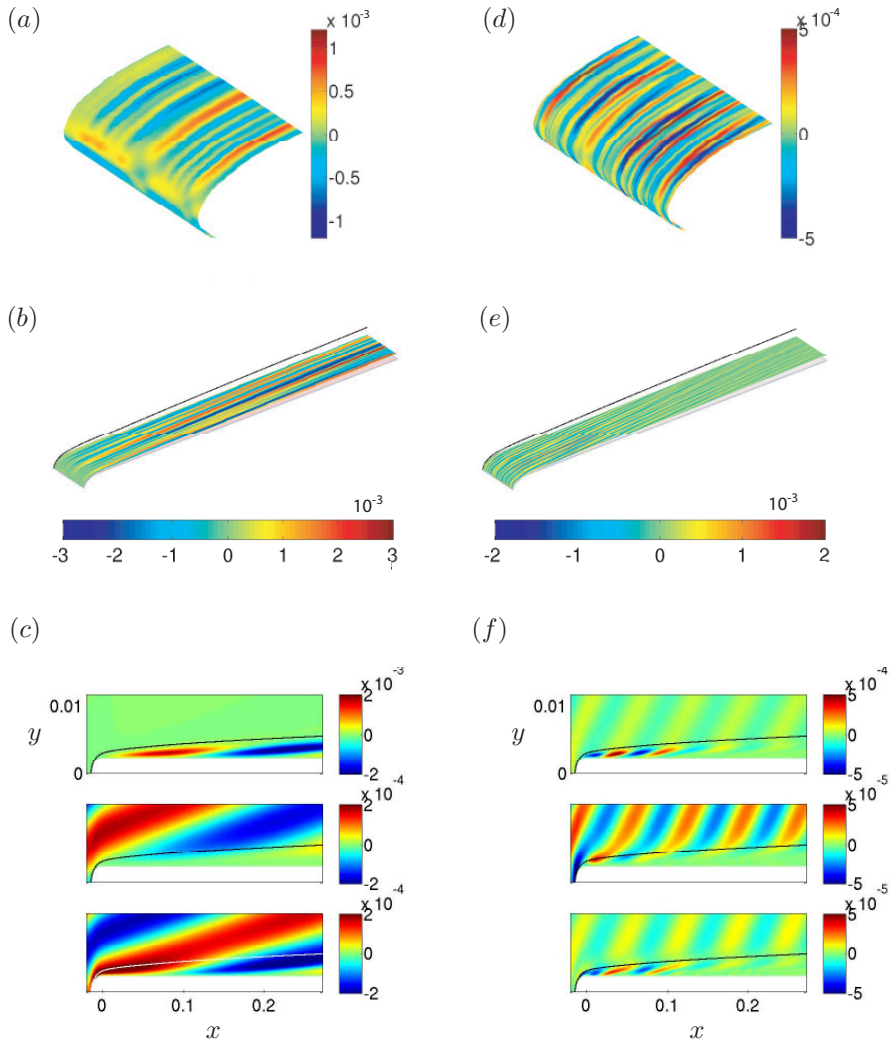

FIGURE 9. Boundary-layer response to vortical free-stream perturbations with axial vorticity at a frequency of $F = 16$, (a)–(c), and spanwise vorticity at $F = 96$, (d)–(f). The instantaneous streamwise disturbance velocity is shown; in (c) and (f) the vertical and spanwise components are also included. Plots (a) and (d) display the region around the nose of the body, (b) and (e) illustrate the maximum disturbance levels inside the boundary layer and (c) and (f) depict the location of the dominant axial, vertical and spanwise disturbance structures on the x-y plane at $z = 0$.

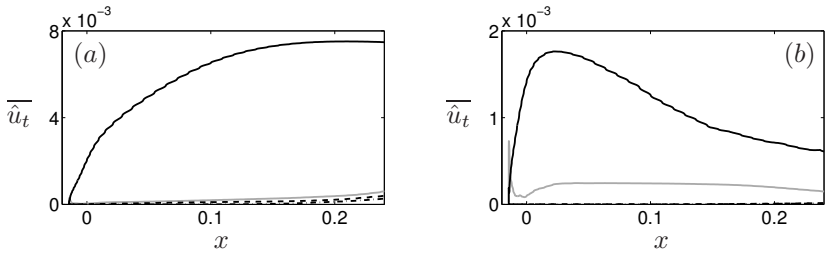

FIGURE 10. Downstream evolution of the boundary-layer disturbance excited by axial free-stream vorticity with amplitude $\varepsilon_v = 10^{-4}$ and frequency parameter (a) $F = 16$ and (b) $F = 96$. The spanwise averaged temporal Fourier transform of the streamwise disturbance u is shown. The development of disturbance components with different frequencies is plotted separately: Steady disturbance, $F_0 = 0$ (——, grey); fundamental component, $F_1 = F$ (——, black); first harmonic, $F_2 = 2F$ (----); second harmonic, $F_3 = 3F$ (-·-·-). The leading edge with aspect ratio $a{:}b = 6$ is considered.

(f) illustrate the matching between the axial size of the boundary-layer disturbance and the streamwise length scale of the free-stream disturbance. It is also seen that the boundary-layer disturbance is dominated by the stream- and the spanwise component, whereas the vertical fluctuations are hardly present. The relevance of low-frequency spanwise disturbance velocity for streak formation has been pointed out by Leib *et al.* (1999). As mentioned above, the characteristic amplitude ε_v of the free-stream disturbances is small – $\varepsilon_v = 10^{-4}$ – to limit nonlinear effects. This is examined in figure 10, showing to which extent the forcing frequency F and the frequencies $F_0 = 0$, $F_2 = 2F$ and $F_3 = 3F$ due to nonlinear interaction are present in the spectrum of the boundary-layer disturbance. The curves represent the temporal Fourier transform of the streamwise disturbance velocity, averaged in spanwise direction. Plot (a) shows the results for $F = 16$ and plot (b) those for $F = 96$. Figure (a) reveals that the boundary-layer response to low-frequency axial free-stream vortices with $F = 16$ is clearly dominated by the component with the fundamental forcing frequency F. The contributions at zero frequency and the higher harmonics attain in contrast only small amplitudes. At $F = 96$, plot (b), the disturbance amplitudes are in general lower than at $F = 16$ and they decay downstream. The fundamental frequency component is still the strongest, but the relative importance of the steady disturbance has increased to some 20% of the total disturbance, whereas the higher harmonics are negligible. It can be concluded that nonlinear effects are negligible at low frequency and moderate at high frequency

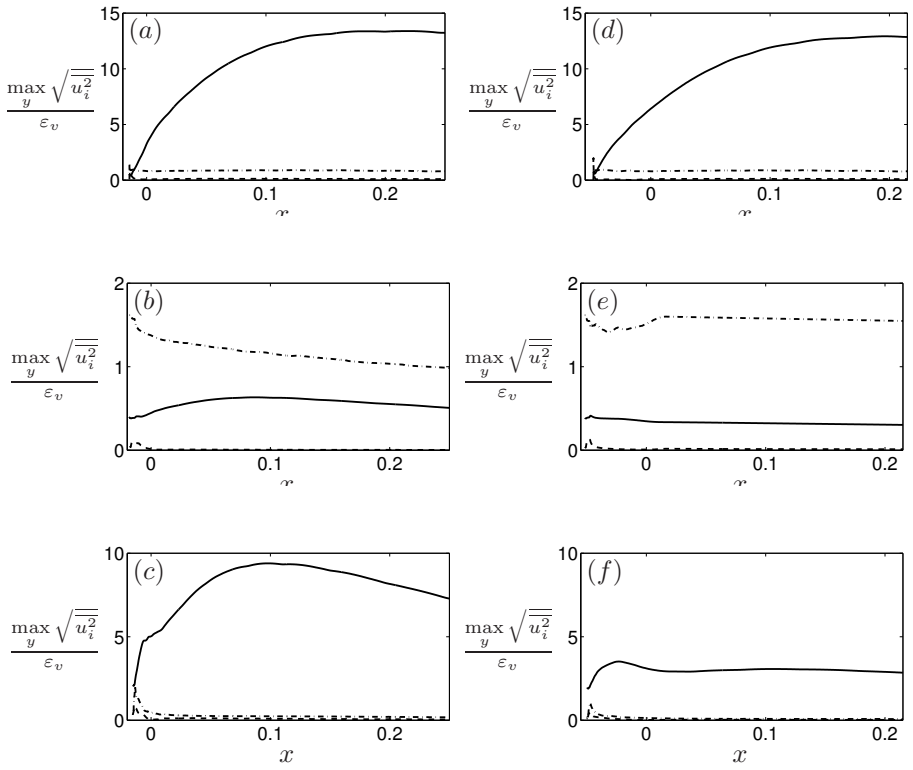

FIGURE 11. Downstream evolution of the boundary-layer disturbance excited by free-stream vorticity with amplitude $\varepsilon_v = 10^{-4}$ and frequency parameter $F = 16$. The wall-normal maximum of the r.m.s. in time and spanwise direction of the disturbance velocities u (——), v (----) and w (-·-·-) inside the boundary layer is displayed. Two leading edges with different aspect ratio a:b are considered, and the flow is exposed to three different vortical free-stream disturbances $(\xi, \eta, \zeta)^T$. (a) a:$b = 6$, $(\xi, 0, 0)^T$; (b) a:$b = 6$, $(0, \eta, 0)^T$; (c) a:$b = 6$, $(0, 0, \zeta)^T$; (d) a:$b = 20$, $(\xi, 0, 0)^T$; (e) a:$b = 20$, $(0, \eta, 0)^T$ and (f) a:$b = 20$, $(0, 0, \zeta)^T$.

for a free-stream disturbance amplitude of $\varepsilon_v = 10^{-4}$. They become less relevant when the external perturbation is dominated by vertical and spanwise vorticity (not shown here). Therefore, the subsequent analysis is restricted to the dominant disturbance components with the fundamental frequency. The observations from figure 9 are quantified in figures 11 and 12 by considering the

wall-normal maximum of the r.m.s. of the three disturbance components u, v and w in the boundary layer. The r.m.s values are computed by averaging in time and in spanwise direction, and they are normalized with the amplitude ε_v of the free-stream disturbance. The plots show the response of the boundary layer on the plates with blunt and sharp leading edge to axial, vertical and spanwise vortical free-stream modes. The frequency parameter in figure 11 is $F = 16$ and in 12 $F = 96$. Clearly from figure 11, the free-stream disturbance dominated by axial vortices is most efficient in triggering boundary-layer instability. The disturbance exhibits amplification proportional to the growth of the boundary layer in the upstream region and levels out downstream at a value being about 13 times larger than the amplitude of the oncoming free-stream fluctuations. Comparison between figure 11(a) and (d) reveals that the disturbance amplitude is slightly larger in the boundary layer on the bluff body and that the upstream amplification rate in the curved region is somewhat higher. However, the effect of leading-edge bluntness on receptivity to axial vorticity is rather moderate. The effect of geometry is, by contrast, larger if the free-stream perturbation is dominated by vertical and spanwise vortices. This is concluded from comparing figure 11(b) and (c) with (e) and (f). In particular the free-stream fluctuations dominated by spanwise vorticity are able to trigger strong upstream transient growth, which is most notable on the plate with the blunt leading edge in plot (c). The disturbance obtained is, however, not the same as in figure (a), and its amplitude diminishes downstream. Plot (f) shows a weaker disturbance with different amplification in the slender-body boundary layer. Differences between the response of the layers around the 6:1 and 20:1 leading edge are also identified in figures 11(b) and (e). These plots reveal that free-stream fluctuations dominated by vertical vortices are significantly less efficient in exciting disturbances in the boundary layer than spanwise and in particular axial vortices. The obtained amplitudes are weak and the disturbance is dominated by the spanwise velocity component, whereas the streamwise velocity indicating boundary-layer streaks remains small. Figure 12 displays the boundary-layer response to forcing at higher frequency, $F = 96$. The instabilities inside the layer are significantly weaker than those triggered by low-frequency free-stream perturbations at $F = 16$ except for the case of vertical free-stream vorticity shown in (b) and (e). Strong transient amplification is seen in the case of spanwise free-stream vorticity in figures 12(c) and (f), but the disturbance dies out further downstream. Comparing the two plots reveals again that upstream transient growth is enhanced by leading-edge bluntness.

To summarize the results in figure 11 and 12, the downstream disturbance amplitude of the streamwise velocity in the boundary layer is maximum when axial free-stream vortices act on the layer. Spanwise free-stream vorticity is able to trigger strong upstream transient growth, while the disturbance amplitude decays downstream. The boundary layer is clearly least receptive to vertical free-stream vortices. Finally, we conclude that the disturbance intensity inside the boundary layer is considerably higher at $F = 16$ than at $F = 96$.

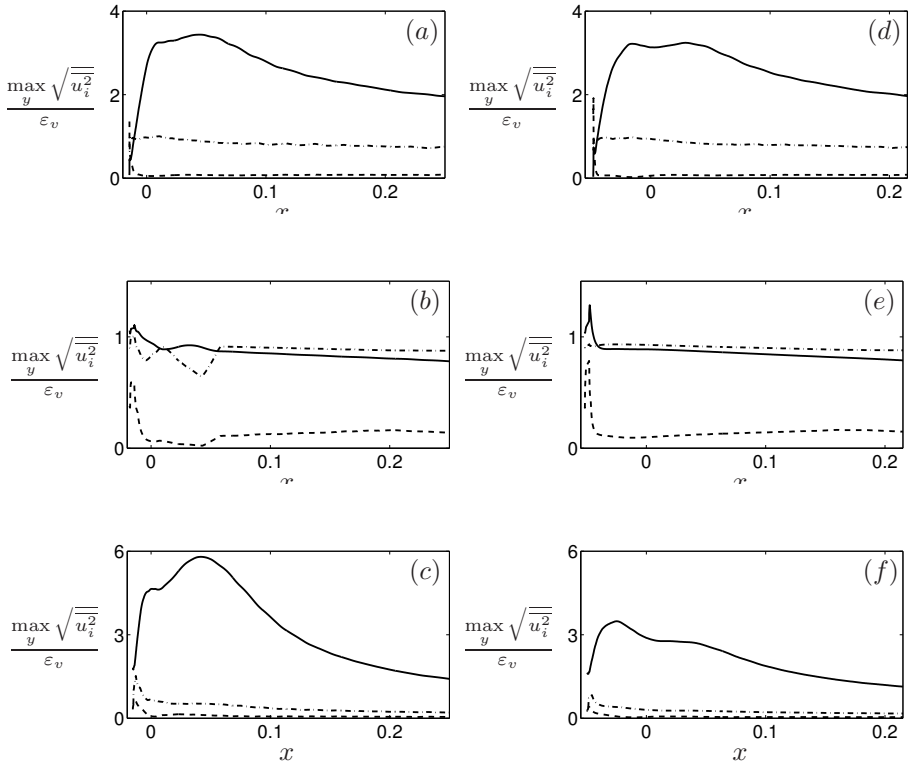

FIGURE 12. Downstream evolution of the boundary-layer disturbance excited by free-stream vorticity with amplitude $\varepsilon_v = 10^{-4}$ and frequency parameter $F = 96$. The wall-normal maximum of the temporal-spanwise r.m.s. of the three disturbance velocities u (——), v (----) and w (-·-·-) inside the boundary layer is displayed. Two leading edges with different aspect ratio a:b are considered, and the flow is exposed to three different vortical free-stream disturbances $(\xi, \eta, \zeta)^T$. (a) $a{:}b = 6$, $(\xi, 0, 0)^T$; (b) $a{:}b = 6$, $(0, \eta, 0)^T$; (c) $a{:}b = 6$, $(0, 0, \zeta)^T$; (d) $a{:}b = 20$, $(\xi, 0, 0)^T$; (e) $a{:}b = 20$, $(0, \eta, 0)^T$ and (f) $a{:}b = 20$, $(0, 0, \zeta)^T$.

To investigate the dominant transverse length scales of the boundary-layer disturbance, the spectral composition $\hat{u}_{tz}$ of the streamwise velocity signals with the fundamental frequency is considered. $\hat{u}_{tz}$ is obtained through Fourier transformation in time and spanwise direction. Figure 13 depicts the results obtained when free-stream vorticity with $F = 16$ is considered. The spanwise

wavenumber composition is shown at two chordwise positions, x_1 and x_2, where x_1 is located at a distance of 0.048 and x_2 of 0.248 length units downstream of the tip of the plate. For the sharp body, $a{:}b = 20$, x_1 corresponds to the junction between the leading-edge region and the flat plate, whereas x_1 is located slightly downstream of the junction in the case of the blunt leading edge, $a{:}b = 6$. Figures 13(a) and (d) show that the peak in the curves moves to slightly higher wavenumbers from location x_1 to x_2, where it is found at $\beta_4 = 4\beta_0$. This corresponds to a wavelength of $\lambda_4 = 9 \cdot 10^{-3}$, i.e. about three times the boundary-layer thickness $\delta_{99}(x_2)$. As seen before, the influence of the leading-edge geometry is small in a perturbation environment dominated by axial free-stream vorticity. The differences in amplitude become larger when vertical free-stream vortices are considered. The blunt leading edge, plot (b), enhances the boundary-layer response to vertical vortices as compared with the sharp nose, plot (e). In both cases, the fundamental wavenumber β_1 dominates at x_1, whereas two peaks at $\beta_3 = 3\beta_1$ at $\beta_9 = 9\beta_1$ are identified downstream at x_2. The amplitudes are, however, irrelevant in comparison with those in figures 13(a) and (d). In the case of spanwise free-stream vorticity the peak at x_2 is obtained at $\beta_7 = 7\beta_1$, which is about 1.5 times $\delta_{99}(x_2)$.

Figure 14 reveals that the amplitude peaks are obtained at the same spanwise wavenumbers for $F = 96$ as in the low-frequency environment, $F = 16$, when axial and spanwise free-stream vortices are considered. In the former case, the most energetic transverse scales are again about 3 times as large as the downstream thickness $\delta_{99}(x_2)$, and in the latter case they are circa 1.5 times $\delta_{99}(x_2)$. The longitudinal scale is, however, shorter at $F = 96$ and the obtained streaks experience attenuation from x_1 to x_2 instead of amplification. The forced response due to vertical free-stream vorticity, plots (b) and (e), dies out rapidly, and no dominant wavenumber can be singled out. This type of vortical free-stream disturbance is thus unimportant at low as well as high frequencies. Finally, note that the component $(F, \beta = 0)$ is very weak in all plots in figure 13 and 14, that is, TS-instability is difficult to trigger through the weak vortical disturbances under consideration. The free-stream vorticity amplitude is $\varepsilon_v = 10^{-4}$ here, and the disturbance energy is distributed among 19 components with different spanwise wavenumber. The contribution at $\beta = 0$ is therefore too weak to excite TS waves with noteworthy amplitudes.

3.2.4. *Nonlinear effects*

Figure 10(b) suggests that disturbance components at frequencies other than the fundamental forcing frequency become detectable already at low amplitudes of the high-frequency forcing. In particular a steady disturbance is visible, entering at second order through interaction between fundamental-frequency instabilities. The relevance of nonlinear effects at high frequencies has been pointed out by Leib *et al.* (1999) who present a theoretical study on laminar boundary layers subject to vortical disturbances. They attribute

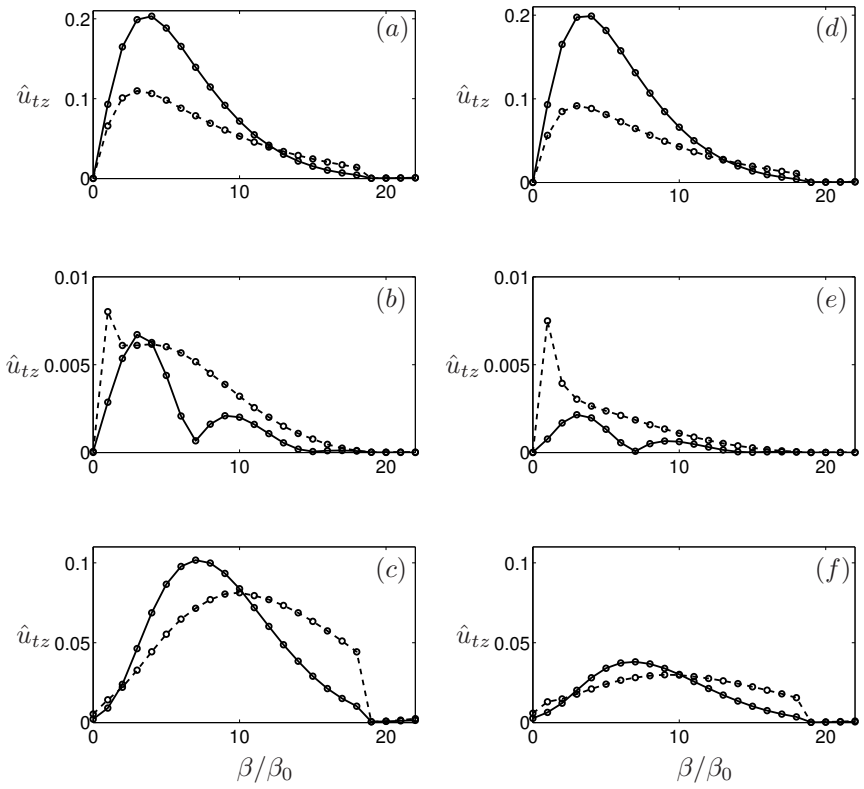

FIGURE 13. Fourier transform in time and spanwise direction of the streamwise disturbance velocity versus the spanwise wavenumber, plotted at two different streamwise locations x_1 (----, 0.048 length units downstream of the nose tip of the body) and x_2 (——, 0.248 units downstream of the nose). The frequency of the free-stream vorticity is $F = 16$. Two leading edges with different aspect ratio a:b and three different vortical free-stream disturbances $(\xi, \eta, \zeta)^T$ are considered. (a) a:$b = 6$, $(\xi, 0, 0)^T$; (b) a:$b = 6$, $(0, \eta, 0)^T$; (c) a:$b = 6$, $(0, 0, \zeta)^T$; (d) a:$b = 20$, $(\xi, 0, 0)^T$; (e) a:$b = 20$, $(0, \eta, 0)^T$; (f) a:$b = 20$, $(0, 0, \zeta)^T$.

the downstream increasing discrepancy between their results and experimentally obtained disturbance amplitudes to the high-frequency components of the disturbance and suggest nonlinear effects to come into play in a quasi-steady manner. Here, the case in figure 10(b) is reconsidered ($F = 96$); however, the amplitude of the axial free-stream vorticity is 20 times larger than before, i.e.

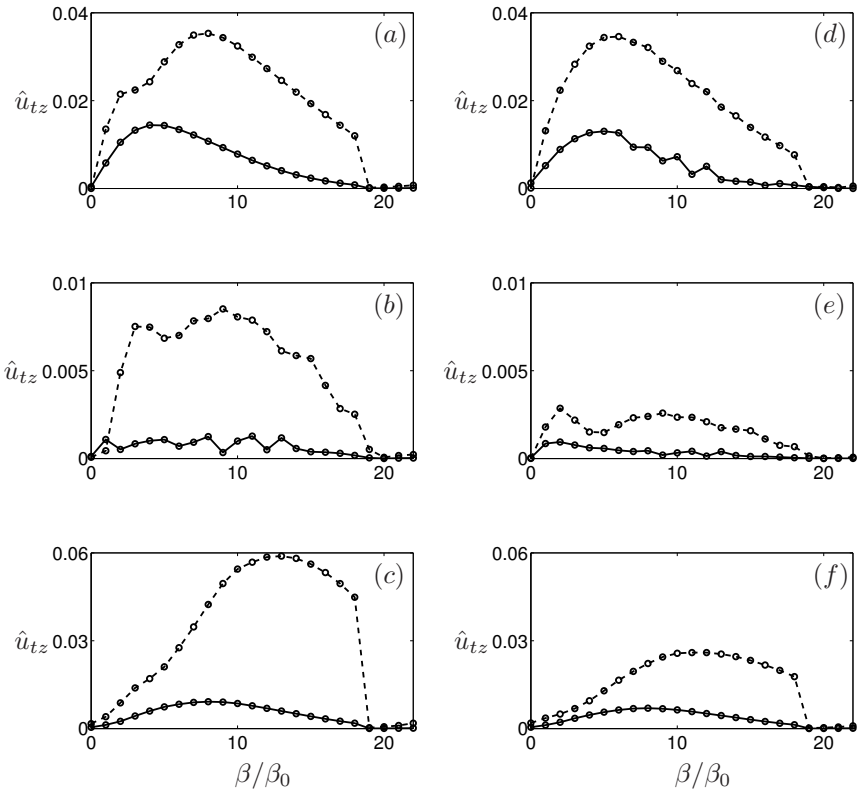

FIGURE 14. Fourier transform in time and spanwise direction of the streamwise disturbance velocity versus the spanwise wavenumber, plotted at two different streamwise locations x_1 (----) and x_2 (——), see the caption of figure 13. The frequency of the free-stream vorticity is $F = 96$. (a)–(f) are explained in the caption of figure13.

$\varepsilon_v = 2 \cdot 10^{-3}$. Figure 15(a) shows the boundary-layer response to such kind of forcing. The maximum r.m.s. in streamwise velocity u normalized by ε_v is displayed versus the chordwise coordinate x. Upstream transient behavior is followed by downstream amplification being nearly linear in x. This suggests the competition between two growth mechanisms, as clarified in figure 15(b): The upstream transient growth is caused by a directly forced instability at $F = 96$, whereas the downstream amplification is in a steady component, $F = 0$, which outweighs the amplitude of the directly forced contribution. It can be concluded that nonlinear interaction between individual disturbance

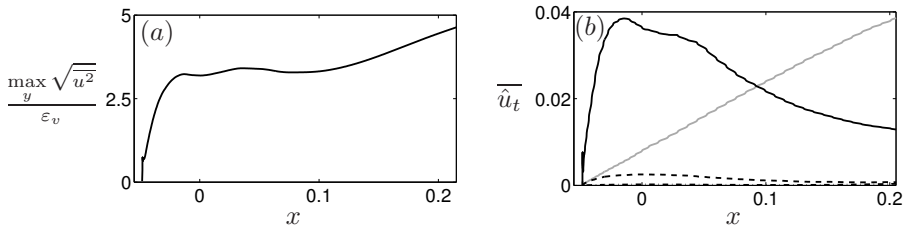

FIGURE 15. Downstream evolution of the boundary-layer disturbance excited by axial free-stream vorticity with amplitude $\varepsilon_v = 2 \cdot 10^{-3}$ and frequency parameter $F = 96$. In (a) the r.m.s. in time and spanwise direction of the streamwise disturbance u is depicted. The spanwise averaged temporal Fourier transform of u is considered in (b), showing the development of disturbance components with different frequencies is plotted separately: Steady disturbance, $F_0 = 0$ (——, grey); fundamental component, $F_1 = F$ (——, black); first harmonic, $F_2 = 2F$ (----); second harmonic, $F_3 = 3F$ (-·-·-). The leading edge is at aspect ratio a:$b = 20$.

components is relevant for the free-stream disturbance of still low intensity considered here ($\varepsilon_v = 0.2\%$ of U_∞). Nonlinearity becomes manifest mainly in the zero-frequency component generated in a high-frequency vortical perturbation environment. Nonlinear interaction will be the object of future investigations.

4. Conclusions

A study of the response of the boundary layer on a flat plate with elliptic leading edge to vortical free-stream disturbances is herein presented. The effect of leading-edge geometry is included in the investigation by considering a blunt and a sharp elliptic leading edge with aspect ratio 6:1 and 20:1. Simplified models for the vortical free-stream fluctuations are applied by setting two of the three vorticity components to zero. This allows us to single out the receptivity of the flow to axial, vertical and spanwise free-stream vortices. A free-stream perturbation field with zero divergence is obtained by putting the disturbance velocity parallel to the free-stream vorticity to zero. On approaching the obstacle the disturbance field is distorted by mean shear and fluctuations. This results in the forcing of vorticity and velocity in the components being initially zero at the inflow plane.

Results can be summarized as follows: The boundary layer is most receptive to axial free-stream vortices with low frequency which generate non-modal instability in the form of long streaks inside the layer. The streamwise disturbance velocity is clearly dominant. This is in line with earlier experimental

findings and with numerical studies disregarding the leading edge. It has been found here that the disturbance amplification is slightly enhanced when the sharp leading edge is replaced by the blunt one, which is due to the more distinct region of adverse pressure gradient on the bluff body. However, the effect of leading-edge bluntness remains small in the presence of axial vortices. This is in contrast with the response of the boundary layer to spanwise free-stream vorticity: The latter is able to excite non-modal instability in the curved part of the body. This becomes manifest in significant upstream transient growth, being clearly stronger in the boundary layer on the plate with blunt leading edge. This finding is again ascribed to the stronger adverse pressure gradient and is in line with results in Levin & Henningson (2003), for example. Little receptivity to vertical free-stream vortices has been observed here, and it is concluded that the vertical vorticity component is least relevant for receptivity to free-stream turbulence. The plate considered here is, however, rather thin – its thickness is comparable with the boundary-layer thickness at the outflow. A bluffer obstacle may be more efficient in tilting the vertical vorticity parcels, as suggested in Goldstein & Wundrow (1998), which are then wrapped around the leading edge and force axial vorticity.

The boundary layer is less receptive to free-stream vortices at high frequency. Non-modal instabilities at lower amplitudes are obtained inside the layer which decay downstream. However, at large enough amplitudes (0.2% here) high-frequency axial vortices are efficient in generating a steady nonlinear contribution to the disturbance, which is rapidly intensified downstream and dominates the boundary-layer disturbance there. Nonetheless, the total disturbance amplitude remains considerably lower than that of the low-frequency streaks. High-frequency spanwise vorticity triggers again upstream transient growth, but on a lower amplitude level than low-frequency spanwise free-stream vortices.

Tollmien-Schlichting (TS) instability has been observed at rather low amplitudes in two-dimensional simulations with spanwise vortices in the free-stream. Leading-edge bluntness enhances receptivity for TS waves. In the three-dimensional simulations the TS modes have been found to be negligible even in the boundary layer over the plate with blunt leading edge, although the high-frequency spanwise free-stream vorticity also contains a component with $\beta = 0$. It is, however, weak such that the TS mechanism cannot compete with the non-modal instability.

The authors wish to acknowledge Dr. Paul Fischer for providing the simulation code and Dr. Ardeshir Hanifi for his support in the generation of the boundary conditions for the mean flow.

This research is funded by VR (The Swedish Research Council). SNIC computing facilities located at the Center for Parallel Computers (PDC), KTH, and the National Supercomputer Centre, Linköpings universitet, have been used for the computations.

References

Bertolotti, F. P. & Kendall, J.M. 1997 Response of the Blasius Boundary Layer to Controlled Free-Stream Vortices of Axial Form. *AIAA Paper* (97-2018).

Brandt, L., Schlatter, P. & Henningson, D. S. 2004 Transition in boundary layers subject to free-stream turbulence. *J. Fluid Mech.* **517**, 167–198.

Buter, T. A. & Reed, H. L. 1994 Boundary layer receptivity to free-stream vorticity. *Phys. Fluids* **6 (10)**, 3368–3379.

Choudhari, M. & Streett, C. L. 1992 A finite Reynolds number approach for the prediction of boundary layer receptivity in localized regions. *Phys. Fluids A* **4**.

Crouch, J. D. 1992 Localized receptivity of boundary layers. *Phys. Fluids A* **4 (7)**, 1408–1414.

Fischer, P. F. 1997 An overlapping Schwarz method for spectral element solution of the incompressible Navier-Stokes equations. *J. Comp. Phys.* **133**, 84–101.

Fischer, P. F., Kruse, G. W. & Loth, F. 2002 Spectral Element Method for Transitional Flows in Complex Geometries. *J. Sci. Comp.* **17**, 87–106.

Fransson, J. H. M., Matsubara, M. & Alfredsson, P. H. 2005 Transition induced by free-stream turbulence. *J. Fluid Mech.* **527**, 1–25.

Fuciarelli, D., Reed, H. & Lyttle, I. 2000 Direct Numerical Simulation of Leading-Edge Receptivity to Sound. *AIAA Journal* **38 (7)**, 1159–1165.

Goldstein, M. E. & Wundrow, D. W. 1998 On the Environmental Realizability of Algebraically Growing Disturbances and Their Relation to Klebanoff Modes. *Theoret. Comput. Fluid Dynamics* **10**, 171–186.

Jacobs, R. G. & Durbin, P. A. 2001 Simulations of bypass transition. *J. Fluid Mech.* **428**, 185–212.

Kendall, J.M. 1998 Experiments on boundary-layer receptivity to freestream turbulence. *AIAA Paper 98-0530* .

Kendall, J. M. 1985 Experimental study of disturbances produced in a pretransitional laminar boundary layer by weak free-stream turbulence. *AIAA Paper* **85** (85-1695), 1–10.

Leib, S. J., Wundrow, D. W. & Goldstein, M. E. 1999 Effect of free-stream turbulence and other vortical disturbances on a laminar boundary layer. *J. Fluid Mech.* **380**, 169–203.

Levin, O. & Henningson, D. S. 2003 Exponential vs Algebraic Growth and Transition Prediction in Boundary Layer Flow. *Flow, Turbulence and Combustion* **70**, 183–210.

Lin, N., Reed, H. & Saric, W. 1992 Effect of leading edge geometry on boundary-layer receptivity to freestream sound. In *Instability, Transition and Turbulence* (ed. M. Hussaini, A. Kumar & C. Streett). Springer.

Maday, Y., Patera, A. T. & Ronquist, E. M. 1990 An operator-integration-factor splitting method for time-dependent problems: Application to incompressible fluid flow. *J. Sci. Comput.* **5(4)**, 310–337.

Matsubara, M. & Alfredsson, P. H. 2001 Disturbance growth in boundary layers subjected to free-stream turbulence. *J. Fluid Mech.* **430**, 149–168.

Nagarajan, S., Lele, S. K. & Ferziger, J. H. 2007 Leading-edge effects in bypass transition. *J. Fluid Mech.* **572**, 471–504.

Patera, A. T. 1984 A Spectral Element Method for Fluid Dynamics: Laminar Flow in a Channel Expansion. *J. Comp. Phys.* **54**, 468–488.

Tufo, H. M. & Fischer, P. F. 1999 Terascale spectral element algorithms and implementations. In *Supercomputing, ACM/IEEE 1999 Conference*. Portland, USA.

Wanderley, J. B. V. & Corke, T. C. 2001 Boundary layer receptivity to free-stream sound on elliptic leading edges of flat plates. *J. Fluid Mech.* **429**, 1–21.

Xiong, Z. & Lele, S. K. 2007 Stagnation-point flow under free-stream turbulence. *J. Fluid Mech.* **590**, 1–33.

Zaki, T. A. & Durbin, P. A. 2005 Mode interaction and the bypass route to transition. *J. Fluid Mech.* **531**, 85–111.